Università degli Studi di Palermo

AREA QUALITÀ, PROGRAMMAZIONE E SUPPORTO STRATEGICO
SETTORE STRATEGIA PER LA RICERCA
U. O. DOTTORATI

Dottorato di Ricerca in Scienze della Terra e del Mare
Dipartimento di Scienze della Terra e del Mare (DiSTeM)
Settore Scientifico Disciplinare GEO/04

Soil erosion in Sicily: testing hydro-morphological approaches.

LA DOTTORESSA

Grazia Azzara

IL COORDINATORE

Prof. Alessandro Aiuppa

IL TUTOR

Prof. Edoardo Rotigliano

CICLO XXXVI
ANNO CONSEGUIMENTO TITOLO 2024

TABLE OF CONTENTS

1.0 INTRODUCTION

Denudation processes on Earth are intricate and natural modeling phenomena of its surface under the action of a set of agents, among which water runoff surface plays a central role in humid climatic areas. Each modeling process is marked by erosion s.s., transport, and deposit stages, which in the case of runoff water-related phenomena, have to be analyzed in a very complex system. In fact, running water flows with different modes from hillslopes (overland flow) to streams (drainage network) to rivers (channel). At the same time, the lithosphere exposes to the mechanic work of running water very different types of geo-materials, ranging from very (too) resistant cemented rocks to very weak soils and debris. In the case of rocks s.s. differences in terms of erodibility are linked to the lithogenetic processes (composition, texture, structure) and to subsequent weathering phenomena which can modify the original status in the outcropping horizon volumes. A large part of the Earth is actually "covered" by the products of weathering processes or the deposits of the modeling processes (debris s.s., in geomorphology). The moderately stable weathered layer is the base horizon where vegetation grows and deeply modifies and fixes the eluvium (soil s.s., in geomorphology). Debris deposits are the result of the erosive action of the modelling agent and can have very different characteristics according to the specific genetic process.

According to the very general elements given above, approaching the study of erosion poses the scientist in front of a very intricate challenge. However, a simplified approach can furnish tools for understanding and modeling the processes to an extent suitable enough to face the current requirements. In fact, if the natural rationale of erosion processes is out of doubt, the effects related to the crossing between these processes and human activity are of interest as some risk aspects are related. Soil loss is obviously a direct source of damage for agriculture and farming. Deteriorating soil and debris can result in destructive phenomena such as debris floods and debris flow, reducing the available channel section at bridges, or filling artificial reservoirs, reducing their storage capacity.

This thesis tries to investigate water erosion issues in Sicily, with a specific focus on three main adopted approaches.

The first approach is based on the analysis of the erosion processes from an experimental perspective, searching relations between the measured flow of water and sediment through a stream or fluvial section and the subtending hydro-morphodynamic, which merge in two time changing measured parameters all the effects of the interplay between rainfall/temperature forcing and slope, stream, and channel response.

In particular, the available historical data of the hydrometric gauge stations' regional network are analyzed by modeling Sediment Rating Curves (SRCs), which predict the Suspended Soil Concentration (SSC) from the water discharge (Q) and analyzing the mean hysteresis annual loops.

A different approach was adopted in the second experimental case, where SWAT (Soil and Water Assessment Tool), a physically-based continuous model for catchment scale simulations developed by

the USDA-ARS, was applied to the San Leonardo River basin. SWAT's objective is to determine how land use and management can affect water, sediment, and agricultural chemical yields in ungauged watersheds. In SWAT, erosion and sediment yield are estimated from the Modified Universal Soil Equation (MUSLE). While the USLE uses rainfall as an indicator of erosive energy, MUSLE uses the amount of runoff, which should improve the sediment yield prediction because runoff is a function of antecedent moisture conditions as well as rainfall energy. Therefore, differently from USLE, delivery ratios are not needed with MUSLE because the runoff factor represents energy in detaching and transporting sediment.

In a third application, water erosion assessment is carried out in the framework of a coastal erosion study to estimate the contribution of soil delivery at the coastal physiographic units in the advancement/retreatment stages. In particular, the spatially distributed model WaTEM/SEDEM is used to evaluate the sediment load carried to the coastal areas. The WaTEM/SEDEM model consists of three main components: soil erosion assessment, sediment transport capacity calculation, and sediment routing. Soil erosion is predicted with a modified version of RUSLE for 2-dimensional landscapes. Once the mean annual erosion rate is known at each grid cell, a routing algorithm is used to transfer the displaced soil amount (gross erosion) from the source to the river network according to the transport capacity (TC in Mg yr^{-1}).

2.0 SOIL EROSION AND SEDIMENT PRODUCTION

The continuing geomorphological modelling occurring on the Earth's surface implies the production of sediment and subsequent distribution of sediments. Soil particles are removed from one location and deposited at another.

Soil erosion can be defined as a three-phase process that consists of (i) the detachment of soil particles from the soil mass; (ii) their transport caused by one or more natural or anthropogenic erosive forces (rain, runoff, wind, gravity, tillage, land levelling, and crop harvesting); and, when sufficient energy is no longer available to transport the particles, (iii) their deposition (Boardman and Poesen, 2006).

On-site and off-site impacts of erosion on the environment have become a global issue because of their environmental and economic consequences. On-site effects are connected to the redistribution of soil within a field, the loss of soil from a field, the breakdown of soil structure and the decline in organic matter and nutrients, resulting in a reduction of cultivable soil depth and a decline in soil fertility and water-holding capacity (Morgan, 2006). Off-site problems include sedimentation downstream that decreases river capacity, increases the risk of muddy floods, and leads to sedimentation within artificial reservoirs that decreases their storage capacity. To decrease the rate of soil erosion to that of natural conditions, it is crucial to have a thorough understanding of the processes of erosion.

The focus of this chapter is on exploring different erosion processes.

2.1 PROCESSES AND MECHANISMS OF EROSION

2.1.1 EROSION AND SEDIMENT PRODUCTION ON HILLSLOPE

Most concerns about erosion are related to water-induced soil erosion which represents one of the most important and widespread causes of soil degradation. Soil erosion by water (Water Erosion) comprises splash, sheet or interill, rill, gully and pipe erosion.

Water erosion processes are closely related to the pathways water takes in its movement through vegetation and over the ground surface.

During a rainstorm, the rainfall component that directly falls on the ground and the component that drips from the leaves, known respectively as direct throughfall and leaf drainage, produce *rain splash erosion*, the most important detaching agent.

The action of raindrops on soil particles depends on the transfer of the momentum of the single raindrop falling on the soil surface, which has two effects. First, it provides a consolidating force compacting the soil and creating a surface crust a few millimetres thick that can produce a reduction of infiltration capacity. Second, the disruptive force of the raindrop impact produces a failure of the soil by the combined mechanism of compression and shear, launching the soil particles into the air over a distance of several centimeters. Drop impact is more effective if a thin water layer covers the soil surface because impacting raindrops induce turbulence on the water layer.

In general, the response of soil to a given rainfall depends upon its moisture content and, therefore, its structural state and the intensity of rain. Coarse soils are resistant to detachment because of the weight of the large particles. Finer soils are resistant because the raindrop energy must overcome the adhesive or chemical bonding forces that link the minerals in the clay particles. Overall, silt loams, fine sands, and sandy loams are the most detachable.

When the rainfall component reaches the ground, it may be stored in small depressions or hollows on the surface, or it may infiltrate the soil, filling the spaces between soil particles, contributing to soil moisture storage, and lateral movement downslope within the soil as interflow or, by percolating deeper, to the groundwater.

The forces driving infiltration are gravity and capillarity, whereby water is attracted to and held as a thin molecular film around the soil particles. Capillary force is a combination of two effects: surface tension and adsorption and the strength of those effects is referred to as soil suction, which depends on the amount of water present and on the pore size distribution. During the infiltration process, the rate at which water passes into the soil is not constant. Generally, water initially infiltrates at a faster rate and slows down with time to a steady level that theoretically corresponds to the saturated hydraulic conductivity of the soil. In practice, the infiltration capacity is often lower than the saturated hydraulic conductivity because of the air entrapped in the soil pores as the wetting front passes downwards through the soil. Infiltration rates depend upon the inter-particle spacing or micropores. Generally, coarse-textured soils such as sands and sandy loams, have higher infiltration rates than clay soils because of the larger spaces between the pores (Figure 2.1.1). In addition, also larger cracks or macropores exert an important influence over infiltration because they can transmit considerable quantities of water.

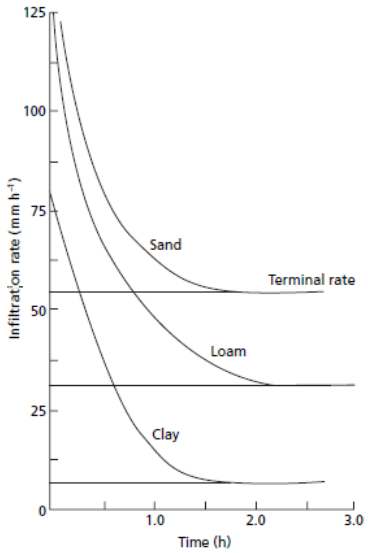

Figure 2.1.1 - Typical infiltration rates for various soils (Morgan, 2006)

When the soil cannot take in more water, the excess contributes to runoff. Different runoff processes can be observed at the hillslope scale. Overland flow is the water which runs across the surface of the land before reaching the stream. In the subsurface, throughflow (or lateral flow) occurs in the shallow subsurface predominantly in the unsaturated zone. Groundwater flow is in the deeper saturated zone (Figure 2.1.2). All of these are runoff mechanisms contribute to streamflow and the relative importance of each is dependent on the catchment under study and the rainfall characteristics during a storm.

The mechanisms for generating runoff are different. According to Horton, overland flow occurs when the rainfall intensity exceeds the infiltration capacity of the soil, and the infiltration rate equals the infiltration capacity, this type of overland flow is referred to as *Hortonian overland flow*. Hortonian overland flow is common on bare rock surfaces, and in deserts, where soil tends to be thin, bedrock outcrop common, vegetation limited, and rainfall rates high. Another important control for runoff production on many soils is a limiting moisture content. When the actual moisture content is below this value, pore water pressure in the soil is less than atmospheric pressure and water is held in capillary form under tensile stress or suction. When the limiting moisture is reached and all pores are full of water, pore water pressure equates to atmospheric pressure, suction reduces to zero and surface ponding occurs. This type of overland flow is referred to as *saturated overland flow*.

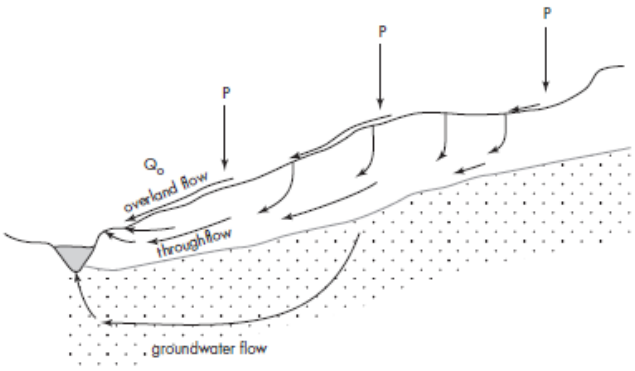

Figure 2.1.2 - Hillslope runoff processes (Davie, 2010)

Whatever the generating mechanism, the overland flow also plays a role in the detachment of soil particles. The important factor that controls the erosive power of the flow is the flow velocity. Because of the inherent resistance of the soil, before erosion starts the forces exerted by the flow must exceed the forces keeping the particles at rest, and this happens when velocity achieves a threshold value. For particles larger than 0.2 mm a larger force is required to move larger particles, so the critical shear velocity increases with particle size. For particles smaller than 0.2 mm, the critical shear velocity increases with decreasing particle size. The finer particles are harder to erode because of the cohesiveness of the clay minerals. In general, the detach capability of the overland flow, related to flow shear stress, is negligible compared to the one of rainfall impact.

Once the sediment has been entrained within the flow, it will be transported at such time as deposition occurs.

The transport of soil particles by running water occurs commonly by *interill and rill erosion* (Fig. 2.1.3). Interill erosion refers to the combined action of raindrop impact and overland flow on the land between the rills. Rill erosion refers to water running as a concentrated flow. About the mechanism of the breakup of overland flow into rills, Moss et al., (1982) found that in addition to the main flow path downslope, secondary flow paths develop with a lateral component. Where these converged, the increase in discharge intensified particle movement and small channels or trenches were cut by scouring. Merritt, (1984) found that the shift from overland flow to rill flow passes through four phases: unconcentrated overland flow, overland flow with concentrated flow paths, microchannels without head cuts and microchannel with headcuts (channelled flow). Once rills have been formed, they can migrate upslope and downslope. The first occurs by the retreat of the headcut at the top of the channel. Morgan (2006) explains that the rate of retreat is influenced by the cohesiveness of the soil, the height and angle of the headwall, the discharge, and the flow velocity.

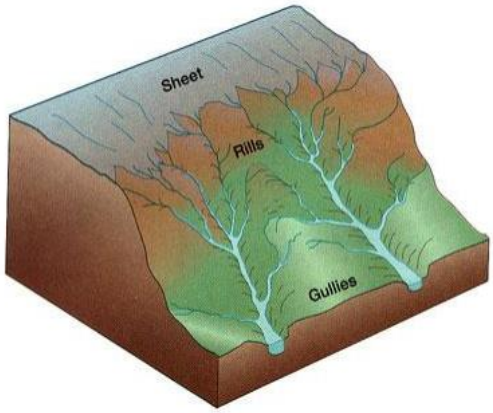

Figure 2.1.3 - Types of erosion processes on hillslope.

Downslope extension of the rill is controlled by the shear stress exerted by the flow and the strength of the soil. Different from rills that generally appear at different locations on the slope from year to year, ephemeral gullies occur in the same spot every year. The term *ephemeral gully* was introduced by Foster, (1986) to describe channels intermediate in size between rills and classic gullies, the 'ephemeral' nature of this erosion feature results from the fact that ephemeral gullies are ploughed in and tilled across annually. In contrast to ephemeral gullies that are short-lived, *classical gullies* are permanent steep-sided water channels characterized by a head cut and various steps or knick-points along their course. A widely recognized definition used to separate gullies from rills is that gullies have a cross-sectional area greater than 1 m^2. The formation of a gully is complex (Fig. 2.1.4), it starts in small depressions of the hillside created because of localised weakening of the vegetation cover by grazing or fire. Water becomes concentrated in these depressions and enlarges them until several depressions coalesce to form an incipient channel. As the channel progresses, the erosion processes are focused either at the top of the depression, where there are near vertical scarps, or at the bottom of the scarp due

to the water's scouring action. Deepening of the channel and weakening of the headwall result in the collapse and retreat of the scarp upslope.

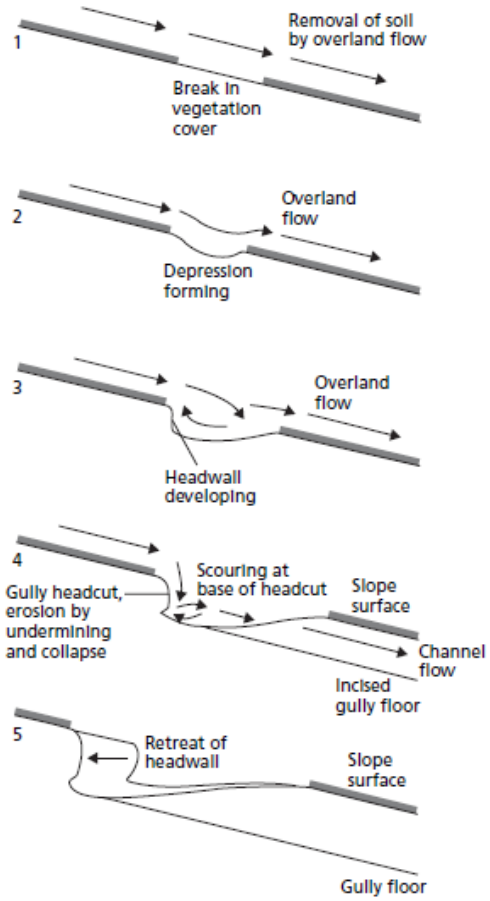

Figure 2.1.4 - Stages in the surface development of gullies on a hillside (Morgan, 2006)

Generally, the main cause of gully formation is an increase in runoff. It may occur if rainfall increases or if deforestation, burning of vegetation, and overgrazing reduce the vegetation cover.

The severity of erosion associated with rills and gullies depends upon the quantity of material available for transport and the capacity of the water to transport it. Sediment available for transport in rills and gullies is from the interill erosion on adjacent overland flow areas. The sediment transport capacity refers to the amount and size of sediment that the water has the ability or energy to transport. Where the water has the capacity to transport more material than is supplied by detachment, the erosion is described as detachment-limited. Where more material is supplied than can be transported, the erosion is transport-limited.

2.1.2 Erosion and sediment production on the channel

Channel erosion consists of the removal of soil and rock by a concentrated flow of water. It includes stream bed and stream bank erosion. Stream bed erosion in alluvial channel beds takes place when there is a net removal of sands and gravels, in bedrock channels, erosion is caused by the channel's bed load

abrading the bed. Stream bank erosion occurs when the channel banks are carried away, usually by being undercut, which leads to slumping and bank collapse.

The ability of water to erode and transport rock and sediment is a function of a stream's kinematic energy (the energy of motion). If Chézy's equation is substituted for velocity in the equation of kinetic energy, the equation will be:

$$E_k = \frac{(mCR_s)}{2}$$

Where:

m is the mass of water.

C is the Chézy coefficient representing gravitational and frictional forces.

R_s , R is the hydraulic radius and s is the stream gradient.

This equation shows that the deeper and faster a stream, the greater its kinetic and larger its potential to erode. Two criteria are used for defining incipient motion, the shear stress approach and the velocity approach. The shear stress or tractive force on the channel bed can be defined with the following equation:

$$\tau = \gamma ds$$

Where:

γ is the specific weight of water (g/cm^3)

d is water depth (cm)

s is the stream gradient expressed as a tangent of the slope angle.

This equation relates the resistance of the channel bed and banks to the downstream gravitational tractive force of the water: when the former is exceeded, sediment transport is initiated. Critical shear stress, τ_c, refers to the shear stress necessary to mobilise a given grain size. When the bed shear stress exceeds the critical shear stress, a part of the bed material starts to move. The forces that resist the entraining action of the flowing water differ according to the grain size and grain size distribution of the sediment. For coarse sediments, e.g., sands and gravels, the forces resisting motion are caused mainly by the weight of the particles; the medium sand is eroded at the lowest velocities. Finer sediments that contain a fraction of silt and clay tend to resist cohesion. Also, these deposits undergo consolidation with time; since the resistance to erosion increases with consolidation, the critical shear stress has to exceed the shear stress under which the sediment was deposited plus any strengthening to consolidations before starts.

The relationships between the stream's flow velocity and its ability to erode and transport grains of a particular size are expressed in the Hjulström diagram (Figure 2.1.5). The upper curve shows the critical velocities at which grains of a given size start to erode, soil particles of 0.01 mm required a higher velocity for erosion. The lower curve shows the velocity at which particles in motion cannot be

transported further and fall to the channel bed. It depends on the grain's size, density, and shape but also on the viscosity and density of the water. As the flow velocity reduces, the coarser particles are deposited first, with progressively finer grains dropping out of the flow as the flow velocity continues to decline. The result is differential settling and sediment sorting.

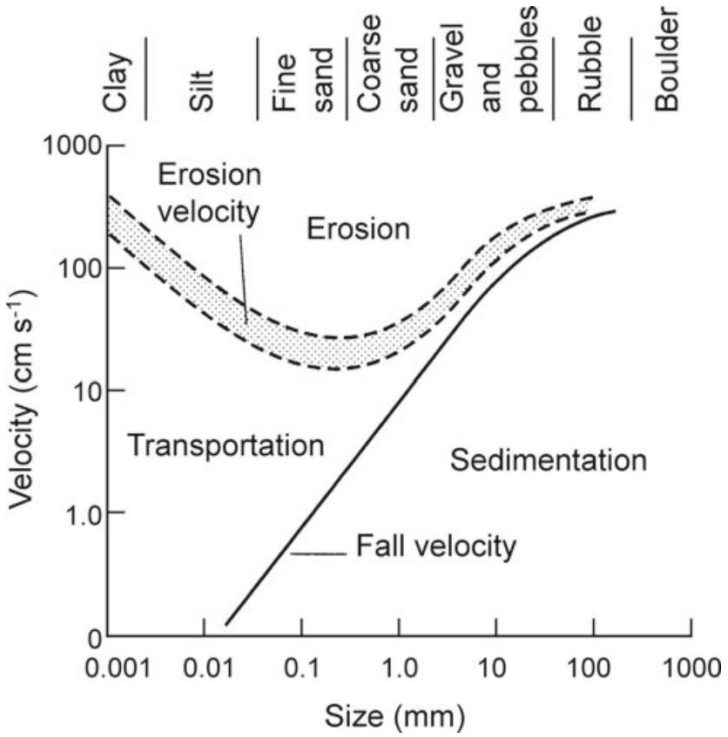

Figure 2.1.5 - Critical water velocities for erosion, transport, and deposition of sediment as a function of particle size (Hjulström 1935)

Sediment load is the amount of sediment passing a point over an interval. It is estimated by multiplying sediment concentration by water discharge. By mode of transport, sediment load is separated into two classes:

- *Bed load* consists of granular particles transported by sliding, rolling, or hopping near the bed.
- *Suspended sediment load* is that part of the sediment load transported within the main body flow, and it may be subdivided into wash load and suspended bed material load.
    - *Wash load* consists of fine sediments mainly derived from either channel banks or hillslope area contributing runoff to the stream. Wash load grains tend to be very small (clay and silts) and have a very small settling velocity (Figure 2.4). Once introduced into the channel, wash-load grains are kept in suspension by the flow turbulence and essentially pass straight through the stream with negligible deposition or interaction with the bed.
    - *The suspended bed material load* is the suspended load derived primarily from the channel bed.

The *sediment transport capacity* is the total load of sediment that the river has the ability or energy to carry. The key components that control the sediment transport capacity are the velocity and depth of the water moving through the channel. The channel slope, dimensions, discharge, and roughness control velocity and depth. Changes in any of these parameters will result in a change in the sediment transport capacity of the river. Generally, the higher the velocity and discharge, the larger the quantity of sediment transported unless the sediment supply is depleted. Some general assumptions can be made by comparing the sediment transport capacity with the sediment load. Erosion would be expected if the capacity exceeds the sediment load due to the excess energy. Deposition is expected when the capacity is less than the sediment load. If the capacity equals the sediment load, no net change in erosion and deposition would be expected. Another way to view this concept is to use Lane's relationship:

$$Q_s D_{50} \sim Q_w S$$

Where:

Q_s is the sediment discharge.

D_{50} is the median particle size.

$Q_w$is the water discharge.

S is the slope.

Rearranging the relation, it is apparent that sediment transport is directly related to stream power ($Q_w S$) and inversely related to grain size. The stream power is the capacity of a stream to do work. In other words, stream power is the rate at which a stream works to transport sediment, overcome frictional resistance, and generate heat. Thus, steeper slopes and higher discharges both increase stream power. The Lane relationship can be visualized using the Lane's Diagram (Figure 2.1.6):

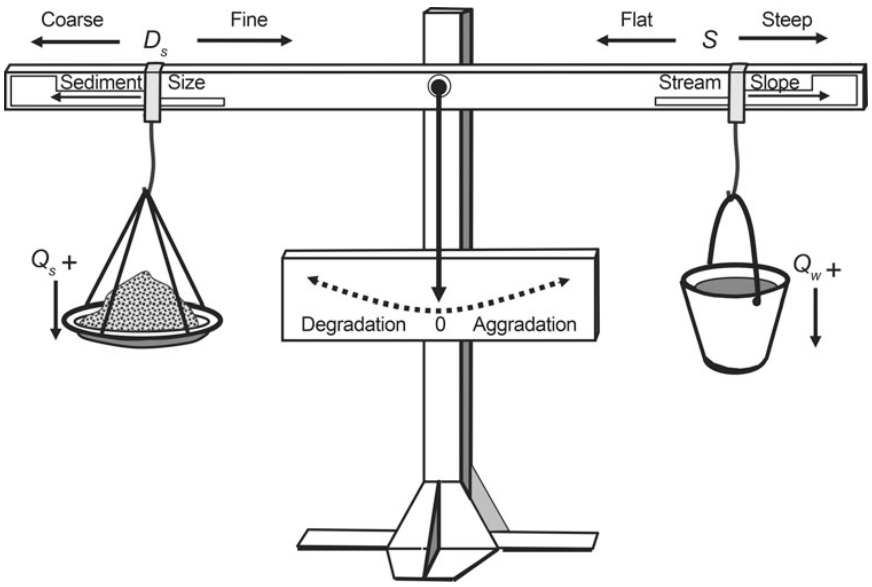

Figure 2.1.6 - Lane's Diagram (Allan et al., 2021)

Lane's balance demonstrates how the channel may respond to a change in various parameters, and it implies that the channel will remain in equilibrium as long as no major change occurs in any of the variables. Aggradation is the result of a shift in the balance towards aggradation when there is an increase in the volume or dimension of the sediment load compared to the available stream power. When stream power exceeds what is needed to transport the sediment load through the reach, this excess energy is used to erode, and in this case, degradation predominates.

2.2 SEDIMENT DELIVERY RATIO

The interplay of stream capacity to transport sediment with the input of sediment and their size results in different balances between erosion and deposition along the river profile. As one proceeds downslope, the drainage basin changes from a sediment production to a sediment-accumulating system: the upland zone, closely associated with the hillslope, from which sediments are exported. The middle or transitional zone is where erosion and deposition take place and where sediments are transported onward. The zone near the distal end of the drainage system, where gradients are low and sediment deposition is dominant, resulting in large floodplains, alluvial fans, and deltas (Figure 2.2.1). These variations lead to downstream changes in channel and floodplain morphology.

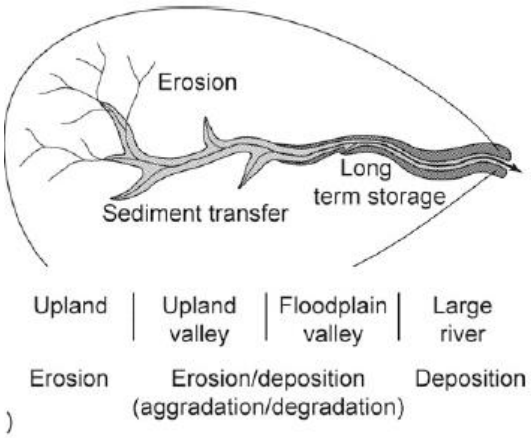

Figure 2.2.1 - Three principal longitudinal Zones in stream channels: an upland zone where the drainage forms and from which sediments are exported; a middle, transitional zone where erosion and deposition of sediments may be approximately in balance; and a lower floodplain where sediments may accumulate (Church, 2002).

Not all of the eroded material is effectively routed to the river systems and delivered to the sea. Sediment yield is the amount of eroded soil that is delivered to a point in the watershed that is remote from the origin of the detachment soil particles (Figure 2.2.2). In a watershed, sediment yield includes erosion from slopes, channels, and mass wasting, minus the sediment that is deposited after it is eroded but before it reaches the point of interest. Deposition and temporary or permanent storage may occur on the hillslope, particularly where gradients decline downslope, foot slopes, flood plain, or channel itself.

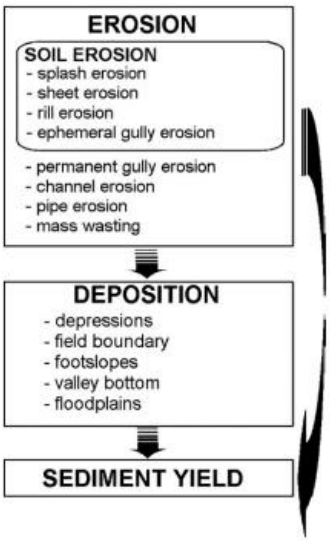

Figure 2.2.2 – The distinction between erosion, soil erosion, deposition and sediment yield (De Vente et al., 2008)

The proportion of eroded sediment that exits the drainage basin as part of the river's load is called the S*ediment Delivery Ratio (SDR):*

$$SDR = \frac{SSY}{gross\_erosion}$$

Where: $gross\_erosion$ is all erosion in the watershed (i.e., sheet and rill, gully, streambank, and landslides), the quantity of gross erosion that is delivered to a specific location is the Suspended Sediment Yield (SSY). SDR represents the efficiency of the watershed in moving soil particles from areas of erosion to the point where sediment yield is measured. Sediment delivery ratios vary between watersheds due to differing physical attributes. Many studies reported a decreasing area-specific sediment yield with increased drainage basin area. Of course, gross erosion is high in large drainage basins, but there is more spare space, or volume, available for storing sediment. This means that a greater proportion of the eroded sediment ends up in storage.

Rates of gross erosion on hillslope are determined by the erosivity of rainfall and runoff and the erodibility of the surface, and therefore by factors, including soil type, land use, topography, and human activity. A poor cover increases the SDR because runoff is not slowed by growing vegetation, and the deposition of eroded particles is low. Short, steep slopes will deliver more sediment to a channel than a watershed with long, complex slopes. Also, channel density controls SDR, in a watershed with high channel density the distance from eroding areas to a channel is short, and soil particles have less chance to deposit. Finally, watersheds where channel and gully erosion is higher than sheet and rill erosion, have a higher SDR due to a high transport capacity of gullies and streams.

2.3 MEASUREMENT OF SOIL EROSION

2.3.1 EROSION PLOT

Erosion plots are bounded plots used at experimental stations to study the factors influencing erosion. The plots are pieces of land of known size, slope steepness, slope length and soil type. The standard plot is 22 m long and 1.8 m wide with an edge made of sheet metal. At the downslope, a collection trough is positioned, and equipped with a lid to prevent direct rainfall entry. This trough directs sediment and runoff into collection tanks. Within each tank, a flocculating agent is introduced into the water-sediment mixture. At the bottom of the tank, the sediment is settled, while the clear water is extracted and measured. The amount of soil in the tank is calculated, and samples of known volume are collected for drying and weighing later. Multiplying the mean sample weight by the total volume gives the overall weight of soil within the tank. By using this method, the total soil loss from the designated plot can be accurately assessed when all soil has been successfully collected in the tank.

2.3.2 MEASUREMENT SEDIMENT DISCHARGE

Based on the distribution of the sediment in the flow, the sediment measurement techniques are divided into two categories:

Measurement of suspended sediment discharge

There are several types of suspended sediment samplers; their purpose is to obtain a representative sample of the water-sediment mixture moving in the stream in the vicinity of the sampler intake. The instantaneous samplers are horizontal cylinders, lowered into streams, and aligned to flow, equipped with end valves that can be closed suddenly to trap a sample at any desired time and depth (Figure 2.3.1 - D and E).

The time-integrating suspended sediment samplers consist of samplers that collect a sample during a finite time interval. These are of two types: depth-integrating and point-integrating. The depth-integrating sampler (Figure 2.3.1 - A and B) is designed to accumulate a water-sediment sample while it is lowered to the stream bed and raised to the surface at a uniform rate. Good samplers are designed to maintain isokinetic conditions. Accordingly, the sampling intake velocity equals the natural flow velocity at every point. The sample is then dried to measure the flux-averaged concentration, C_f. The point-integrating sampler (Figure 2.3.1 - C) is designed to accumulate a water sediment sample that is representative of the mean concentration at any selected point in a stream during a short interval of time (Vanoni, 1975). The dried sample measures the time-averaged sediment concentration, C_t.

The integrated sampler comprises a streamlined metallic body with tail fins for proper alignment within the water flow. The body of the sampler houses the sample container, and a variable-diameter intake nozzle extends into the current from the sampler head. A downstream-oriented exhaust tube facilitates the release of air from the container. Valve mechanisms enclosed in the head are under the electrical control of the observer, enabling the initiation and cessation of the sampling process.

The single-stage samplers (Figure 2.3.1 – F) were developed for obtaining sediment data on streams were remoteness of site location and/or rapid changes in stage make it impractical to use a conventional depth integrating sampler.

Finally, it is possible to record sediment concentration on a continuous basis by monitoring turbidity. Sediment concentration is not measured directly, instead, optical sensors can be used to record how much light passes through the flow. These measurements can be related to the concentration of sediment since more light is absorbed at higher concentrations.

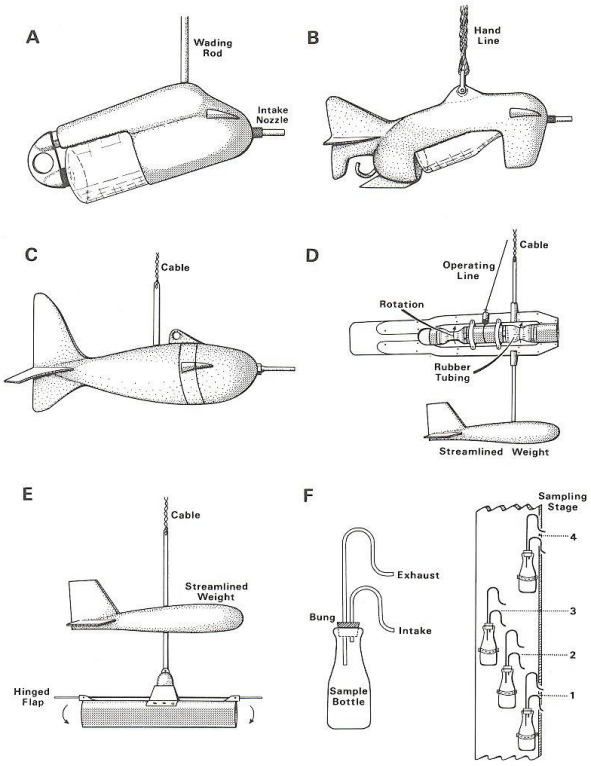

Figure 2.3.1 – Types of suspended sediment samplers

It is worth noting that in a natural stream, the sediment concentration at a given cross-section varies in both the vertical and the transversal directions and changes with time. Therefore, the concentration of sediment in suspension may increase or decrease both in space and time, although the flow remains steady in a straight, uniform reach. Concentration data are typically acquired using one of the following three approaches: (1) depth-integrated samples taken at stream verticals representing areas of equal water discharge in the cross section; (2) depth-integrated samples collected at equally spaced stream verticals in the cross section; and (3) point-integrated samples gathered at selected depths at stream verticals representing areas of equal water discharges. For both schemes (1) and (2), the concentration is the suspended-sediment discharge concentration $\bar{C}_f$ for the sampled portion of the stream section. The suspended-sediment discharge, Q_s, is given by:

$$Q_s = C_f\, Q = \int_A C\, v_x d\, A$$

in which:

C_f is the suspended-sediment discharge concentration;

Q is the stream discharge;

C is the point concentration;

v_x is the velocity of sediment particles;

d is the depth

A is the cross-sectional area.

The measured suspended-sediment discharge, Q'_s, is, by definition, the product of the measured suspended-sediment discharge concentration, C'_f and the total water discharge, Q, in the cross-section. In scheme (1), the transit rate of the sampler must be consistently uniform, although it may vary among verticals, the concentration is the average obtained for depth-integrated samples taken at stream verticals representative of areas of equal discharge. For scheme (2), the transit velocity of the sampler must be uniform and consistent across all verticals, and the concentration for the stream cross-section is a value derived from a composite of partial samples collected at all verticals. Since the sampling procedure typically employs wading equipment, the water-sediment mixture for one or more verticals will be collected in containers while traversing the cross-section. The precision of sediment discharge records relies on accurately determining both the concentration and the corresponding water discharge. The field installation needed to gather data for determining suspended-sediment discharge primarily depends on the stream's size and the desired accuracy of the record. In the case of small streams, samples are gathered by wading or from footbridges using hand-operated samplers. In medium-sized rivers, samples are collected from cable or bridge measuring installations, utilising both depth and point integrating samplers (Vanoni, 1975).

Measurement of bed material discharge

Measurement of bed load discharge is difficult because it is highly variable in both space and time. Bed load generally varies greatly both longitudinally along the channel and transversely across a cross-section.

The samplers for bed load have been classified into slot trap, basket types, pan types and pressure - difference types. The slot trap (Figure 2.3.2 – A) is installed in the bed of the channel and consists of removable small containers that catch and retain all bed load sediment that is transported to the sampler. The basket and pan types (illustrated in Figure 2.3.2 -- D and B, respectively) introduce elevated resistance to the flow, leading to a decrease in stream velocity at the sampler. This diminished velocity in the stream lowers the rate of bed load movement at the sampler. Consequently, certain particles accumulate at the sampler entrance, while others are redirected away.

The pressure-difference type (Figure 2.3.2 – C) is designed to eliminate the reduction in velocity, and thus any change in the rate of bed load movement at the entrance to the sampler. The velocity in the sampler is made equal to that of the flow by creating a decrease in pressure at the exit of the sampler nozzle by having a gradual increase in area.

Perhaps the most accurate of these types of samplers are the slot traps however, the difficulty and high cost of their installation preclude their use in many studies. The only practical way to collect samplers is often the use of portable samplers. To effectively use portable samplers, the number and location of the samples collected must be carefully designed to ensure sufficient information about the temporal and spatial variability is collected.

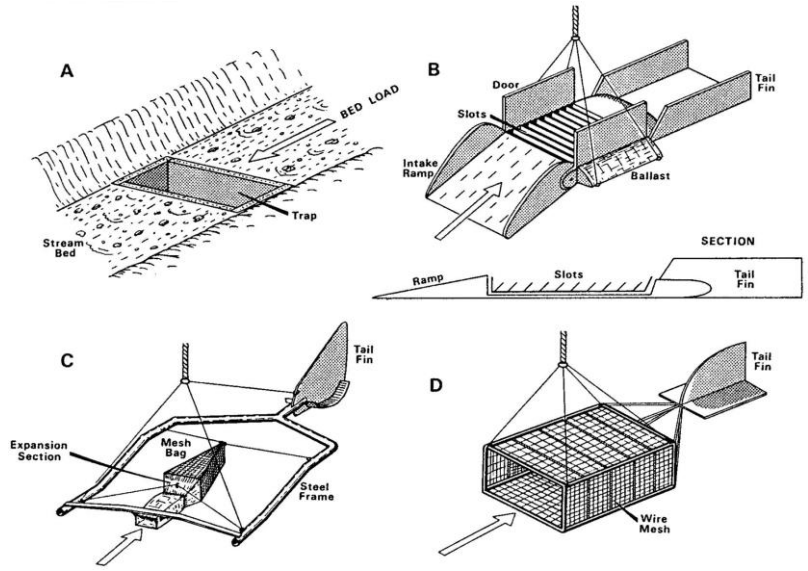

Figure 2.3.2 – Types of bed load samplers.

2.3.3 RESERVOIR SURVEYS

As a stream flows into a reservoir, the depth of the flow increases while the velocity decreases. This leads to a reduction in the stream's sediment transport capacity, resulting in sediment settling. The deposition pattern in a reservoir typically initiates with coarser sediment settling in the headwaters area, forming a delta. Density currents may transport finer sediment particles downstream towards the dam.

Various survey techniques are employed, including sonic equipment primarily measuring reservoir elevation, and terrestrial or aerial photogrammetry surveying to measure the water surface area at a specific stage.

Sonic sounders, operating from boats crossing the reservoir, continuously detect the reservoir bottom. Depth measurement relies on the speed of sound through the water. Under known reservoir water temperature and salinity conditions, the speed of sound through water governs the time interval between the projected and received signals, directly correlating with water depth. The sonic sounding instrument comprises three units: the recorder, housed in a protective metal case, includes mechanical recording components and electronic phasing, keying, and power circuitry; the transmitting-receiving transducers;

and a power source, which can be either a wet cell battery or a generator-converter combination based on the vessel's size.

Airborne or satellite-based requires minimal ground control. With stereoscopic equipment, contour maps can be easily generated. GPS and differential GPS are recommended, with a 1-2 meter position currently considered acceptable for reservoir mapping and estimating sediment volume (Julien, 2010)

Additionally, it is crucial to sample the deposited sediments to determine specific mass density and particle size distribution. Sediment samplers like gravity core and spud-rod samplers are used to obtain undisturbed volumetric samples of the deposited sediments.

Sedimentation rates in lakes and reservoirs can indicate how much erosion has occurred in a catchment upstream, provided the efficiency of the reservoir as a sediment trap is known. Utilizing a contour map created for the reservoir bottom, the reservoir volume can be calculated by summing up partial volumes (V) using the formula:

$$V = \frac{h(A + B)}{2}$$

Where V is the volume of sediment (m^3), h is the upper contour interval (m), A is the area of the upper contour (m^2), and B is the area of the lower contour interval (m^2). To this total, the volume below the lowest contour is added, calculated as the product of the area of the lowest contour and the mean depth to that contour from the bottom. The resulting reservoir volume is then compared with the initial volume. The amount of sedimentation that has accumulated in the reservoir can be determined by observing the reduction in volume. Assuming an average dry bulk density value, the volume is converted into a mass and divided by the area of the catchment upstream to yield an erosion value in tons per hectare (t ha^{-1}). This value is further adjusted by assuming that sediment in the reservoir represented about half that eroded from the catchment. Dividing the adjusted total by the years since the reservoir was built gives a mean annual erosion rate.

2.4 MODELLING SOIL EROSION AND SEDIMENT YIELD

Over the last decades, important progress has been made in understanding, describing, and modelling soil erosion rates (Mg km^{-2} yr^{-1}) and associated sediment yield (Mg km^{-2} yr^{-1}) at various spatial and temporal scales. Based on the complexity and the level of the dynamic physical processes applied, the modelling approaches are classified into empirical or regression, conceptual, and physically based models.

Empirical models are based on identifying statistically significant relationships between assumed important variables where a reasonable database exists. They are relatively simple in structure and application, requiring less computational effort.

Conceptual models are based on a simplified representation of the physical processes involved in soil erosion. They use conceptualizations of the watershed and its components to simulate erosion based on assumed relationships.

Physically based models are based on mathematical equations to describe the processes involved in the model, taking account of the law of conservation of mass and energy. The most challenging of all three types, it necessitates detailed input data and computational resources.

2.4.1 EMPIRICAL MODELS: REVISED UNIVERSAL SOIL LOSS EQUATION (RUSLE)

The erosion rate at a given site is determined by the particular way in which levels of numerous physical and management variables are combined at that site. The first attempt to develop a soil loss equation was that of Zingg, 1940 who published the first equation for calculating field soil loss relating erosion to slope length and slope steepness. Further studies led to the addition of a crop factor, to take account of the protection effectiveness of different crops (Smith, 1941), a conservation factor, and a soil erodibility factor (Browning et al., 1947). Finally, by adding a climatic factor based on the rainfall erosivity index (R), Wischmeier and Smith, (1978) developed the Universal Soil Loss Equation (USLE). An updated form of the USLE (RUSLE) was published later by Renard, (1997), to include improvements to the method of calculating the different USLE factors.

The Revised Universal Soil Loss Equation is an erosion model designed to compute longtime average soil loss (E) resulting from raindrop splash and runoff under a specific combination of crop systems and management practices. Factor affecting erosion can be expressed in an equation of the form:

$$E = R \times K \times LS \times C \times P$$

Where:

E is the annual average soil loss (t ha^{-1} yr^{-1})

R is the rainfall erosivity factor (MJ mm ha^{-1} yr^{-1})

K is the soil erodibility factor (t ha h ha^{-1} MJ^{-1} mm^{-1})

LS is the slope length and slope steepness factor (dimensionless)

C is the cover-management factor (dimensionless)

P is the support practices factor (dimensionless).

RUSLE predicts soil loss based on the factors influencing the erosion rate: energy, resistance, and protection. The energy is related to the potential ability of rainfall and runoff to cause erosion, and this ability is called erosivity. The resistance is related to the erodibility of the soil, which depends upon its mechanical and chemical properties. Factors relating to the plant cover, land use, and management techniques constitute the protection because intercepting rainfall and reducing the velocity of runoff and wind can protect soil from erosion.

- *Rainfall Erosivity Index (R)*

The erosivity of a rainstorm is related to the kinetic energy of the rain, and it is a function of the intensity and duration of the rainfall, and of the mass, diameter, and velocity of the raindrops. Laws and Parsons, (1943) showed that the drop size characteristics vary with the intensity of the rain, in general, median drop diameter by volume increases with rainfall intensity.
Based on this work, Wischmeier and Smith, (1958) obtained the equation:

$$E = 0.0119 + 0.0873\log_{10} i$$

Where:
i is the rainfall intensity (mm h^{-1}), $i \leq 76$ mm h^{-1}
E is the kinetic energy (MJ ha^{-1} mm^{-1})

To compute the kinetic energy of a storm, a trace of the rainfall from an automatic recording gauge is analysed and the storm is divided into small time increments of uniform intensity (Figure 2.4.1). For each elemental rain the rainfall intensity i is calculated having a rainfall depth and a duration t. Then, the specific and unitary kinetic energy of the rain at that intensity is estimated using the above-mentioned equation.

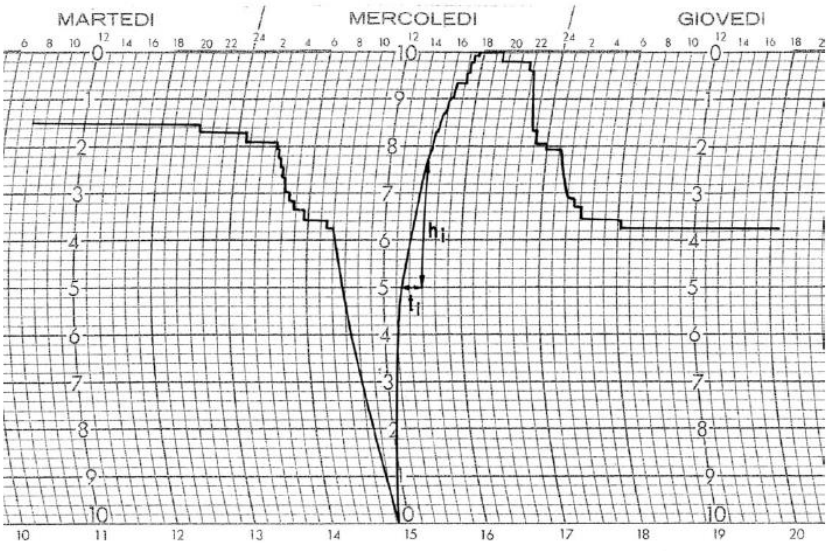

Figure 2.4.1 - Hyetograph divided into m parts, each with constant rainfall intensity.

Another equivalent formula for calculating the unit rainfall energy (MJ ha^{-1} mm^{-1}) for each time interval was suggested by Brown and Foster, (1987) and used in the Revised Universal Soil Loss Equation:

$$e_r = 0.29\,[1 - 0.72\exp(-0.05 i_r)]$$

Where:

i_r is the rainfall intensity during the time interval (mm h^{-1}).

According to Wischmeier and Smith, (1958), the soil loss by splash, overland flow and rill erosion is expressed as the product of the total kinetic energy E of a storm times its 30-min maximum rainfall intensity I_{30} of each erosive storm for the specific time period as follows:

$$EI_{30} = \sum_{r=1}^{0} (e_r v_r) I_{30}$$

Where:

e_r is the unit rainfall energy (MJ ha^{-1} mm^{-1})

v_r is the rainfall volume (mm) during a time period

I_{30} is the maximum rainfall intensity during a 30-min period of the rainfall event (mm h^{-1})

Finally, the average annual rainfall erosivity is expressed as:

$$R = \frac{1}{n} \sum_{j=1}^{n} \sum_{k=1}^{m_j} (EI_{30})_k$$

Where:

R is the average annual rainfall erosivity (MJ mm ha^{-1} h^{-1} yr^{-1})

n is the number of years covered by the data records

m_j is the number of erosive events of a given year j

EI_{30} is the rainfall erosivity index of a single event k.

The R-factor calculation requires the identification of erosive rainfall events (mj) for the station. Two rainfall events are considered distinguished when separated by a time interval of no rain equal to or greater than 6 hours. Other criteria to define an erosive event are: (i) the cumulative rainfall of an event is greater than 12.7 mm, or (ii) the event has at least one peak greater than 6.53 mm during a period of 15 min (or 12.7 mm during a period of 30 min) (Renard, 1997).

- *Erodibility factor (K)*

Erodibility defines the resistance of the soil to both detachment and transport. It varies with soil texture, aggregate stability, shear strength, infiltration capacity, and organic and chemical content. About the role of texture, considering that large particles are resistant to transport because of the greater force required to entrain them and that fine particles are resistant to detachment because of their cohesiveness, in very general terms, the silt size particles are eroded most easily, and soil became less erodible as

either the sand fraction or the clay fraction increased. The rate of increase in erodibility with additional increments of silt-size material became less as either organic matter or the clay-to-sand ratio increased. The rate of decrease in erodibility with increased clay content declines with higher organic-matter content or higher aggregation index.

The erodibility of soil is described by the soil erodibility factor K. The soil erodibility factor K is the rate of soil loss per rainfall erosion index unit as measured on a unit standard bare soil plot, 22 m long and with 9° slope and continuously in a clean-tilled fallow condition with tillage performed upslope and downslope. In practical terms, the K factor is the average long-term soil and soil-profile response to the erosive powers of rainstorm.

Soil erodibility factors are best obtained from direct measurements on natural runoff plots or in rainfall-simulation plots. However, the direct measurement of the K-factor on field plots is not financially sustainable. For this reason, the soil erodibility nomograph (Figure 2.4.2) is the most commonly used method for soil erodibility calculation (Wischmeier et al., 1971).

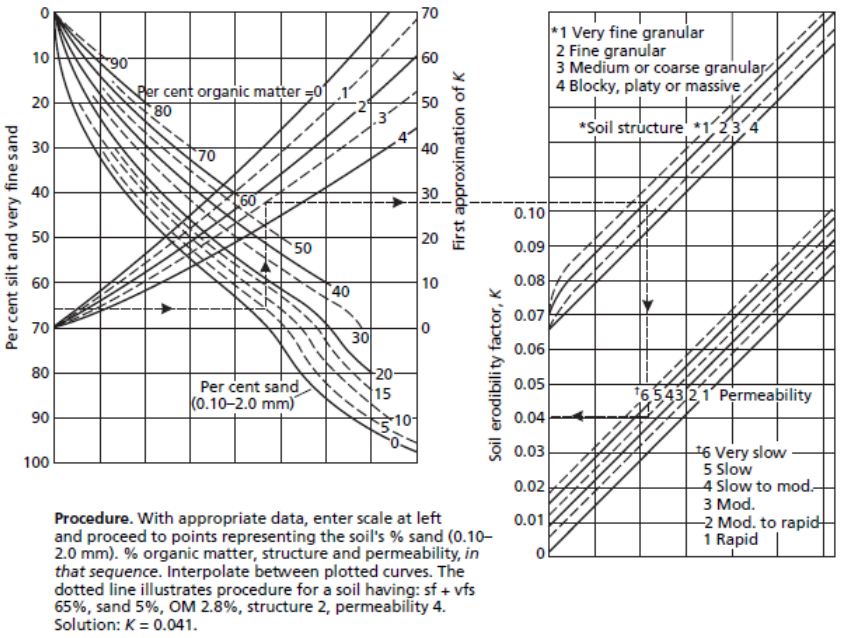

Figure 2.4.2 - Nomograph for calculating the K-factor of soil erodibility (Wischmeier et al., 1971)

An algebraic approximation of the nomograph, including five soil parameters, was proposed by (Renard, 1997) for those cases where the silt fraction does not exceed 70%:

$$K = \frac{\left[2.1\ 10^{-4}(12 - OM)\ M^{1.14} + 3.25\ (s - 2) + 2.5[p - 3]\right]}{100} * 0.1317$$

Where:

K is the K factor expressed as t ha h ha^{-1} MJ^{-1} mm^{-1}

M is the textural factor with M = (m_{silt} + m_{vfs}) * (100 - m_c)

m_c [%] is the clay fraction content (<0.002 mm)

m_{silt} [%] is the silt fraction content (0.002 – 0.05mm)

m_{vfs} [%] is the very fine sand fraction content (0.05 – 0.1 mm)

OM [%] is the organic matter content.

s is the soil structure class (Table 2.4.1)

p is the permeability class (Table 2.4.2)

Structure class (s)		
1	Very fine granular	1-2 mm
2	Fine granular	2-5 mm
3	Medium or coarse granular	5-10 mm
4	Blocky, platy or massive	>10mm

Table 2.4.1 – Soil Structure Classes

Permeability class (p)		Texture
1	Fast and very fast	Sand
2	Moderate fast	Loamy sand, sand loam
3	Moderate	Loam, silty loam
4	Moderate low	Sandy clay loam, clay loam
5	Slow	silty clay loam, sand clay
6	Very slow	Silty clay, clay

Table 2.4.2 – Permeability Classes

- *Slope length and slope steepness factor LS*

Topographic factors L and S adjust the soil-loss prediction for effects of difference in length and steepness of land slope. Erosion increases with increases in slope steepness and slope length as a result of respective increases in velocity and volume of surface runoff.

Slope length is defined as the horizontal distance from the origin of overland flow to the point where either the slope gradient decreases enough that deposition begins or runoff becomes concentrated in a defined channel (Wischmeier and Smith, 1978b). The soil loss per unit area generally increases as slope length increases. The greater accumulation of runoff on the longer slopes increases its detachment and transport capacity. L-factor was defined as the ratio of soil lost from a horizontal slope length to the corresponding loss from the slope length of a unit plot (22.13 m):

$$L = \left(\frac{\lambda}{22.13}\right)^{m}$$

Where:

λ is the slope length (m)

m is equivalent to 0.5 for slopes steeper than 5 %, 0.4 for slopes between 3%-4%, 0.3 for slopes between 1%-3% and 0.2 for slopes less than 1%. It is also related to the ratio β of the rill to interill erosion:

$$m = \frac{\beta}{(1 + \beta)}$$

With:

$$\beta = \frac{\left(\frac{\sin\theta}{0.0896}\right)}{[3.0(\sin\theta^{0.8}) + 0.56]}$$

Where:

θ is the slope angle.

The m ranges between 0 and 1, and it approaches 0 when the ratio of rill to interill is close to 0.

The slope steepness factor (S) reflects the influence of slope gradient on erosion. Soil loss increases when slopes steepen. The S-factor is the ratio of soil loss from the field slope gradient to that from the 9% slope under otherwise identical conditions. It is evaluated by the equation:

$$S = 65.41\ \sin^2\theta + 4.56\ \sin\theta + 0.065$$

Where:

θ is the slope angle.

Combining the above equations, the LS factor is the expected ratio of soil loss per unit area from a field slope with a 22.13 m length of uniform 9 % slope under otherwise identical conditions. This ratio for specified combinations of field slope length and uniform gradient may be obtained directly from the slope-effect chart (Figure 2.4.3), assuming slopes that have essentially uniform gradients:

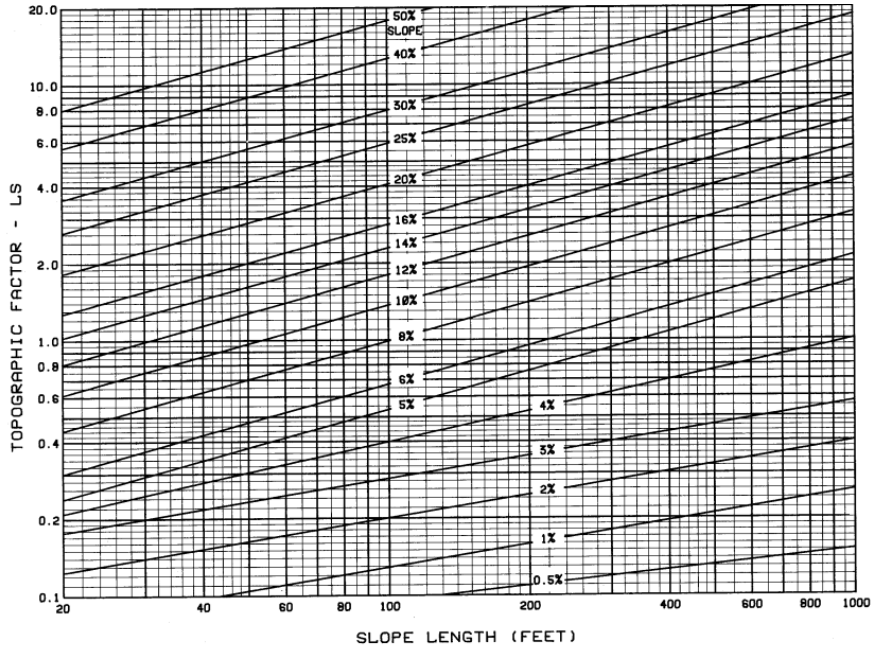

Figure 2.4.3 -- Slope-effect chart (Topographic Factor, LS)

The chart was derived from the equation:

$$L = \left(\frac{\lambda}{22.13}\right)^m 65.41\ \sin^2\theta + 4.56\ \sin\theta + 0.065$$

- *Cover-management factor C*

Vegetation acts as a protective layer, the above-ground components, such as leaves and stems, absorb some of the energy of falling raindrops, and dissipate the energy of running water by imparting

roughness to the flow, thereby reducing its velocity, while the below-ground components contribute to the slope stability because of the cohesive effect of the tree roots. Factor C is the ratio of soil loss from land cropped under specific conditions to the corresponding loss from clean-tilled, continuous fallow (Wischmeier and Smith, 1978a). The actual soil loss depends on the combination of cover, crop sequence, and management practices. It also depends on the particular stage of growth and development of the vegetal cover at the time of rain. The variations in rainfall distribution within the year also affect the crop management factor. For arable farming, the year is divided into crop stage periods defined so that cover and management effects may be considered uniform within each period. The crop stage periods are defined as follows:

Period F (rough fallow) – Inversion ploughing to secondary tillage.

Period SB (seedbed) – Secondary tillage for seedbed preparation until the crop has developed 10 percent canopy cover.

Period 1 (establishment) – End of SB until the crop has developed a 50 percent canopy cover.

Period 2 (development) – End of period 1 until canopy cover reaches 75 percent.

Period 3 (maturing crop) – End of period 2 until crop harvest.

Period 4 (residue of stubble) – Harvest to ploughing or new seeding.

To derive site values of C, soil loss ratios (SLRs) must be computed for the individual crop stage periods. And for a given crop. The soil loss ratio (SLR) is an estimate of the ratio of soil loss under actual conditions to losses experienced under reference conditions. The SLR for the given condition will be:

$$SLR = PLU \text{ x } CC \text{ x } SC \text{ x } SR \text{ x } SM$$

Where:
PLU is the prior- land use subfactor.
CC is the canopy-cover subfactor.
SC is the surface-cover subfactor.
SR is the surface-roughness subfactor.
SM is the soil-moisture subfactor.

The SLR ratio's values are obtained from tables summarising data collected over many years by the United States Natural Resources Conservation Service at their experimental stations. Once the SLR's have been calculated for each time interval, they must be weighted by the fraction of the rainfall and runoff erosivity (EI) associated with the corresponding period time, and these weighted values are combined into an overall C factor value. The following Figure 2.4.4 gives typical ranges of values for different crops and management systems:

Practice	Average annual C-factor
Bare soil	1.00
Forest or dense shrub, high mulch crops	0.001
Savanna or prairie grass in good condition	0.01
Overgrazed savanna or prairie grass	0.10
Maize, sorghum or millet; high productivity; conventional tillage	0.20–0.55
Maize, sorghum or millet; low productivity; conventional tillage	0.50–0.90
Maize, sorghum or millet; high productivity; chisel ploughing into residue	0.12–0.20
Maize, sorghum or millet; low productivity; chisel ploughing into residue	0.30–0.45
Maize, sorghum or millet; high productivity; no or minimum tillage	0.02–0.10
Cotton	0.40–0.70
Meadow grass	0.01–0.025
Soya beans	0.20–0.50
Wheat	0.10–0.40
Rice	0.10–0.20
Groundnuts	0.30–0.80
Palm trees, coffee, cocoa with cover crops	0.10–0.30
Pineapple on contour; residue removed	0.10–0.40
Pineapple on contour; with surface residue	0.01
Potatoes; rows downslope	0.20–0.50
Potatoes; rows across slope	0.10–0.40
Cowpeas	0.30–0.40
Strawberries; with weed cover	0.27
Pomegranate; with weed cover	0.08
Pomegranate; clean-weeded	0.56
Ethiopian tef	0.25
Sugar cane	0.13–0.40
Yams	0.40–0.50
Pigeon peas	0.60–0.70
Mungbean	0.04
Chilli	0.33
Coffee: after first harvest	0.05
Plantains: after establishment	0.05–0.10
Papaya	0.21

Figure 2.4.4- C-factor values for the Universal Soil Loss Equation (Morgan, 2006)

- *Support practices factor P*

The support practice factor P is the ratio of soil loss with a specific support practice to the corresponding loss with upslope and downslope tillage (Wischmeier and Smith, 1978a). These practices affect erosion by modifying the flow pattern, grade, or direction of surface runoff and by reducing the amount of rate of runoff. For cultivated land, the support practices considered include:

- contouring (tillage and planting on or near the contour).
- stripcropping.
- terracing.
- subsurface drainage.

The practice of tillage and planting on the contour protects against erosion from moderate to low intensity storms, but the protection is negligible for the occasional severe storms. Contouring is also affected by the slope length. Values for P factor and slope-length limits for contour support practices are given in Figure 2.4.5:

Land slope percent	P value	Maximum length[1]
		Feet
1 to 2	0.60	400
3 to 5	.50	300
6 to 8	.50	200
9 to 12	.60	120
13 to 16	.70	80
17 to 20	.80	60
21 to 25	.90	50

[1] Limit may be increased by 25 percent if residue cover after crop seedlings will regularly exceed 50 percent.

Figure 2.4.5 – P values and slope-length limits for contouring (Wischmeier and Smith, 1978a)

Strip cropping is a practice in which contoured strips of sod are alternated with equal-width strips of row crops or small grains. Recommended values for contour strip cropping are given in Figure 2.4.6:

Land slope percent	P values[1]			Strip width[2]	Maximum length
	A	B	C		
				Feet	Feet
1 to 2	0.30	0.45	0.60	130	800
3 to 5	.25	.38	.50	100	600
6 to 8	.25	.38	.50	100	400
9 to 12	.30	.45	.60	80	240
13 to 16	.35	.52	.70	80	160
17 to 20	.40	.60	.80	60	120
21 to 25	.45	.68	.90	50	100

[1] P values:
A For 4-year rotation of row crop, small grain with meadow seeding, and 2 years of meadow. A second row crop can replace the small grain if meadow is established in it.
B For 4-year rotation of 2 years row crop, winter grain with meadow seeding, and 1-year meadow.
C For alternate strips of row crop and small grain.
[2] Adjust strip-width limit, generally downward, to accommodate widths of farm equipment.

Figure 2.4.6 – P values, maximum strip widths, and slope-length limits for contour strip-cropping (Wischmeier and Smith, 1978a)

Terraces are a series of horizontal ridges made on the hillside. There are several types of terraces. The broad base type is common on gently sloping land, and the steep backslope terrace is most common on steeper land. Terracing divides the slope into segments equal to the horizontal terrace interval. The horizontal terrace interval for broad base terraces is the distance from the centre of the ridge to the centre of the channel for the terrace below. For steep backslope terraces, it is the distance from the point where cultivation begins at the base of the ridge to the base of the front slope of the terrace below. Values for P for contour farming terraced fields are listed in Figure 2.4.7:

Land slope (percent)	Farm planning		Computing sediment yield[3]	
	Contour factor[2]	Stripcrop factor	Graded channels sod outlets	Steep backslope underground outlets
1 to 2	0.60	0.30	0.12	0.05
3 to 8	.50	.25	.10	.05
9 to 12	.60	.30	.12	.05
13 to 16	.70	.35	.14	.05
17 to 20	.80	.40	.16	.06
21 to 25	.90	.45	.18	.06

[1] Slope length is the horizontal terrace interval. The listed values are for contour farming. No additional contouring factor is used in the computation.

[2] Use these values for control of interterrace erosion within specified soil loss tolerances.

[3] These values include entrapment efficiency and are used for control of offsite sediment within limits and for estimating the field's contribution to watershed sediment yield.

Figure 2.4.7 – P values for contour-farmed terraced fields (Wischmeier and Smith, 1978a)

Finally, an overall P-factor value is computed as a product of P subfactors for individual support practices, which are typically used in combination.

Although the Universal Soil Loss Equation was widely used worldwide for estimating sheet and rill erosion, it is worth noting that soil erosion cannot be adequately described merely by multiplying together six-factor values. In addition, the equation has some limitations, one limitation is that its database is restricted to the USA east of the Rocky Mountains, to slopes where cultivation is permissible, normally 0-7°, and to soil with low content of montmorillonite, so it needs of some modifications to be applied more widely. Furthermore, since it was designed for interill and rill erosion, it should not be used to predict gully or stream-bank erosion, and care should be taken in using it to estimate the contribution of hillslope erosion to basin sediment yield because it does not estimate deposition of material or incorporate a sediment delivery ratio.

2.4.2 CONCEPTUAL MODELS: WATER AND TILLAGE EROSION MODEL AND SEDIMENT DELIVERY MODEL (WaTEM/SEDEM)

WaTEM/SEDEM is a spatially distributed model for the calculation of sediment delivery to river channels at a catchment scale (Van Oost et al., 2000a; Van Rompaey et al., 2001). The model has three main components:

1) - Water erosion component

The water erosion component consists of an assessment of the mean annual soil erosion rate based on a 2D application of the RUSLE methodology:

$$E = R \times K \times LS_{2D} \times C \times P$$

Where:

E is the mean annual soil loss (kg m^{-2} $year^{-1}$)

R is the rainfall erosivity factor (MJ mm m^{-2} h^{-2} yr^{-1})

K is the soil erodibility factor (kg h MJ^{-1} mm^{-1})

LS is the slope length factor.

C is the crop management factor.

P is the erosion control practice factor.

In order to adapt the RUSLE to the complex topography of 2D landscape and to account for effects of flow convergence, it is used the unit contributing area LS_{2D} proposed by (Desmet and Govers, 1996), i.e. the upslope drainage area per unit of contour length.

2) - Transport capacity component

The transport capacity component consists of an assessment of the mean annual transport capacity (TC kg m^{-1}) for each grid cell. Van Oost et al. (2000b) considered that the transport capacity on a given slope segment is directly proportional to the potential for rill (and ephemeral gully) erosion. Deposition occurs when the sediment inflow exceeds the transport capacity, so the amount of material leaving a point equals the transport capacity. The transport capacity can be estimated as:

$$T_C = k_{TC}\, E_{PR}$$

Where:

T_C is the transport capacity (kg m^{-1} $year^{-1}$)

K_{TC} is the transport capacity coefficient (m)

E_{PR} is the potential for rill erosion (kg m^{-2} yr^{-1})

The transport capacity coefficient $K_{TC,}$ expressed in meters, is the only model parameter that needs to be calibrated because it is scale-dependent. It represents the slope length needed to produce an amount of sediment equal to the amount produced under similar topographic conditions on a bare surface with an identical slope gradient (Verstraeten, 2006). The coefficient is dependent on land cover.

The potential for interill erosion E_{PIR} (kg m^{-2} yr^{-1}) is a theoretical erosion rate assuming the field is bare and no conservation measures are undertaken. It can be estimated according to the following equation:

$$E_{PIR} = R\, K\, (LS_{2D} - 4.1\, S_{IR})$$

Where:

R is the rainfall erosivity factor (MJ mm m^{-2} h^{-1} $year^{-1}$)

K is the soil erodibility factor (kg h MJ^{-1} mm^{-1})

LS_{2D} is the slope -length factor

S_{IR} is the interill slope gradient factor

3) Sediment routing algorithm component

Once the mean annual erosion rate and the mean annual transport capacity are known at each grid cell, a routing algorithm is used to transfer the eroded sediment from the source to the river network. Starting

from the highest grid cells of the DEM, the sediment is routed downslope toward the river system using a runoff pattern calculated using a multiple-flow algorithm. Sediment is routed along this runoff pattern towards the river, considering each pixel's local transport capacity. Mass balance is computed for each cell, and the sediment input is added to the amount of soil erosion in that cell. If the sum of the sediment input and the local sediment production is lower than the transport capacity, then all the sediment is routed downslope. If the sum exceeds the transport capacity, sediment deposition will occur. As soon as all the sediment reaches a stream cell, it is directly delivered to the catchment outlet.

The output of the model is a pixel map representing the amount of erosion or sediment deposition at each pixel. Furthermore, the Sediment Yield (SY, in t yr^{-1}) can be expressed as an absolute value and an area-Specific Sediment Yield value (SYY, in t ha^{-1} $year^{-1}$) can be calculated when the absolute sediment yield value is divided by the catchment area. It is worth noting that WaTEM/SEDEM can identify major sediment source areas on the hillslope, but it does not model permanent gully erosion or fluvial processes such as riverbank, floodplain sedimentation and channel storage; this can introduce a bias during model calibration in catchments where stream processes are important.

2.4.3 Physically Based Models: Soil & Water Assessment Tool (SWAT)

The Soil and Water Assessment Tool (SWAT) is a physically based, semi-distributed, continuous-time, watershed-scale and eco-hydrological model developed by the United States Department of Agriculture (USDA) Agricultural Research Service (ARS) to predict and assess the impact of climate change and agricultural land management practices on water, sediment and agricultural chemical yields in large watersheds with a variety of soil types, land uses, and management strategies (Neithsch et al., 2009).

SWAT operates on a daily time step, providing output files at daily, monthly, and yearly time scales (G. Arnold et al., 2012).

The QGis extension, QSWAT, allows the SWAT model to be executed within a geographic information system (GIS) while providing tools to develop and run the model.

In SWAT, a watershed is partitioned into multiple sub-watersheds interconnected by stream networks based on digital elevation model (DEM) data. A single reach (stream) is created in each subbasin based on flow accumulation principles and direction. Upon watershed delineation, the SWAT model further discretizes every sub-watershed into several spatially unrelated hydrologic response units (HRUs), or HRUs. HRUs consist of unique land use, soil, and surface slope combinations and are the minor modeling units used in the SWAT model. HRU discretization allows the model to account for watershed spatial variability while reducing overall running time.

In the SWAT model, the hydrologic cycle is simulated based on the water balance equation that incorporates principles of mass and energy continuity:

$$SW_t = SW_0 + \sum_{i=1}^{t} \left(\mathrm{P} - Q_{surf} - \mathrm{ET} - W_{seep} - Q_{gw} \right)$$

Where:

- SW_t is the soil water content (mm) on day t;
- SW_0 is the initial soil water content (mm) on day i, t is the time in days;
- P is the precipitation (mm) on day i;
- Q_{surf} is the surface runoff (mm) on day i;
- ET is the evapotranspiration (mm) on day i;
- w_{seep} is the amount of water (mm) entering the vadose zone from the soil profile on day i;
- Q_{gw} is the return subsurface flow (mm) on day i.

The hydrologic cycle for the watershed is analyzed into two major divisions: the land phase at the HRU level and the water or routing phase.

1) Land phase at the HRU level

In this phase, the SWAT model estimates the hydrologic components (flow, sediment, nutrient, and pesticide loadings) for each HRU, assuming there is no interaction between HRUs in one subbasin. Then, loadings (runoff with sediment, nutrients, etc., transported by runoff) from each HRU are calculated separately and then summed together to determine the total loadings from the subbasin.

Hydrology

Once water is introduced to the system with precipitation (Figure 2.4.8), climatic processes are the main source of energy affecting the movement of water in the land phase of the hydrologic cycle. The most basic climatic input data SWAT requires are precipitation, air temperature, solar radiation, wind speed, and relative humidity. Since the accuracy of the model results is significantly improved using measured data, obtaining measured data from gauges in or near the watershed is strongly recommended if possible. However, when measured data is unavailable, SWAT uses data simulated by a weather generator program from average monthly values.

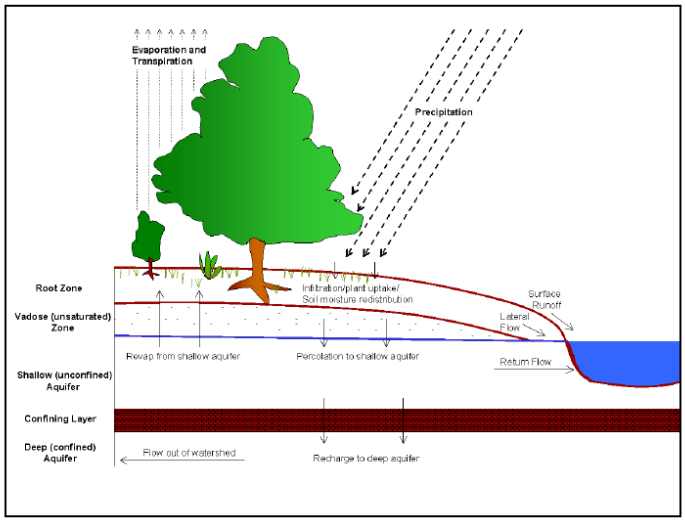

Figure 2.4.8 – Schematic representation of the hydrologic cycle (from SWAT Theoretical Documentation, version 2009)

The primary mechanism of the hydrologic cycle is EVAPOTRANSPIRATION, this term includes all the processes by which water is converted to water vapor, and it is removed from the watershed. Potential evapotranspiration (PET) is the rate at which evapotranspiration occurs from a large area completely and uniformly covered with growing vegetation with access to an unlimited supply of soil water. SWAT has three options for estimating PET: the Penman-Monteith method (Allen et al., 1989), which works with solar radiation, air temperature, relative humidity, and wind speed; and the Priestly-Taylor method (Priestley and Taylor, 1972) which requires solar radiation, relative humidity and air temperature, and the Hargreaves method (Hargreaves and Samani, 1985) that requires only air temperature. Once total potential evapotranspiration is determined, the actual amount of sublimation and evapotranspiration from the soil is calculated.

The water reaching the soil surface will infiltrate the soil profile or flow overland as runoff. Surface runoff, or overland flow, is the flow that occurs along the sloping surface. Using daily rainfall amounts, SWAT simulates surface runoff volumes and peak runoff rates for each HRU, providing two mechanisms for estimating SURFACE RUNOFF VOLUME: the SCS-CN curve number procedure (Soil Conservation Service, 1972) and the Green & Ampt infiltration method (Ampt and Heber Green, 1911). In SCS-CN empirical approach, two assumptions are made. First, it is assumed that a watershed can hold a certain maximum amount of precipitation, S_{max}

$$S_{max} = I_a + F_\infty$$

Where:

S_{max} is the maximum retention capacity of the watershed.

I_a is the initial abstraction representing the amount of rainfall (Rday) retained in the watershed storage as interception, infiltration, and surface storage before runoff begins.

Considering that F is the retention, i.e., the amount of rainfall falling after the initial abstraction is satisfied but does not contribute to the storm flow (equivalent to the volume of water infiltrated). F_∞ is the total amount of water retained as t became very large (the cumulative infiltration amount).

Second, it is also assumed that during the storm:

$$\frac{Q_{surf}}{(R_{day} - I_a)} = \frac{F}{S_{max}}$$

Q_{surf} is the accumulated runoff, and the quantity ($R_{day} - I_a$) is the excess precipitation or potential runoff. The idea inside this equation is that the more of the potential storage that has been exhausted (cumulative infiltration, F, converges on Smax), the more of the 'excess rainfall', or 'potential runoff', ($R_{day} - I_a$), will be converted to runoff.

Considering that by definition:

$$F = R_{day} - I_a - Q_{surf}$$

Combination of the two equations leads to the rainfall-runoff equation:

$$Q_{surf} = \frac{(R_{day} - I_a)^2}{(R_{day} - I_a + S_{max})}$$

Where:

Q_{surf} is the accumulated runoff (mm H_2O)

R_{day} is the rainfall depth for the day (mm H_2O)

I_a is the initial abstractions (mm H_2O)

S is the retention parameter (mm H_2O).

Based on a regression analysis of recorded rainfall and runoff data from small drainage basins, the following average relationship was found:

$$I_a = \mu S_{max}$$

Where:

μ is the initial abstraction ratio.

Thus:

$$R_{day} - I_a = R_{day} - 0.2\ S_{max}$$

Finally:

$$Q_{surf} = \frac{(R_{day} - 0.2\ S_{max})^2}{(R_{day} + 0.8\ S_{max})}$$

With this equation, the problem of predicting surface runoff is reduced to estimating a single value, S_{max}. The retention parameter is spatially variable and is primarily based on soils, land use, management, and slope, as well as temporally on water content (Figure 2.4.9). It is defined as:

$$S_{max} = 254.0 \left(\frac{100}{CN} - 1\right)$$

where *CN* is a dimensionless index of storm-runoff generation capacity for the day, varying from 0 to 100.

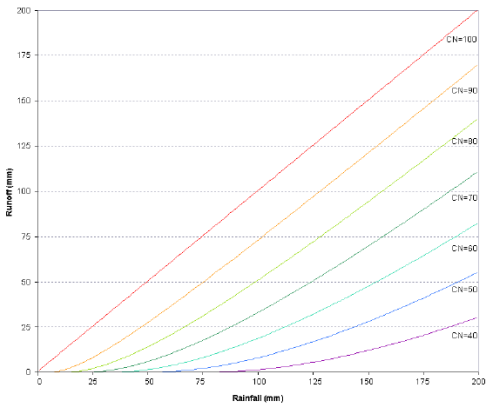

Figure 2.4.9 – Relationship of runoff to rainfall in SCS curve number method

A higher curve indicates a large runoff response from a watershed with a fairly uniform soil with a low infiltration capacity. A lower curve is a smaller response expected from a watershed with permeable soil, with a relatively high spatial variability in infiltration capacity.

The CN parameter is related to land use, land treatment, hydrological condition, hydrological soil group, and antecedent soil moisture condition in the drainage basin.

Hydrologic Soil Groups are defined in SCS Sil Survey reports considering the minimum rate of infiltration obtained for a bare soil after prolonged wetting as follows (Table 2.4.3):

Table 2.4.3 – Hydrologic Soil Groups as defined in SCS Soil Survey Report (Soil Conservation Service, 1972)

CLASSIFICATION	TYPE OF SOIL
A (Low runoff potential)	Soils with high infiltration capacities, even when thoroughly wetted. They chiefly consist of sand and gravels, deep and well drained. They have a high rate of water transmission.
B	Soils with moderate infiltration rates when thoroughly wetted. Moderately deep to deep, moderately well to well drained, with moderately fine to moderately coarse textures
C	Soils with slow infiltration rates when thoroughly wetted. Usually have a layer that impedes vertical drainage or have a moderately fine to fine texture. They have a moderate rate of water transmission.
D (High runoff potential)	Soils with very slow infiltration rates when thoroughly wetted. Chiefly clays with a high swelling potential; soils with a high permanent water table; soil with a clay layer at or near the surface; shallow soils over nearby impervious materials. They have a very slow rate of water transmission

The land use or cover, in SCS method, is distinguished into (Figure 2.4.10):

- Fallow: The agricultural land use has the highest potential for runoff because the land is kept bare.
- Row crops: field crops planted in rows far enough apart that most soil surface is directly exposed to rainfall.
- Small grain: planted in rows close enough that the soil surface is not directly exposed to rainfall.
- Close-seeded legumes or rotational meadow: either planted in close rows or broadcasted. This kind of cover usually protects the soil throughout the year.
- Pasture or range: native grassland used for grazing, whereas meadow is grassland protected from grazing and generally mown for hay.
- Woodlands: usually small, isolated groves of trees raised for farm use.

For each cover category is chosen a treatment or practice that includes mechanical practise such as contouring or terracing, and management practice such as rotation of crop, grazing control, or burin, and it also chosen a hydrological condition, distinguished in poor, fair and good (Figure 2.4.10).

Land use or cover, treatment or practice, hydrological condition, and hydrological soil group together are called the Hydrological Soil-Cover Complex, and their relation to the CN value is usually given for average conditions, i.e. Antecedent Soil Moisture Condition Class II.

Land use or cover	Treatment or practice	Hydrological condition	Hydrological soil group			
			A	B	C	D
Fallow	Straight row	Poor	77	86	91	94
Row crops	Straight row	Poor	72	81	88	91
	Straight row	Good	67	78	85	89
	Contoured	Poor	70	79	81	88
	Contoured	Good	65	75	82	86
	Contoured/terraced	Poor	66	74	80	82
	Contoured/terraced	Good	62	71	78	81
Small grain	Straight row	Poor	65	76	84	88
	Straight row	Good	63	75	83	87
	Contoured	Poor	63	74	82	85
	Contoured	Good	61	73	81	84
	Contoured/terraced	Poor	61	72	79	82
	Contoured/terraced	Good	59	70	78	81
Close-seeded legumes or rotational meadow	Straight row	Poor	66	77	85	89
	Straight row	Good	58	72	81	85
	Contoured	Poor	64	75	83	85
	Contoured	Good	55	69	78	83
	Contoured/terraced	Poor	63	73	80	83
	Contoured/terraced	Good	51	67	76	80
Pasture range		Poor	68	79	86	89
		Fair	49	69	79	84
		Good	39	61	74	80
	Contoured	Poor	47	67	81	88
	Contoured	Fair	25	59	75	83
	Contoured	Good	6	35	70	79
Meadow (permanent)		Good	30	58	71	78
Woodlands (farm woodlots)		Poor	45	66	77	83
		Fair	36	60	73	79
		Good	25	55	70	77
Farmsteads			59	74	82	86
Roads, dirt			72	82	87	89
Roads, hard-surface			74	84	90	92

Figure 2.4.10 – Runoff curve numbers for Hydrological Soil-Cover Complexes under AMC class II (Soil Conservation Service, 1972)

In SCS-CN method, the soil moisture condition in the drainage basin is classified into three Antecedent Moisture Condition (AMC):

AMC I: The soil I the drainage basin is practically dry (i.e., the soil moisture content is at the wilting point)

AMC II: Average condition.

AMC III: The soils in the drainage basins are practically saturated from antecedent rainfalls (i.e., the soil moisture content is at field capacity).

To determine which AMC Class is the most appropriate for drainage basin under consideration, the original rainfall records must be used. The average of the 5-day total historical rainfall preceding the two historical rainfall events selected in the frequency analysis determines the AMC class (Table 2.4.4).

Table 2.4.4 - Seasonal rainfall limits for AMC classes (Soil Conservation Service, 1972)

AMC category	Rainfall depth in the previous 5 days (mm)	
	Dormant season	Growing season
AMC-I	<12.7	<35.6
AMC-II	12.7 – 27.9	35.6– 53.3
AMC-III	>27.9	>53.3

Finally, it is possible to compute CN values based on the relationships for CN(I) (valid for AMC I) and CN(II) (valid for AMC II).

The Green &Ampt method requires sub-daily precipitation data and calculates infiltration as a function of the wetting front matric potential and effective hydraulic conductivity. As the water infiltrates into the soil, the model assumes the soil above the wetting front is entirely saturated, and there is a sharp break in moisture content at the wetting front (Figure 2.4.11). SWAT calculates the amount of water entering the soil. The water that does not infiltrate becomes surface runoff.

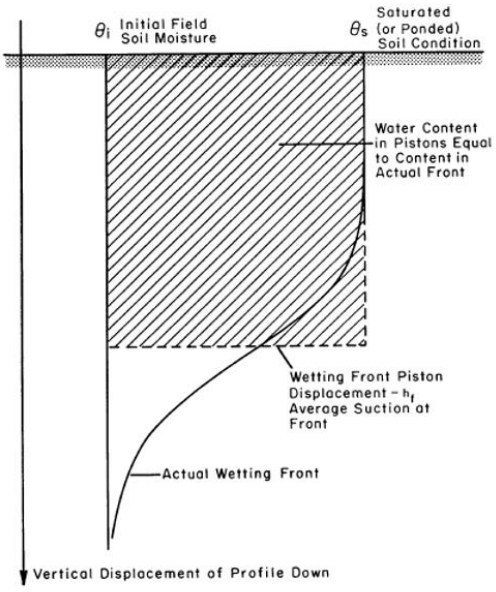

Figure 2.4.11 – Conceptual representation of the Green and Ampt method (from https://www.hec.usace.army.mil/)

SWAT simulates also the PEAK RUNOFF RATE an indicator of the erosive power of the storm used to predict sediment loss. It is the maximum runoff flow rate that occurs during and immediately after a rainfall event; it is influenced by the severity of the storm and the relative importance of various pathways by which rainwater enters the stream. It is calculated by SWAT with a modified rational method based on the assumption that if a rainfall of intensity i begin at time t= 0 and continues indefinitely, the rate of runoff will increase until the time of concentration, $t = t_c$.

The time of concentration, t_c, is defined as the time for runoff to travel from the hydraulically most distant point in the drainage basin to the outlet or point of interest; in this time, the entire subbasin area contributes to flow at the outlet. It is also defined as the distance between the end of excess rainfall and

the inflection point in the recession limb of the hydrograph (Figure 2.4.12). The modified rational formula used to estimate the peak flow rate is:

$$q_{peak} = \frac{a_{tc}\ Q_{surf}\ Area}{3.6\ t_c}$$

Where:

$q_{peak}$is the peak runoff rate ($m^3\ s^{-1}$)

a_{tc} is the fraction of daily rainfall that occur during time of concentration.

Q_{surf} is the surface runoff (mm H_2O)

t_c is the time of concentration for the subbasin (hr), estimated using Manning's formula considering both overland and channel flow.

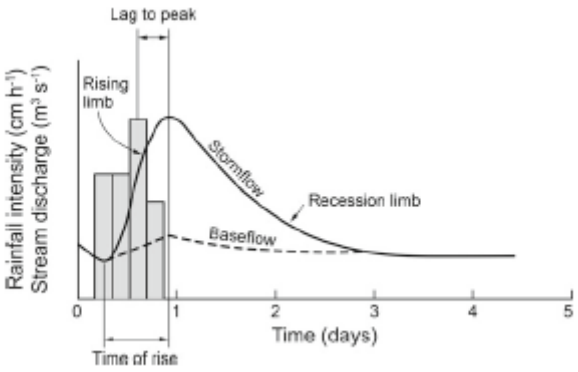

Figure 2.4.12 - Streamflow hydrograph resulting from a rainstorm (Allan et al., 2021)

Once water has infiltrated, it may undergo evapotranspiration or move by percolation or bypass through the vadose zone until the aquifer. From here, it may slowly make its way to the surface-water system as lateral subsurface flow or return flow.

LATERAL SUBSURFACE FLOW, or interflow, is the streamflow contribution that originates below the surface but above the zone where rocks are saturated with water. It can be significant in areas with soils having high hydraulic conductivities in surface layers and an impermeable or semipermeable layer at shallow depths. The saturated conductivity of the soil layer, slope, and water content governs the flow rate.

Return flow, or BASEFLOW, is the volume of the streamflow originating from groundwater (Figure 2.4.13).

In SWAT, the shallow aquifer contributes to the base flow to the main channel or reach within the watershed.

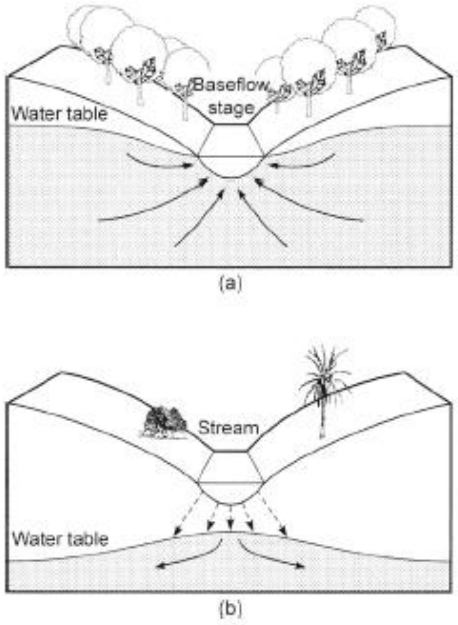

Figure 2.4.13 – The interaction between a river and a groundwater. In (a) the groundwater is contributing to the stream, while in (b) the opposite is occurring (Allan et al., 2021).

The steady-state response of groundwater flow to recharge is:

$$Q_{gw} = \frac{800\, K_{sat}}{{L_{gw}}^2} h_{wtbl}$$

Where:

Q_{gw} is the groundwater flow, or baseflow, into the main channel on day (mmH_2O)

K_{sat} is the hydraulic conductivity of the aquifer (mm/day)

L_{gw} is the distance from the ridge or subbasin divide for the groundwater system to the main channel (m)

h_{wtbl} is the water table height (m)

Erosion

Erosion caused by rainfall and runoff is computed with the Modified Universal Soil Loss Equation for each sub-watershed or HRU (Williams, 1975a).

In MUSLE, average annual gross erosion is predicted as a function of runoff factor as follows:

$$sed = 11.8\,(Q_{surf}\, q_{peak} area_{hru})^{\,0.56} K_{USLE} C_{USLE}\, P_{USLE}\, LS_{USLE}\, CFRG$$

Where:

sed is the sediment yield on a given day (metric tons)

Q_{surf} is the surface runoff volume (mm H_2O/ha)

q_{peak} is the peak runoff rate (m^3/s)

$area_{hru}$ is the area of HRU (ha)

K_{USLE} is the USLE soil erodibility factor (0.013 metric ton m^2 hr / (m^3 metric ton cm))

C_{USLE} is the cover and management factor.

P_{USLE} is the USLE support practice factor.

LS_{USLE} is the USLE topographic factor.

$CFRG$ is the coarse fragment factor.

Management

SWAT allows the definition of the management operations in each HRU, specifying the timing. The management information that can be incorporated into a simulation concern:

- Planting/beginning of growing season.
- Harvest operation.
- Grazing operations.
- Kill/end of growing season.
- Tillage.
- Fertiliser application.
- Pesticide application.

2) Water and Sediment Routing Phase

Determined the loadings of water, sediment, nutrient, and pesticides from each HRUs, they are summed together to determine the total loadings from the subbasin. Then, the subbasin's loading are routed through the channel network of the watershed in the associated reach segment.

SWAT models the main channel processes, i.e., water, sediment, and other constituent movement in the stream network (Figure 2.4.14).

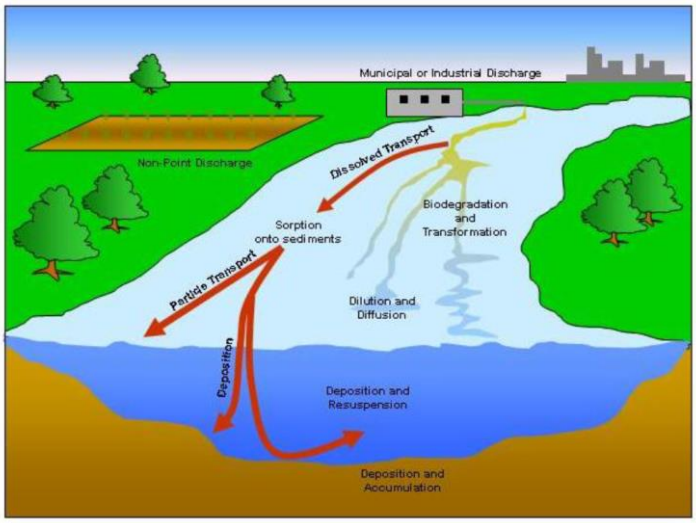

Figure 2.4.14 – In-stream processes modelled by SWAT (SWAT THEORETICAL DOCUMENTATION, VERSION 2009)

Water is routed through the channel network using the Variable Storage Routing Method or the Muskingum River Routing Method; they are variations of the kinematic wave model.

The VARIABLE STORAGE ROUTING METHOD was used in HYMO model by (Williams, 1975b). For a given reach segment, storage routing is based on the continuity equation:

$$V_{in} - V_{out} = \Delta V_{stored}$$

Where:

V_{in} is the volume of inflow during the time step (m^3 H_2O)

V_{out} is the volume of outflow during the time step (m^3 H_2O)

ΔV_{stored} is the change in volume of storage during the time step (m^3 H_2O)

The volume of outflow is calculated with the following equation:

$$V_{out,2} = SC\left(V_{in} + V_{stored,1}\right)$$

Where:

$V_{out,2}$ is the volume of outflow at the end of the time step (m^3 H_2O).

SC is a storage coefficient that depends on the length of the time step and travel time.

V_{in} is the volume of inflow at the beginning of the time step (m^3 H_2O).

$V_{stored,1}$ is the volume of storage at the beginning of the time step (m^3 H_2O).

The MUSKINGUM RIVER ROUTING METHOD models the storage volume in a channel length as a combination of wedge and prism storages (Figure 2.25).

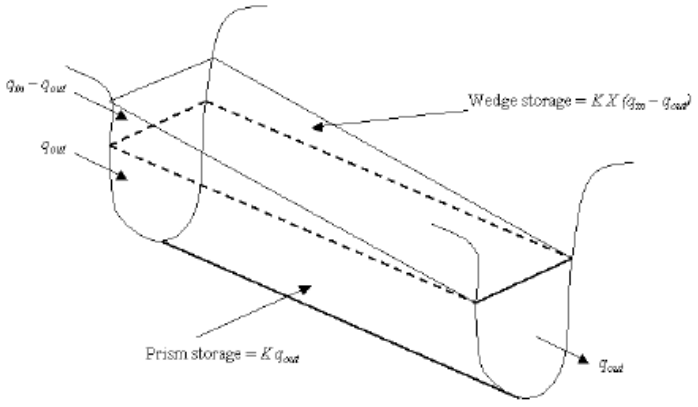

Figure 2.4.15 – Prism and wedge storage in a reach segment (SWAT THEORETICAL DOCUMENTATION VERSION 2009)

When a flood wave advances into a reach, inflow exceed outflow and a wedge of storage is produced. If the flood wave recedes, outflow exceeds inflow in the reach segment, producing a negative wedge. A prism of storage is the volume of constant cross-section along the reach length. The total storage will be:

$$V_{stored} = K\, q_{out} + K\, X\, (q_{in} - q_{out})$$

Where:

V_{stored} is the storage volume (m^3 H_2O)

K is the storage time constant for the reach (s)

q_{out} is the discharge rate (m^3/s)

X is the weighting factor that controls the relative importance of inflow and outflow in determining the storage in a reach.

q_{in} is the inflow rate (m^3/s)

The volume of water flowing out of the reach during the time step is calculated with the following equation:

$$V_{out,2} = C_1\, V_{in,2} + C_2 V_{in,1} + C_3 V_{out,1}$$

Where:

$V_{out,2}$ is the volume of outflow at the end of the time step (m^3 H_2O).

$V_{in,1}$ is the volume of inflow at the beginning of the time step (m^3 H_2O).

$V_{in,2}$ is the volume of the inflow at the end of the time step (m^3 H_2O).

$C_1 + C_2 + C_3 = 1$ are parameters that depend on K and X

SWAT considers the volume of outflow determined by the above equations as the net amount of water removed from the reach, i.e. the amount of outflow to the next reach segment reduced by the amount of the losses by transmission, evaporation, and other water losses.

Concerning the sediment routing, SWAT considers both the components of the sediment transport: Landscape Contribution and Channel Contribution.

The total sediment yield calculated by MUSLE takes some time to reach the stream channel as it is routed through grassed waterways, vegetative filter strips, and ponds in the landscape component. The total sediment trapping is calculated by utilizing these landscape elements to assume that coarser sediments like sand and large aggregate settle and trap first, followed by finer sediments like clay. This is responsible for controlling the final particle size distribution of sediment reaching the stream from the landscape portion.

Regarding the channel component, the sediment is routed through the main routing reach from upland subbasins and added to downstream reaches. Four physically-based approaches are employed in SWAT to model sediment transport, bank erosion, and bed erosion in channels with different bed materials and sediment deposition. The stream power (transport capacity) and the sediment supply are the factors that control channel erosion. The erosion occurs if the stream power index of the stream is high and the sediment load from upstream region is less than this transport capacity. The maximum concentration of sediment that can be transported by water (metric ton/m^3) is a non-linear function of peak velocity:

$$conc_{sed,max} = f\ (peak\ velocity)$$

The default method used to calculate $conc_{sed}$ is the SIMPLIFIED BAGNOLD METHOD, that depends on the peak channel velocity. The maximum concentration of sediment that can be transported by water (ton/m^3 or Kg/L) is calculated:

$$conc_{sed,max} = c_{sp} {v_{ch,pk}}^{spexp}$$

Where:

c_{sp} is a coefficient defined by the user.

$v_{ch,pk}$ is the peak channel velocity (m/s) that depends on the peak flow rate (m^3/s) and the cross-sectional area of the flow in the channel(m^2). The peak flow rate is dependent on the average rate of flow.

$spexp$ is an exponent defined by the user, varying between 1.0 and 2.0.

If the concentration of sediment in the reach at the beginning of the time step $conc_{sed,i}$ is higher than $conc_{sed,max}$ deposition is the dominant process in the reach, and the amount of sediment deposited in the reach segment, sed_{dep} (metric tons) will be:

$$sed_{dep} = \left(conc_{sed,i} - conc_{sed,max}\right) V_{ch}$$

Where:

V_{ch} is the volume of water in the reach segment (m^3 H_2O).

If $conc_{sed,i}$ is lower than $conc_{sed,max}$ degradation is the dominant process, and the amount of sediment incorporated into the reach, sed_{deg} (metric tons), will be:

$$sed_{deg} = \left(conc_{sed,max} - conc_{sed,i}\right) V_{ch}\, K_{ch}\, C_{ch}$$

Where:

K_{ch} is the channel erodibility factor, it is a function of the properties of the bed or bank materials.

C_{ch} is the channel cover factor, it is defined as the ratio of degradation from a channel with a specific vegetative cover to the corresponding degradation from a channel with no vegetative cover. The vegetation reduces the stream velocity and its erosive power near the bed surface.

Finally, the final amount of sediment in the reach, sed_{ch} (metric tons), is determined as:

$$sed_{ch} = sed_{ch,i} - sed_{dep} + sed_{deg}$$

And the amount of sediment transported out of the reach, sed_{out} (metric tons) will be:

$$sed_{out} = sed_{ch} \frac{V_{out}}{V_{ch}}$$

Where:

V_{out} is the volume of outflow during the time step (m^3 H_2O)

V_{ch} is the volume of water in the reach segment (m^3 H_2O)

This method limits the erosion only by the transport capacity, and it does not consider the particle size distribution through the channel reaches (all particles are assumed to be of silt size) and the partitioning between the stream bank and stream bed.

The potential erosion rate of bank and bed depends on the shear stress exerted by the water, this should be more than the critical shear stress, or the tractive force needed to remove the sediment particles, as shown in the following equations:

$$\xi_{bank} = k_{d,bank}(\tau_{e,bank} - \tau_{c,bank})\, 10^{-6}$$

$$\xi_{bed} = k_{d,bed}(\tau_{e,bed} - \tau_{c,bed})\, 10^{-6}$$

Where:

ξ is the erosion rates of the bank and bed (m/s)

k_d is the erodibility coefficient of bank and bed (cm^{-3}/N-s)

τ_c is the critical shear stress acting on bank and bed (N/m^2)

Using the above relationships, the potential bank and bed erosion rate (Metric tons per day) will be:

$$Bnkrte = \xi_{bank} \left(L_{ch}\, 1000\, depth \sqrt{1 + {Z_{ch}}^2} \right) \rho_{b,bank}\, 86400$$

$$Bedrte = \xi_{bed}\, (L_{ch}\, 1000\, W_{btm})\, \rho_{b,bed}\, 86400$$

Where:

L_{ch} is the length of the channel (m)

$depth$ is the depth of water flowing in the channel (m)

W_{btm} is the channel bottom width (m)

$\rho_{b,bank}$, $\rho_{b,bed}$ are the bulk densities of channel bank and bed sediment (g/cm^3)

Finally, SWAT can also simulate downcutting and widening of the stream channel and update channel dimensions throughout the simulation.

3.0 SOIL EROSION IN SICILY

3.1 ANALYSIS OF HISTORICAL SUSPENDED SEDIMENT DATA

3.1.1 DISCHARGE AND SUSPENDED SEDIMENT DATA IN SICILY

With the establishment of the National Hydrographic Service in 1917, the systematic monitoring of river flow discharge, utilizing scientific methodologies and modern instrumentation, began in Italy. Over the subsequent years, the number of flow gauges and monitored rivers experienced substantial growth, peaking in the 1970s and 1980s. However, the continuous monitoring of numerous rivers was not consistently maintained. During the mid-1990s, the transfer of river monitoring authority from the National Hydrological Service to the Regional Hydrological Services resulted in a decline in the data collection for the majority of rivers. This decline led to a data gap of 5-15 years, contingent on the effectiveness of regional governments in establishing organization, acquiring equipment, training personnel, and defining responsibilities. In specific instances, certain recording stations were permanently dismantled while new ones were installed on the same rivers but in different locations. For this reason and due to technical constraints, the time series of sediment yield is commonly discontinuous, and only a few rivers/flow gauges have a relatively long and interrupted series of data (Billi and Fazzini, 2017).

The suspended sediment samples were collected every day (in case of flooding, more times a day) in the cross-section using a primordial sampler ("Bottiglia di Giandotti") (Figure 3.1.1), very similar to the Eijkelkamp® water trap (Bussettini et al., 2013). These samplers allow the collection of water samples at a specific hydrometric height. The samples were filtered in the lab to obtain the value of suspended sediment concentration. The data were then reported as mean monthly specific turbidity.

Figure 3.1.1 – Example of water sampler (Kemmerer water sampler, Eijkelkamp®)

From 1921 to the mid-1990s, the hydrometric data were published on the II part of the Hydrological Annales (Servizio Idrografico, 1916). For each river gauging station, the provided data included daily and monthly data on flow level/discharge, monthly maximum, minimum, and average discharge,

monthly precipitation on the catchment undertaken by the flow gauge, monthly runoff, runoff coefficient, flow duration data, and flow rating curve.

The Annals also reported the monthly maximum, minimum, and average suspended sediment discharge and sediment yield for a selected number of rivers (Fig. 3.1.2).

I - ◆ S. LEONARDO a MONUMENTALE

CARATTERISTICHE DELLA STAZIONE: *a*) Bacino di dominio 521.50 km^2 (parte permeabile 9%); altitudine media 578 *m* s. m.; distanza dalla foce 0.9 *km* circa; inizio delle osservazioni torbiometriche gennaio 1965. - *b*) Idrometro di riferimento (registratore) sp. s.; quota dello zero 1.50 *m* s. m. - *c*) Portata torbida (1965-66) annua media 16.00 *kg/s*; massima 4610.00 *kg/s*; minima 0.00 *kg/s*; torbidità specifica annua media: 4.270 kg/m^3 deflusso torbido unitario annuo medio: 963.00 $tonn/km^2$.

ELEMENTI CARATTERISTICI PER L'ANNO 1966

		ANNO	Gennaio	Febbraio	Marzo	Aprile	Maggio	Giugno	Luglio	Agosto	Settem.	Ottobre	Novem.	Dicemb.
Max	kg/m^3	13.700	7.730	1.880	4.920	5.810	4.790	0.127	0.177	0.000	0.000	0.077	13.700	2.890
	kg/s	165.00	84.20	39.00	88.60	165.00	130.00	0.10	0.01	0.00	0.00	0.01	38.70	21.40
Min.	kg/m^3	0.000	0.010	0.005	0.012	0.002	0.003	0.005	0.000	0.000	0.000	0.000	0.011	0.033
	kg/s	0.00	0.02	0.01	0.01	0.00	0.01	0.00	0.00	0.00	0.00	0.00	0.00	0.04
Med.	kg/m^3	1.330	1.440	0.287	1.350	2.640	1.700	0.030	0.000	0.000	0.000	0.071	1.520	0.730
	kg/s	3.74	9.93	1.63	9.48	11.10	8.92	0.02	0.00	0.00	0.00	0.01	1.47	2.08
10^3 *tonn*		118.00	26.60	3.95	25.40	28.70	23.90	0.06	0.00	0.00	0.00	0.02	3.81	5.85
tonn/km²		226.00	51.00	7.57	48.70	55.00	45.80	0.12	0.00	0.00	0.00	0.04	7.31	10.70

ELEMENTI CARATTERISTICI PER IL PERIODO 1965

Max	kg/m^3	24.300	24.300	6.700	2.340	0.057	0.196	0.058	0.000	0.000	4.060	0.107	0.125	15.700
	kg/s	4610.00	4610.00	251.00	34.20	0.08	0.06	0.01	0.00	0.00	8.44	0.07	0.07	18.20
Min.	kg/m^3	0.000	0.076	0.019	0.035	0.001	0.014	0.000	0.000	0.000	0.000	0.020	0.011	0.007
	kg/s	0.00	0.22	0.15	0.05	0.00	0.00	0.00	0.00	0.00	0.00	0.01	0.01	0.00
Med.	kg/m^3	7.210	11.700	2.340	0.575	0.029	0.027	0.000	0.000	0.000	0.712	0.049	0.044	0.579
	kg/s	28.20	303.00	27.20	2.41	0.03	0.01	0.00	0.00	0.00	0.37	0.02	0.03	1.32
10^3 *tonn*		889.00	812.00	65.70	6.45	0.08	0.04	0.00	0.00	0.00	0.96	0.05	0.08	3.54
tonn/km²		1710.00	1560.00	126.00	12.40	0.15	0.08	0.00	0.00	0.00	1.84	0.10	0.15	6.79

Figure 3.1.2 – Example of the annual hydrometric report from the Hydrological Annals.

Data collection started in 1957 and concluded in 1990 in Sicily. Nineteen rivers were monitored at different times and with discontinuity. The list of the rivers is reported in Table 3.1.1, whereas the location of the suspended sediment gauges is indicated in the map of Figure 3.1.3.

Suspended sediment data from seven selected major rivers were chosen for this study. Despite providing the longest information on sediment yield, there are still some gaps in the dataset. The rivers selected for the study have different catchment areas, and they also exhibit different land use and geomorphological characteristics.

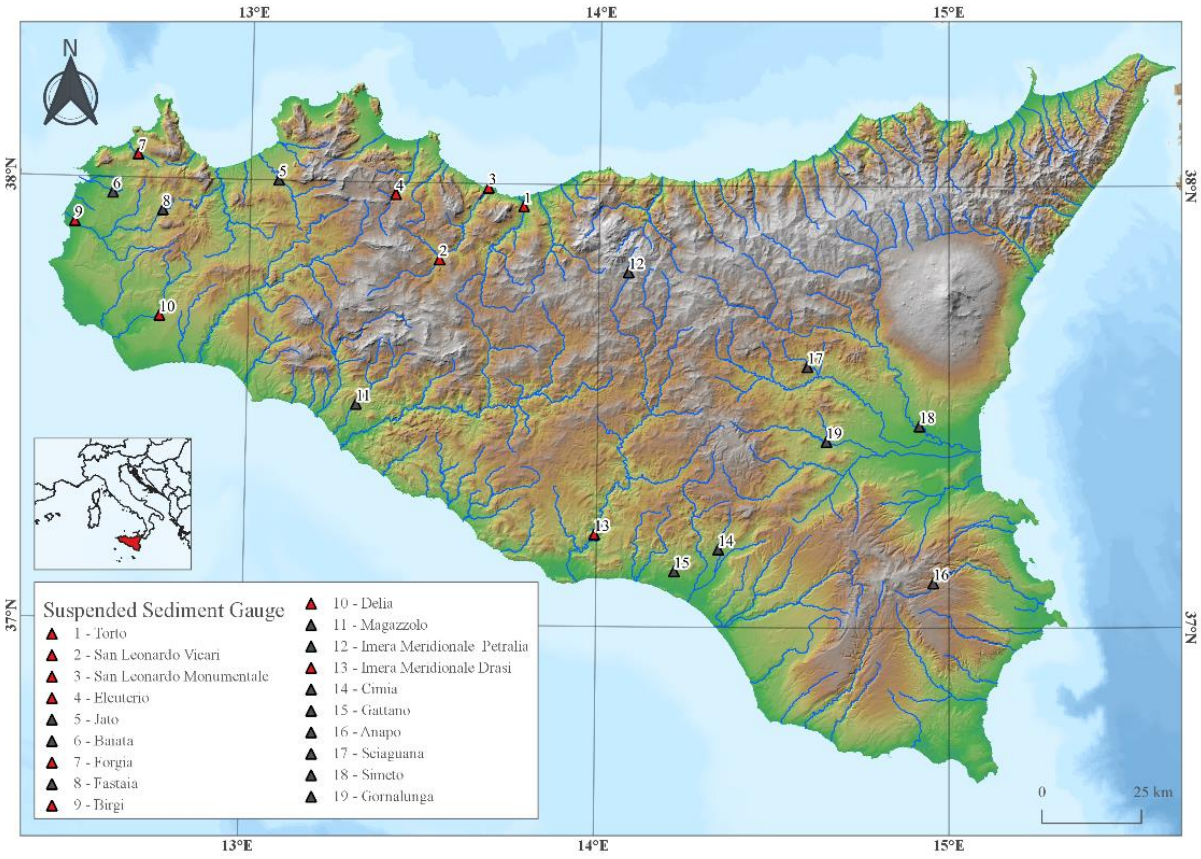

Figure 3.1.3 - Location map of the Suspended Sediment gauges. Triangles in red are the gauges selected in this study.

No	Rivers	Gauges	1957	1958	1959	1960	1961	1962	1963	1964	1965	1966	1967	1968	1969	1970	1971	1972	1973	1974	1975	1976	1977	1978	1979	1980	1981	1982	1983	1984	1985	1986	1987	1988	1989	1990	
1	Torto	Bivio Cerda															■	■	■	■	■	■	■			■			■								*
2	San Leonardo	Vicari																■	■	■	■	■	■	■	■	■	■	■			■	■	■				*
3	San Leonardo	Monumentale									■	■	■	■	■	■	■	■	■	■	■	■	■	■	■	■											*
4	Eleuterio	Risalaimi					■	■	■	■	■	■			■	■	■	■	■	■	■	■	■	■	■	■					■	■	■	■	■	■	*
5	Jato	Taurro						■	■	■	■	■	■																								
6	Baiata	Sapone													■	■	■			■	■	■	■	■													
7	Forgia	Lentina															■	■	■	■	■	■	■	■	■	■	■	■	■				■	■			*
8	Fastaia	La Chinea						■	■	■	■		■	■	■	■	■	■	■	■	■	■	■	■													
9	Birgi	Chinisia															■	■	■	■	■			■	■	■	■	■	■	■			■				*
10	Delia	Pozzillo						■	■	■	■	■	■	■	■		■	■	■	■	■	■	■	■													*
11	Magazzolo	Corvo																■	■	■	■			■	■												
12	Imera M.	Petralia															■	■		■	■	■	■	■	■	■	■	■		■							
13	Imera M.	Drasi								■	■	■	■	■	■	■	■	■	■	■	■	■	■	■	■	■	■	■	■	■	■	■	■	■	■	■	*
14	Cimia	Cerasaro												■	■	■																					
15	Gattano	Zai																		■	■	■															
16	Anapo	San Nicola																■	■	■	■	■	■	■	■	■	■	■			■	■	■		■	■	
17	Sciaguana	Torricchia													■	■	■	■		■	■	■	■	■													
18	Simeto	Giarretta	■	■	■	■	■	■	■	■	■	■	■																								
19	Gornalunga	Secreto						■	■	■	■	■																									

Table 3.1.1 – List of rivers and gauges taken into consideration.

In the following, the time-series plots for average monthly discharge values (m^3/s), monthly sediment yield (10^3 tons), monthly sediment concentrations (kg/m^3), and the location of the measurement sections are reported.

Torto basin

The Torto Basin (Fig. 3.1.4) is located in the northern sector of Sicily and drains into the Tyrrhenian Sea. The gauge station, named "Bivio Cerda", is situated 3 km from the mouth and encompasses a contributing area of 414 km^2. The station has been operational from 1971 to 1984, during which time the maximum monthly average value of discharge of 19 m^3/s was recorded in December 1976, coinciding with the peak of sediment yield value of 2440 x10^3 tons. The highest sediment concentration was recorded in September 1971, marking a significant event in the basin's history.

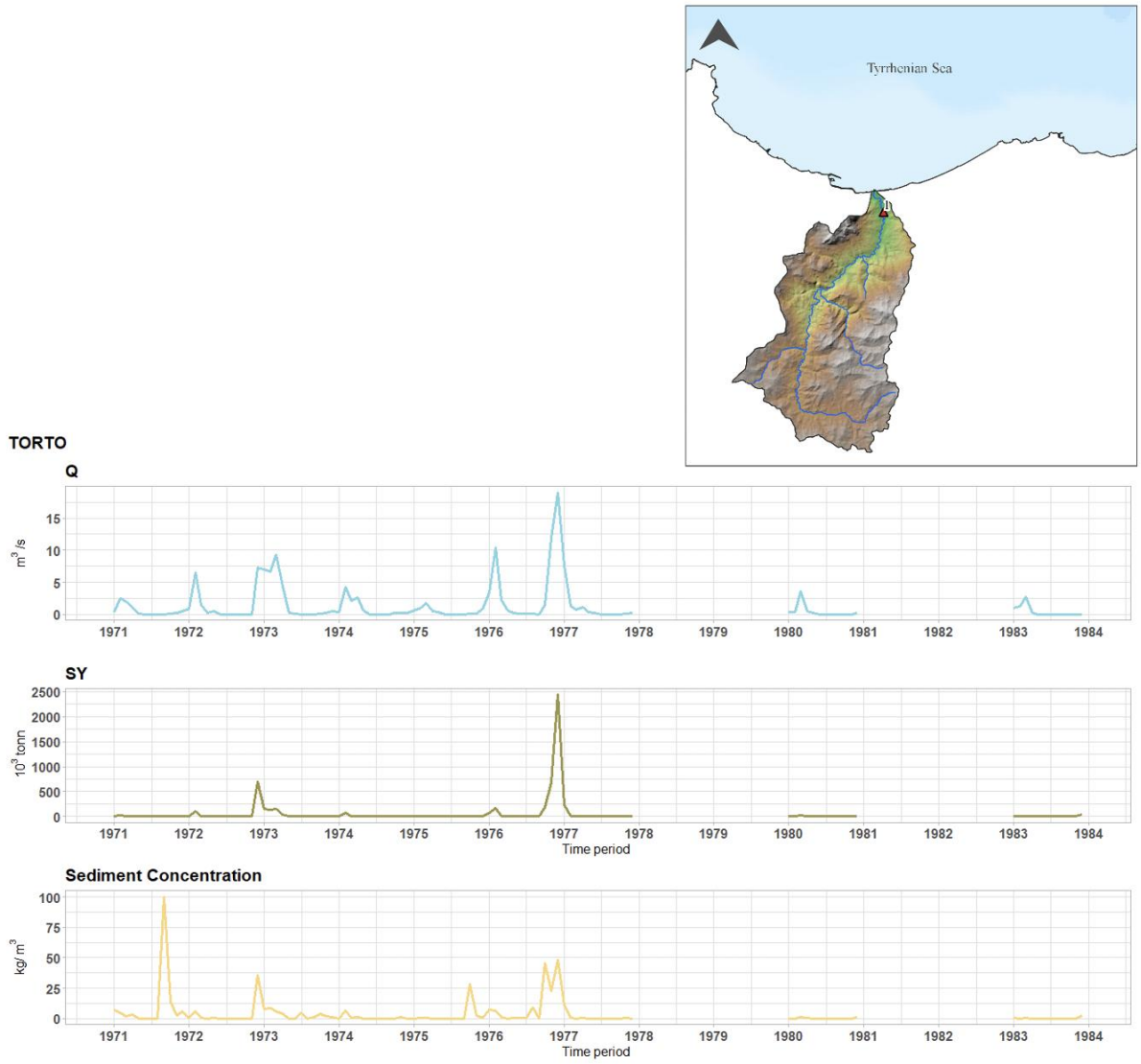

Figure 3.1.4 – Location of the "Bivio Cerda" section in the Torto River basin and the time series plots for discharge (Q), Sediment Yield (SY), and Suspended Sediment Concentration (SSC).

San Leonardo basin

The San Leonardo Basin is situated west of the Torto Basin, and it is equipped with two gauges. The Vicari gauge (Fig. 3.1.5) is located south, with a contributing area of 253 km^2 and a distance of 30 km from the mouth. The Monumentale gauge (Fig. 3.1.6) is positioned north, with a contributing area of 521 km^2 and a distance of only 0.9 km from the mouth. The Vicari gauge has been operational from 1972 to 1987. The maximum monthly average discharge value was recorded in December 1976 (13.6 m^3/s). The peak sediment yield was observed in April 1973 with a value of 56 x10^3 tons. The Monumentale gauge was operational from 1968 to 1980, and the maximum values for the three parameters were all recorded in the year 1976.

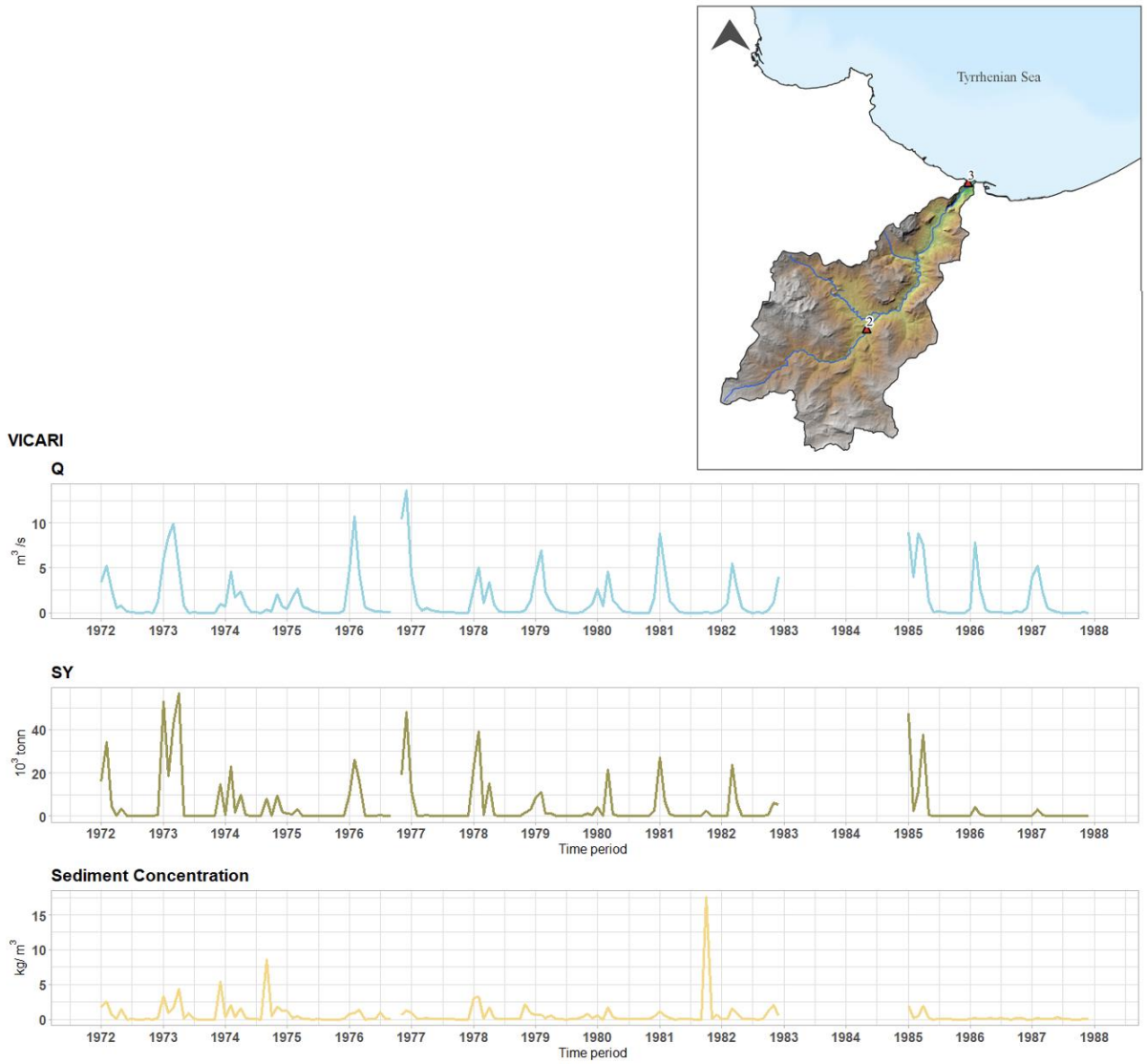

Figure 3.1.5 – Location of the "Vicari" section in the San Leonardo River basin and the time series plots of discharge (Q), Sediment Yield (SY), and Suspended Sediment Concentration (SSC).

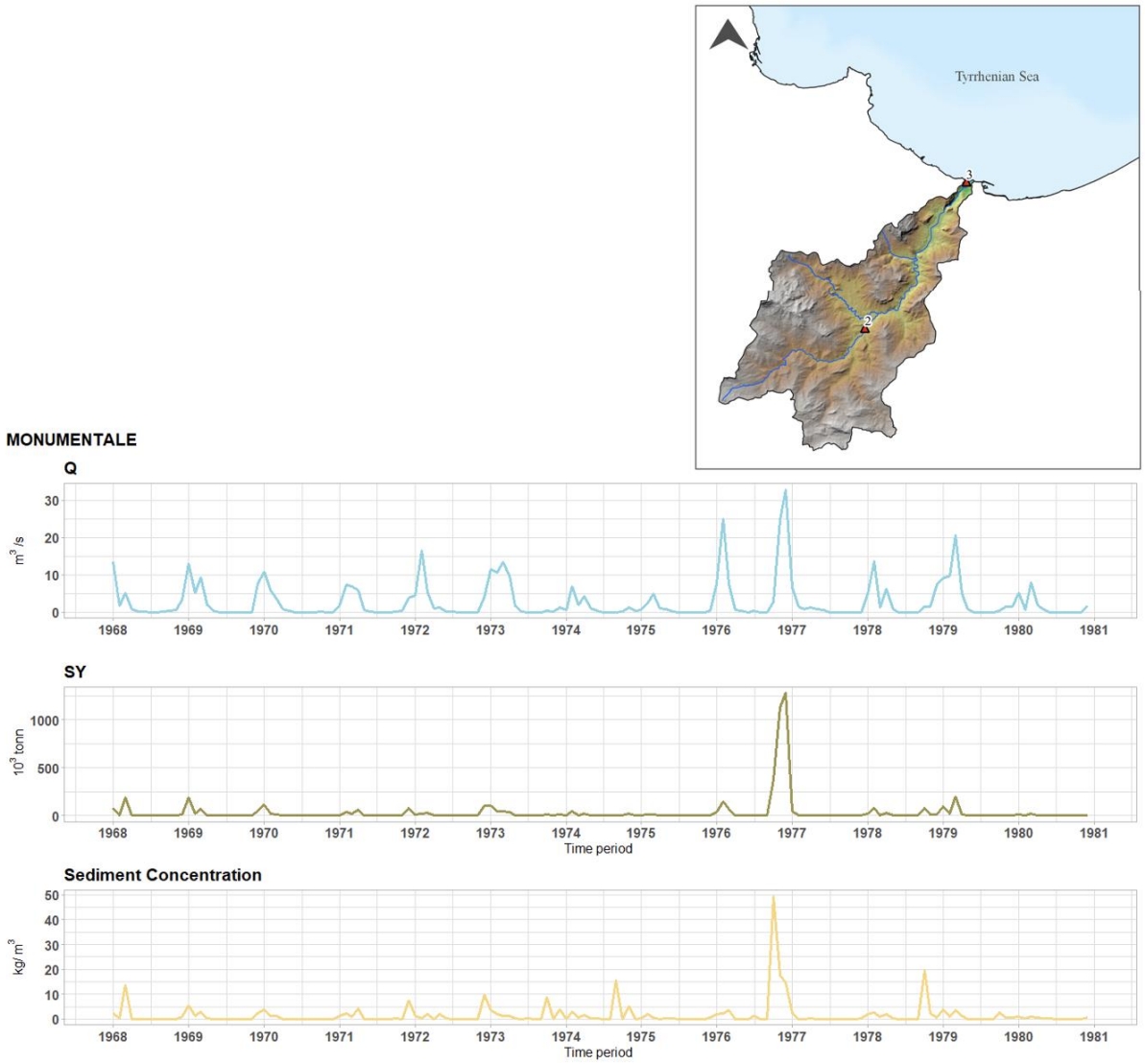

Figure 3.1.6 – Location of the "Monumentale" section in the San Leonardo River basin and the time series plots of discharge (Q), Sediment Yield (SY), and Suspended Sediment Concentration (SSC).

Eleuterio basin

The Eleuterio Basin (Fig. 3.1.7) is located westward to the San Leonardo River basin. From 1961 to 1990, a liquid and solid flow measurement station has been installed in the basin, situated 18 km from the mouth and encompassing a contributing area of 52.9 km^2. During the operational period, the maximum monthly discharge value was recorded in February 1963. The highest sediment yield value was documented in February 1970, with a value of 10.2 $x10^3$ tons, while the maximum sediment concentration was recorded in 1962, with a value of 9.140 kg/m^3.

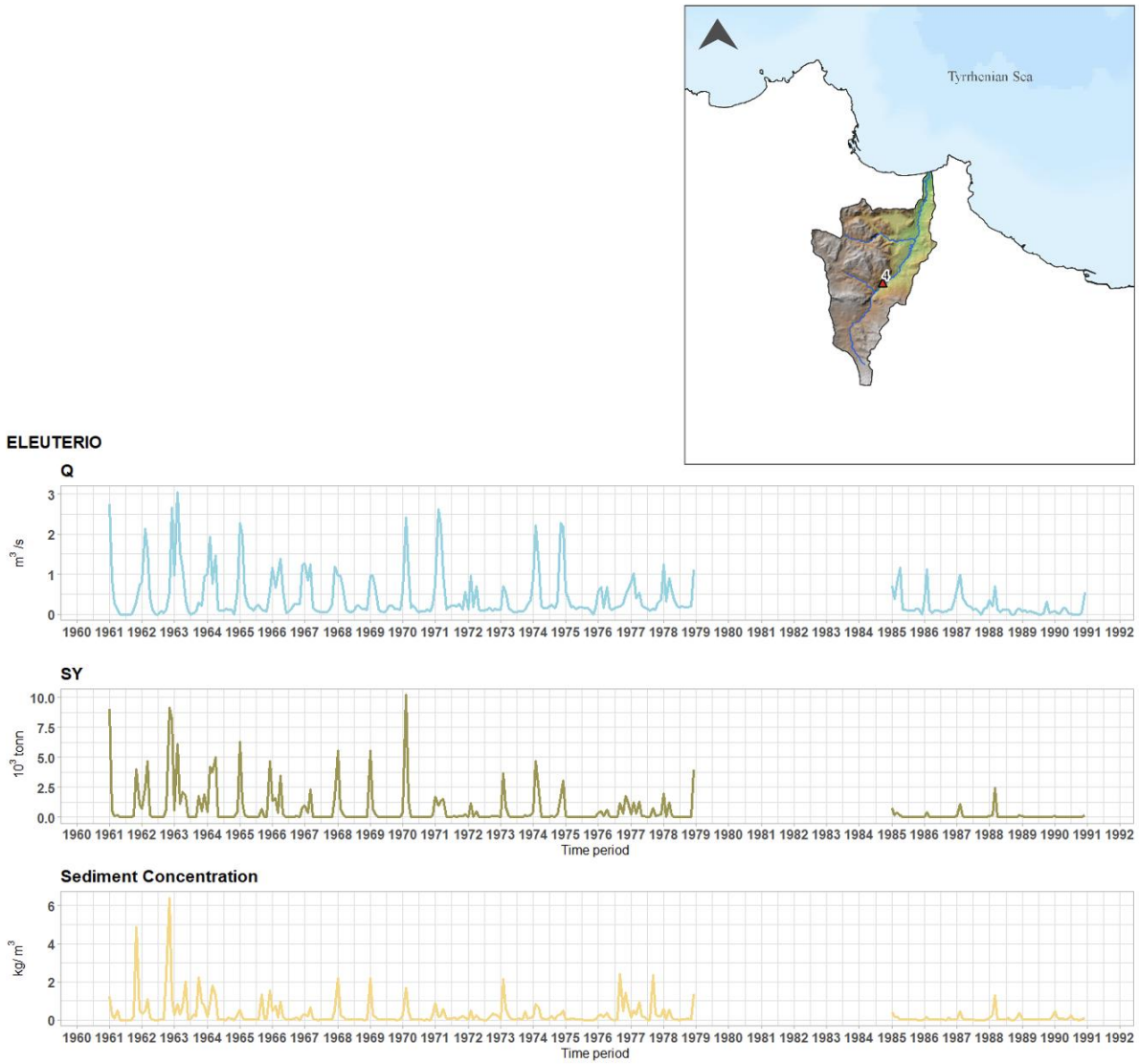

Figure 3.1.7 – Location of the "Risalaimi" section in the Eleuterio River basin and the time series plots of discharge (Q), Sediment Yield (SY), and Suspended Sediment Concentration (SSC).

Forgia basin

The Forgia River Basin (Fig. 3.1.8) is situated in the northwestern sector of Sicily. The upstream contributing area of the station, called "Lentina", covers 45.7 km^2 and the latter is located 5 km from the mouth. During its operations from 1971 to 1988, the station achieved the highest monthly average discharge of 2.6 m^3/s in February 1976. The maximum sediment yield and sediment concentration values were recorded in January 1977, with values of 4.52 x10^3 tons and 3.9 kg/m^3, respectively.

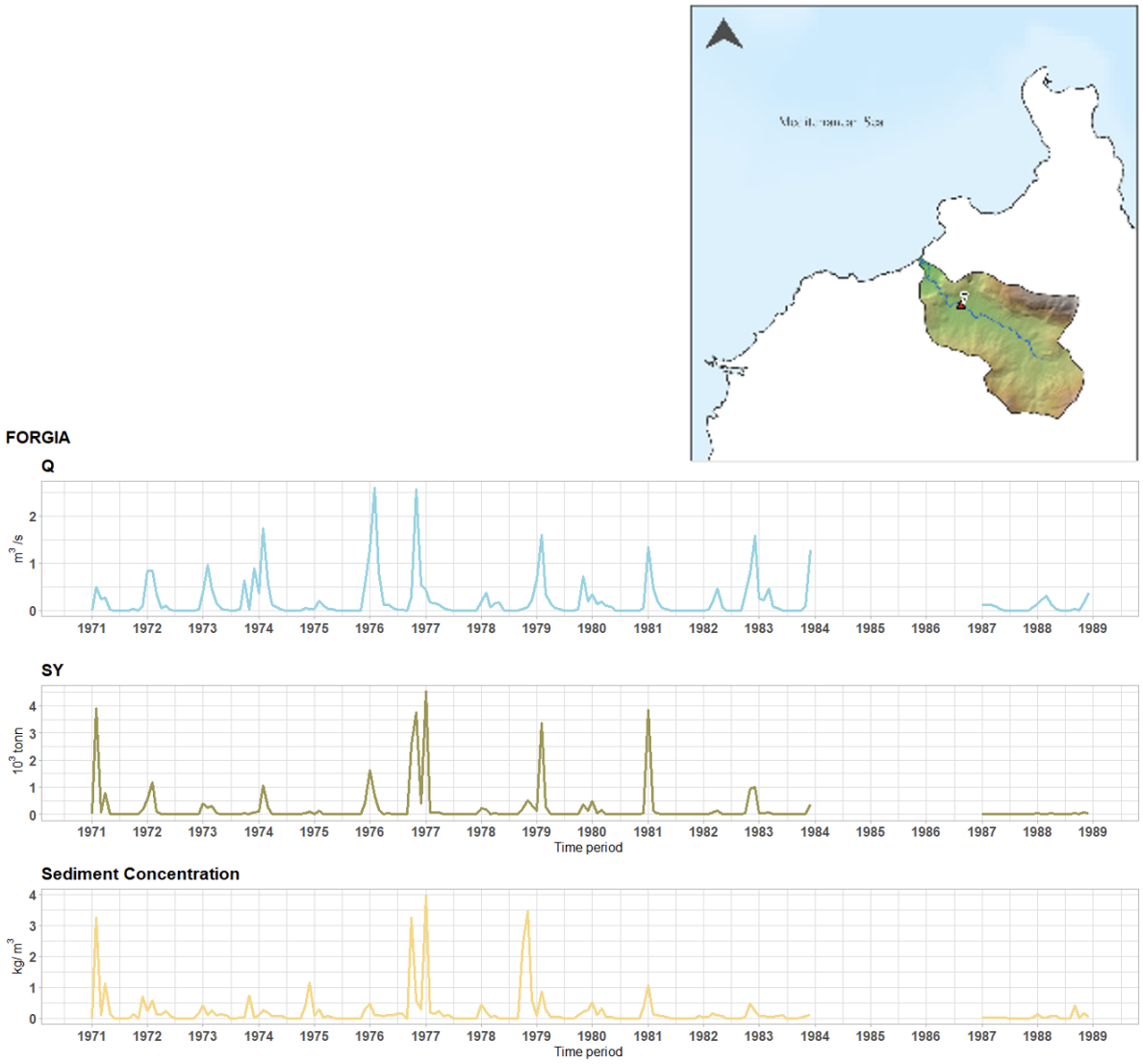

Figure 3.1.8 – Location of the "Lentina" section in the Forgia River basin and the time series plots of discharge (Q), Sediment Yield (SY), and Suspended Sediment Concentration (SSC).

Birgi basin

The Birgi River's Basin is situated in the westernmost region of Sicily (Fig. 3.1.9). The hydrometric station, named "Chinisia", is located 3.5 kilometres from the river's mouth, and the area upstream of the gauge station covers approximately 300 km^2. The average altitude of the basin is 194 meters above sea level. The station was operational from 1971 to 1987 and recorded an average maximum liquid flow value (10.3 m^3/s) in December 1983. The highest sediment yield value was documented in October 1971 with a value of 269 $x10^3$ tons.

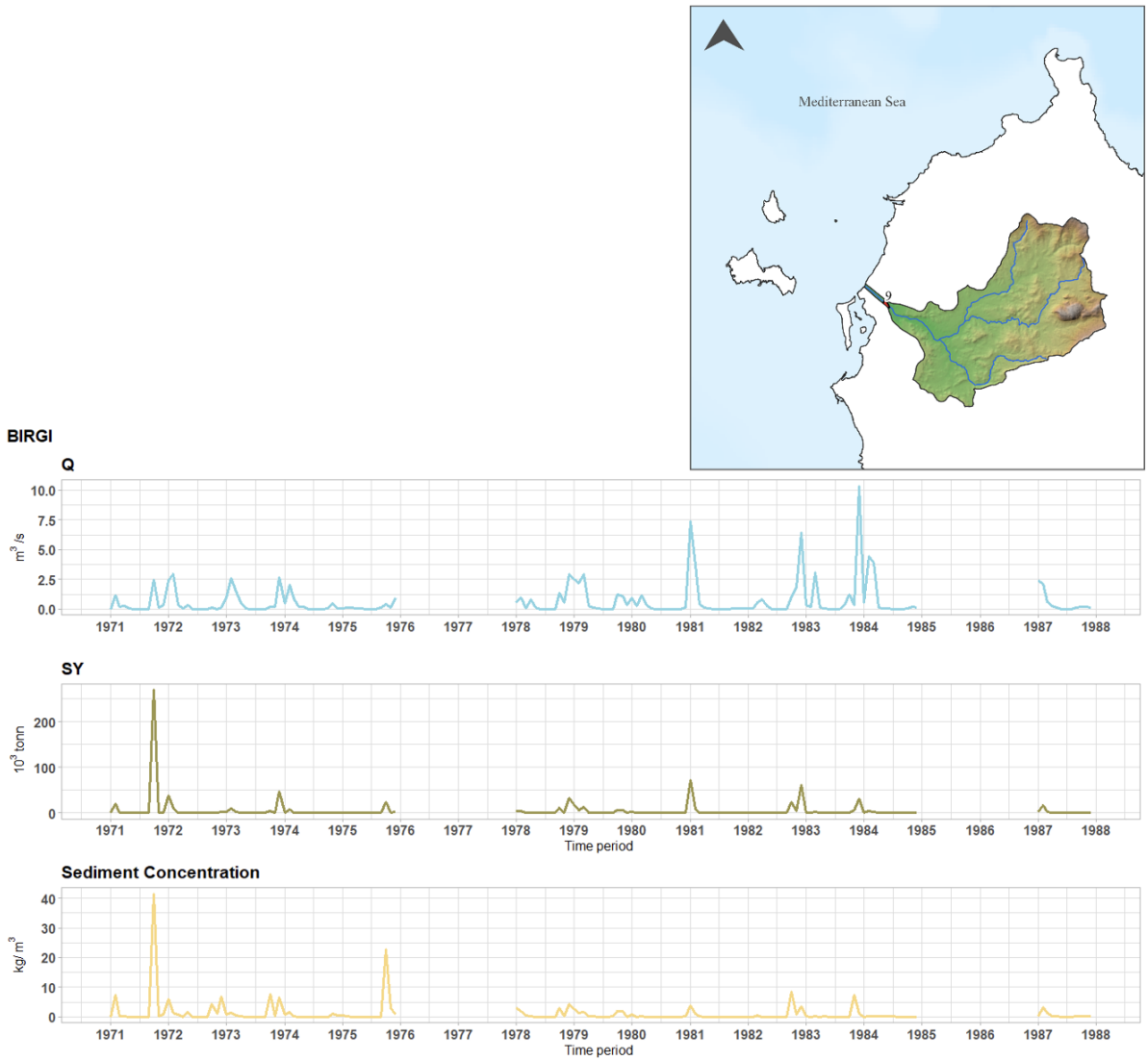

Figure 3.1.9 – Location of the "Chinisia" section in the Birgi River basin and the time series plots of discharge (Q), Sediment Yield (SY), and Suspended Sediment Concentration (SSC).

Delia basin

The hydrological basin of the Delia River was located south of the Birgi basin, and it drains into the Sicily Channel. The hydrometric section is situated 34 km from the mouth and encompassed an area of approximately 139 km^2. The gauge was active from 1962 to 1978, recording the highest monthly average maximum flow in November 1976, when the highest sediment yield value was also recorded (190 x10^3 tons).

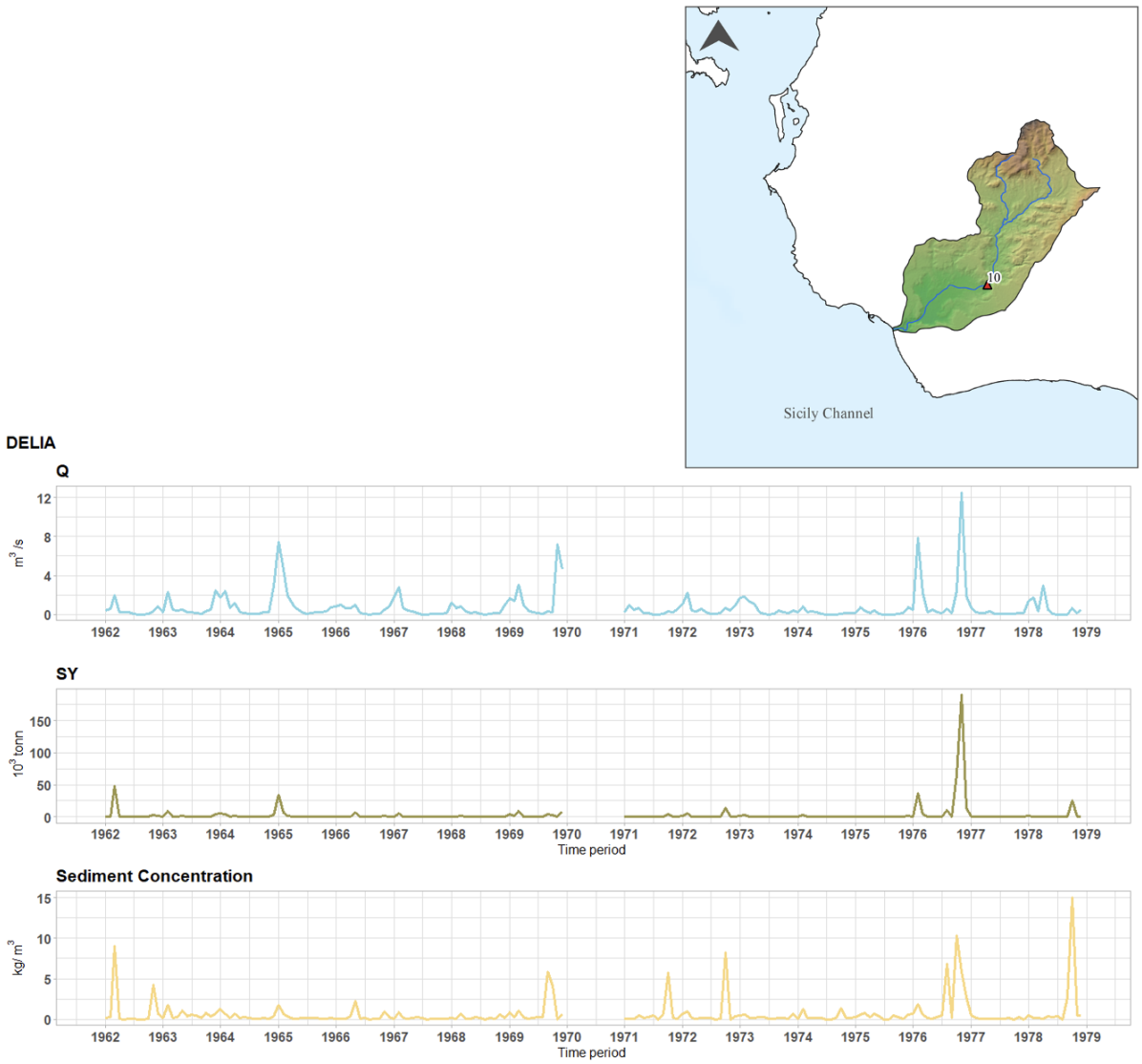

Figure. 3.1.10 – Location of the "Pozzillo" section in the Delia River basin and the time series plots of discharge (Q), Sediment Yield (SY), and Suspended Sediment Concentration (SSC).

Imera Meridionale basin

The Basin of the River Imera Meridionale or Salso (Fig. 3.1.11) is the second channel of Sicily both for the width of the basin and the length of the main channel. It is located in the central portion of the southern side of the island and has an elongated shape in the N-S sense draining into Sicily's Channel. The discharge measuring station operating from 1964 to 1990 is located 34 km from the mouth and had a contribution area of about 1782 km^2. The average maximum flow rate was recorded in January 1985, the highest sediment yield value was recorded in January 1973.

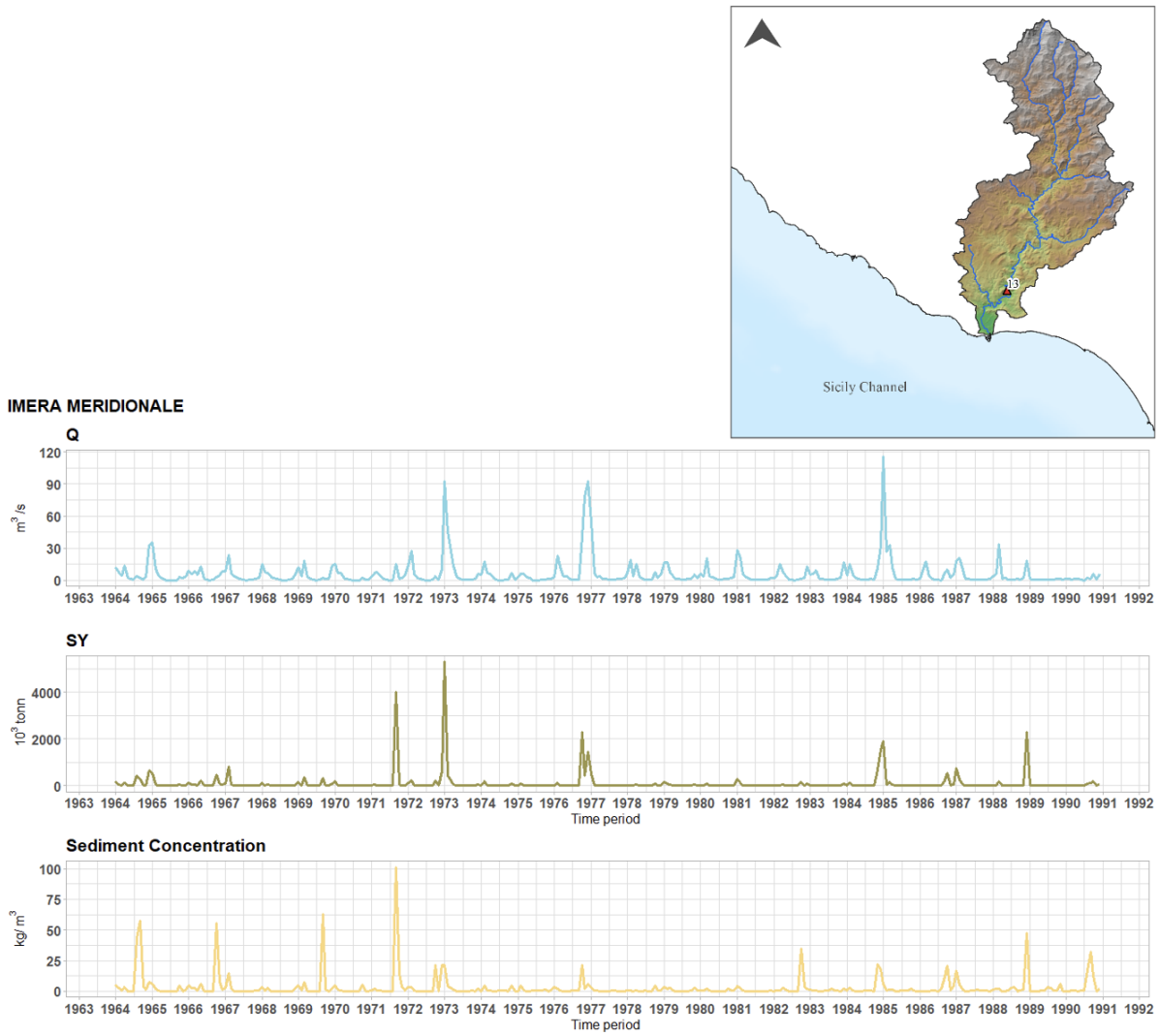

Fig. 3.1.11 – Location of the "Drasi" section in the Imera Settentrionale River basin and the time series plots of discharge (Q), Sediment Yield (SY), and Suspended Sediment Concentration (SSC).

3.1.2 Analysis of Sediment Yield Data

Over the last two decades, there has been an increased interest in investigating the relation between catchment area and sediment yield at a given gauge station. Many studies reported a decreasing area-specific sediment yield (SSY; tonn/km^2 yr) with increasing catchment area (A; km^2). This trend can be explained by the theory of sediment sources and sinks (Walling, 1983). With increasing catchment area, the transported sediment moves into areas with reduced slope gradients and well-developed flood plains. Thus, the probability that sediment particles eroded from the upstream catchment will be deposited increases with increasing transport distance and thus catchment area. The relation between A and SSY is:

$$SSY = \alpha A^{\beta}$$

where A stands for catchment area, α and β are empirical parameters.

However, the relation between basin area and area-specific sediment yield is not so uniquely set. As proposed by Dedkov and Moszherin, (1992) this relationship appears to depend on the dominant erosion processes in the catchment. In general, a positive trend is observed in areas where channel erosion dominates, while a negative trend is noted in areas where slope erosion is the primary sediment source. Similarly, according to Slaymaker et al. (2003), a positive relation between A and SSY indicates sediment capturing along a channel and channel degradation, possibly accompanied by significant sediment delivery to the main rivers due to landslides. Furthermore, the spatial patterns of lithology, topography, climate, and land use within the drainage basin control the spatial distribution of sources and sinks of sediment, influencing the trend between A and SSY. In basins strongly impacted by agricultural use, hillslope erosion is often dominant over river channel erosion processes. Conversely, in basins with limited human impact and well-developed vegetation cover, hillslope erosion has a negligible contribution to sediment yield. In such basins, sediment yield is primarily controlled by permanent gully and river channel erosion processes and can be increased by landslides. This results in a continuous increase in SSY with increasing A.

In conclusion, in regions characterized by significant variability in climate, topography, land use, and soil, the spatial heterogeneity of sediment sources can lead SSY to be independent of A. Therefore, a unique relation between SSY and the catchment area may not be observed.

Interestingly, the Sicilian drainage basins, here considered, exhibit a slightly positive correlation between catchment area and SSY. The positive relationship depicted (Fig. 3.1.12) suggests that, for some of these Sicilian catchments, upland erosion may not be the predominant contributor to specific sediment yield. In particular, in light of the dominant denudation processes that shape the selected Sicilian basin at various degrees, a marked role played by near-channel phenomena arises, which can be ascribed to the erosion of fluvial banks and/or landslide feet or toes.

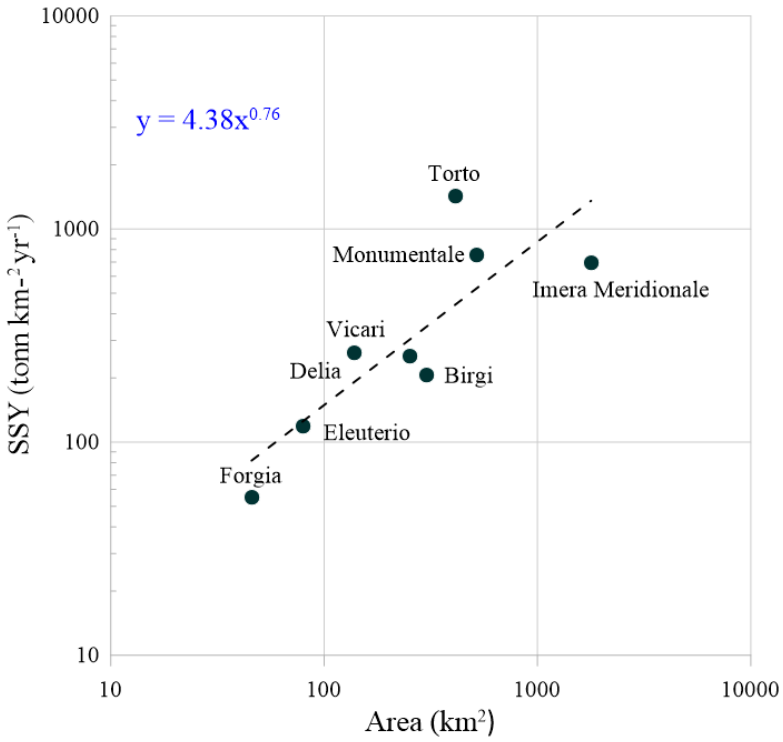

Fig. 3.1.12 – Specific Sediment Yield versus catchment Area and for the gauge station analyzed in this study.

Based on the outcomes derived from applying the WaTEM/SEDEM (see Chapter 2.4) model in Sicily (Borrelli et al., 2018), a comparison was made between the estimated gross erosion (rill, inter-rill, gully) on the contributing hillslopes and the measured soil delivery at the gauge station. In particular, WaTEM/SEDEM gives an estimate of the sediment feeding the pixels along the drainage network but does not route the delivered sediment along the channel. In this way, the Channel Soil Delivery Ratios for the analyzed basins can be estimated (Fig. 3.1.13). In particular, using the soil loss mass estimated from WaTEM/SEDEM and the Specific Sediment Yield measured at the watershed outlets, it was possible to compute the SDR according to:

$$SDR = \frac{SSY(gauge\ station)}{Soil\ loss\ (WaTEM-SEDEM)}.$$

The resulting SDR represents the proportion between the mass of the eroded sediment delivered from the hillslope to the drainage network and the actual mass captured as suspended sediment at the outlet.

The results depict an erosive scenario strongly controlled by near channel processes, with SDRs close to 1 for gauge stations located close to the mouths of their rivers (Birgi-Chinisia, Imera Meridionale-Drasi, Torto-Bivio Cerda) and far from 1 for more inner gauge (far from mouth) stations (San Leonardo-Vicari, Eleuterio-Risalaimi). In light of the extension of the contributing area, the Imera-Drasi station is here assumed to be close to the mouth despite the reported distance. The couple Delia-Pozzillo (far from mouth) and San Leonardo-Monumentale (close to mouth) assume an intermediate behaviour, whilst Forgia-Lentina strongly departs from the expected trend (close to mouth, but very low SDR).

The observed trend seems to suggest that at the full morphodynamic scale of fluvial transportation processes, a recovery of the sediment loss occurs as the more transport-dominated sector is included, whilst at the partial scale of the inner catchments, the discontinuous routing of the delivered sediment leaves a dominant role to near-channel phenomena.

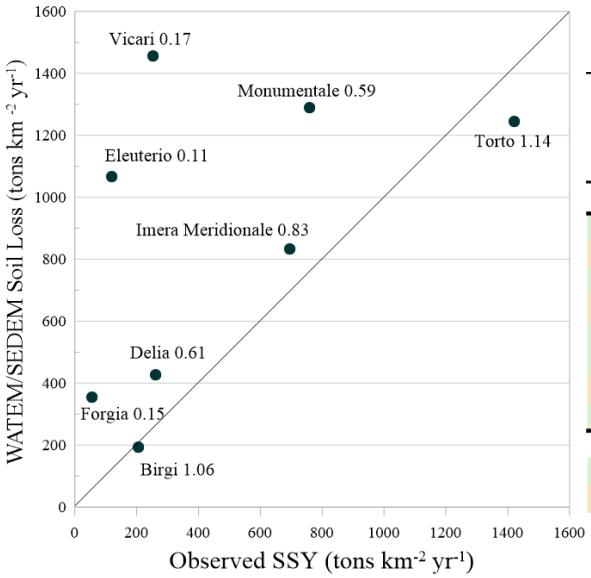

River	Gauge	Area	Average elevation of basin	Distance from the river mouth (km)
		km^2	m a.s.l.	
Torto	Bivio Cerda	414	491	3
San Leonardo	Vicari	253	672	30
San Leonardo	Monumentale	522	578	1
Eleuterio	Risalaimi	80	631	18
Forgia	Lentina	46	285	5
Birgi	Chinisia	293	194	4
Delia	Pozzillo	139	259	34
Imera Meridionale	Drasi	1782	536	34
close to the mouth				
inner (far from the mouth)				

Fig. 3.1.13 -Channel SDR plot for the selected gauge stations.

Analyzing the relationship between channel SDR and area, a positive trend arises, together with the strong anomaly of Imera Meridionale-Drasi, attesting to the recovery of channel sediment routing efficiency for large close-to-mouth gauges.

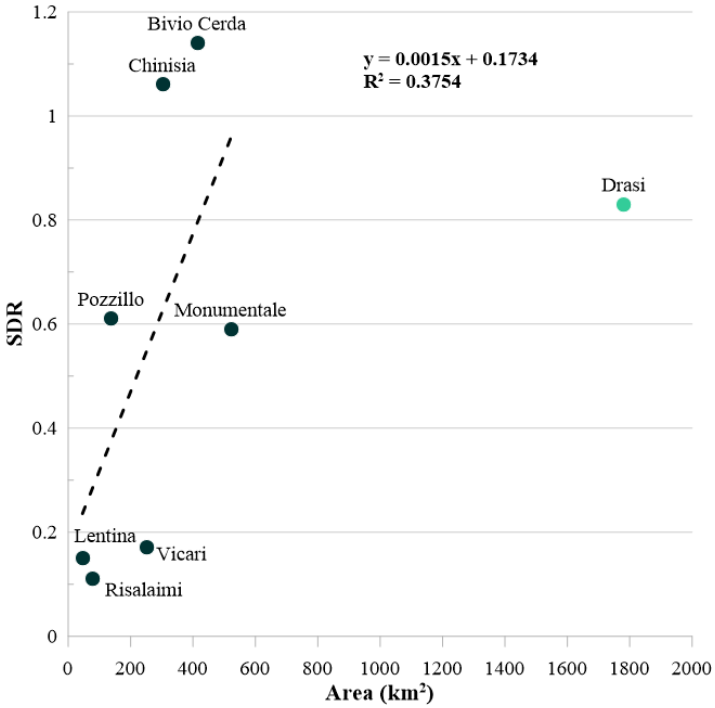

Fig. 3.1.14 -Channel SDR versus area (the fitted trend line disregards the outlier of Imera Meridionale - Drasi).

The suspended sediment data of these selected Sicilian gauges were analysed in terms of coherence with similar general trends which were reported for Italian rivers (Billi and Spalevic, 2022). At first glance (Fig. 3.1.15), the smaller extension of the contributing area to the Sicilian gauges resulted in an opposite trend, which could also be explained by the specific climatic and geologic setting of the contributing watershed. A negative correlation is reported and explained by the theory of sediment sources and sinks, already mentioned above (Walling, 1983), stating that the probability that sediment particles eroded from the upstream catchment will be delivered to the gauge station decreases with long transport distance. At the same time, a positive trend can be observed in areas where channel erosion or foot-slope landslides dominate, with negative trends limited when slope erosion is the primary sediment source (Dedkov and Moszherin, 1992; Slaymaker et al., 2003). However, according to the above-discussed data, the cases of the Sicilian dataset can be explained by considering a dominant role for near-channel erosion processes.

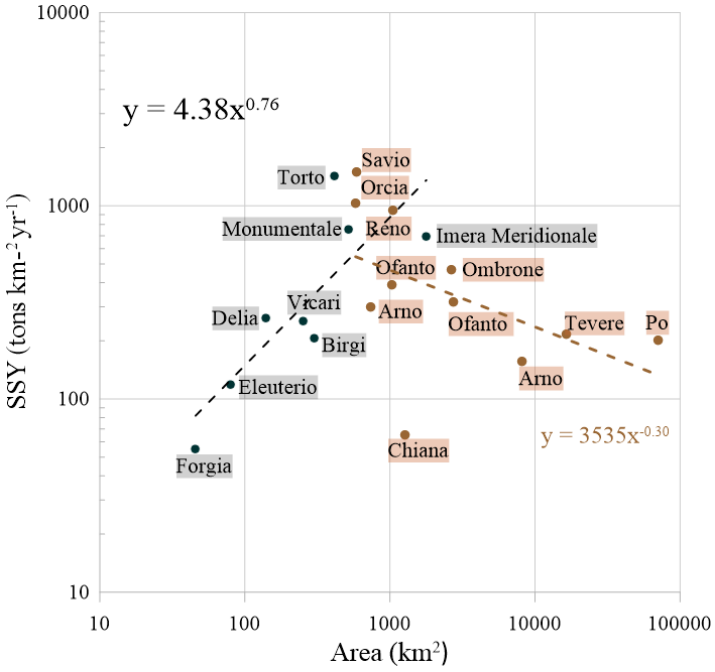

Fig. 3.1.15 -Soil Sediment Yield versus Area: comparison between Italian large rivers and the eight selected Sicilian gauges.

3.1.3 Analysis of Sediment Rating Curves (SRCs)

The sediment rating curves (SRCs) investigate the link between Suspended Sediment Concentration (SSC: kg/m^3) and water discharge (Q: m^3/s) and denote the statistical correlation between suspended sediment concentration or sediment discharge and stream discharge. One widely adopted form for the sediment rating curves takes the shape of a power function:

$$C = aQ^b,$$

where *a* and *b* are the regression coefficient and exponent, respectively.

Exploring the SRCs actually furnishes potential keys for interpreting the erosion dynamics in a region. In fact, assuming both surface runoff and soil erosion are strongly dependent on rainfall and temperature regimes, the way these climatic stressors act can be very complicated, depending on the superimposition of their spectra. The way rainfall acts, tuning both water erosion, landslides, and surface runoff, depends on its intensity, duration, recurrence, and cumulated effects. At the same time, the temperature regime controls both the soil water balance, actually tuning the runoff coefficients, and relevant connected soil erosion processes such as those based on hydroclastic expansion/contraction cycles on clayey soils.

A SRC-fitted function can be considered as a black-box model (Iadanza and Napolitano, 2006) in which the coefficients, calculated through regression analysis, actually seem to lose a physical significance. Nevertheless, some physical interpretations can be posed. In particular, the rating coefficient "a" represents the sediment concentration at unit discharge and depends on the availability of sediment in the contributing area, on the erodibility of the outcropping soils, and on the connectivity of the stream flow network. Morgan (2006) states that the "a" coefficient represents an index of the erosion severity, with high values indicating a large availability of weathered sediment in the basin, which can be easily eroded and transported by runoff. At the same time, the rating exponent "b" indicates the changing rate of the suspended sediment load per change of unit water discharge, configuring three cases (straight, concave, or convex shape, respectively): $b = 1$, the suspended sediment load increases in a linear fashion with the increase of stream discharge; $0<b<1$, the suspended load increases at a diminishing rate with the increase of discharge, in this case the rating curve has a concave shape, indicating a supply limited behaviour of the rivers, indicating the amount of sediment available control the amount of sediment transported; $b>1$, the suspended load increases at an increasing rate with the increase of discharge, in this case, the shape of the rating curve is convex meaning a transport limited behaviour of the rivers, when the discharge does not match the threshold for eroding all available eroded sediment. This condition is typical when coarse material is present in the river bed or when the stream discharge does not reach the specific threshold value for sediment transportation.

The b coefficient represents the power of the river to erode and transport sediments. The b coefficient can also be affected by the grain size, with higher b values resulting in coarser sediments. In a certain sense, the steepness of the SRC reflects the so-called "reactivity" of the river system to changings in Q, with high "b" values attesting a large sediment availability in a transport limited system or in the transition from normal to flashier regime. The regional distribution of the "b" exponent is controlled by the climatic characteristics as well as the catchment characteristics (i.e., steepness, basin size, channel length).

Finally, it is worth recalling that the two ("a" and "b") coefficients are inversely correlated. Some authors (Warrick, 2015) studied changes in sediment rating curve parameters over time to detect alteration of the erodibility and or supply of sediment in the watershed, as well as of the power of the river to erode and transport sediment.

Not only the hydraulic properties of the flow, but also the sediment supply from the catchment, the rainfall intensity and its spatial distribution, the runoff amount and rate, and the travel rates and distance of floodwaters in the main channel determine the suspended sediment response. Consequently, suspended sediment concentrations show a high degree of scatter, and sediment-rating curves can substantially underestimate the concentrations. Various methods, such as seasonally subdividing the suspended sediment dataset as a function of the hydrological flow conditions or choosing a threshold discharge, have been developed to improve the fitting.

Starting from the available time series, which are stored as monthly average values, in a first processing stage, the SSC mean values were computed for each decile class of Q. All the zero values were excluded in the analysis. This approach is actually quite different from the typically adopted, which is rather focused on real time short duration analysis. However, as the main task of the research was to investigate the general behaviour of erosion processes in Sicily, this geomorphological perspective was adopted. Besides, the analysis was carried out both on an annual picture and splitting the data according to the expected climatic regime of rainfall and temperature, which in Sicily is marked by winter (from December to June) and autumn (from July to November) seasons.

The SRC analysis allowed us to capture the specific behaviour of the erosion processes in Sicily (Fig. 3.1.16), with a clear seasonal tuning of the trends, so that higher fitting (Fig. 3.1.17) can be achieved by splitting the data into autumn and winter seasonal subsets. In particular, the splitting of the data resulted in: a general (both winter and autumn sub-series fit better) increasing of the quality of the fitting for Torto - Bivio Cerda, San Leonardo - Monumentale and Eleuterio - Risalaimi; an uncoupled increasing of R^2, (one of the two sub-series performs better than ALL) for San Leonardo - Vicari, Imera Meridionale - Drasi and Forgia – Lentina (in this case, with a dramatic fall of the performance for the autumn sub-series). In the case of Birgi – Chinisia, no non-zero cases were found in the autumn season.

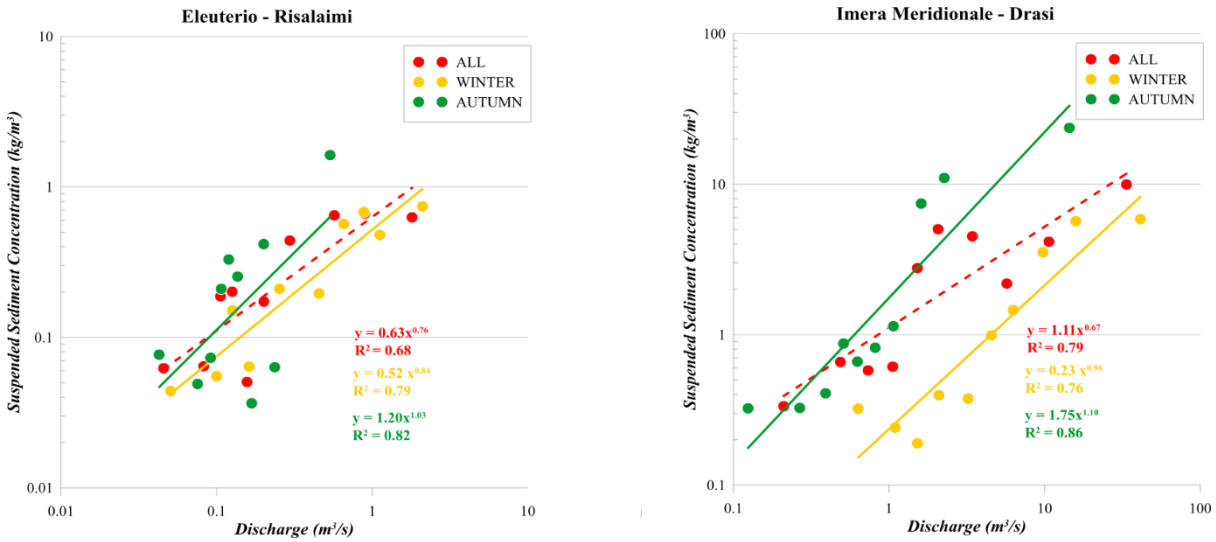

Fig. 3.1.16 a) -Sediment Rating Curves for the eight selected Sicilian gauges.

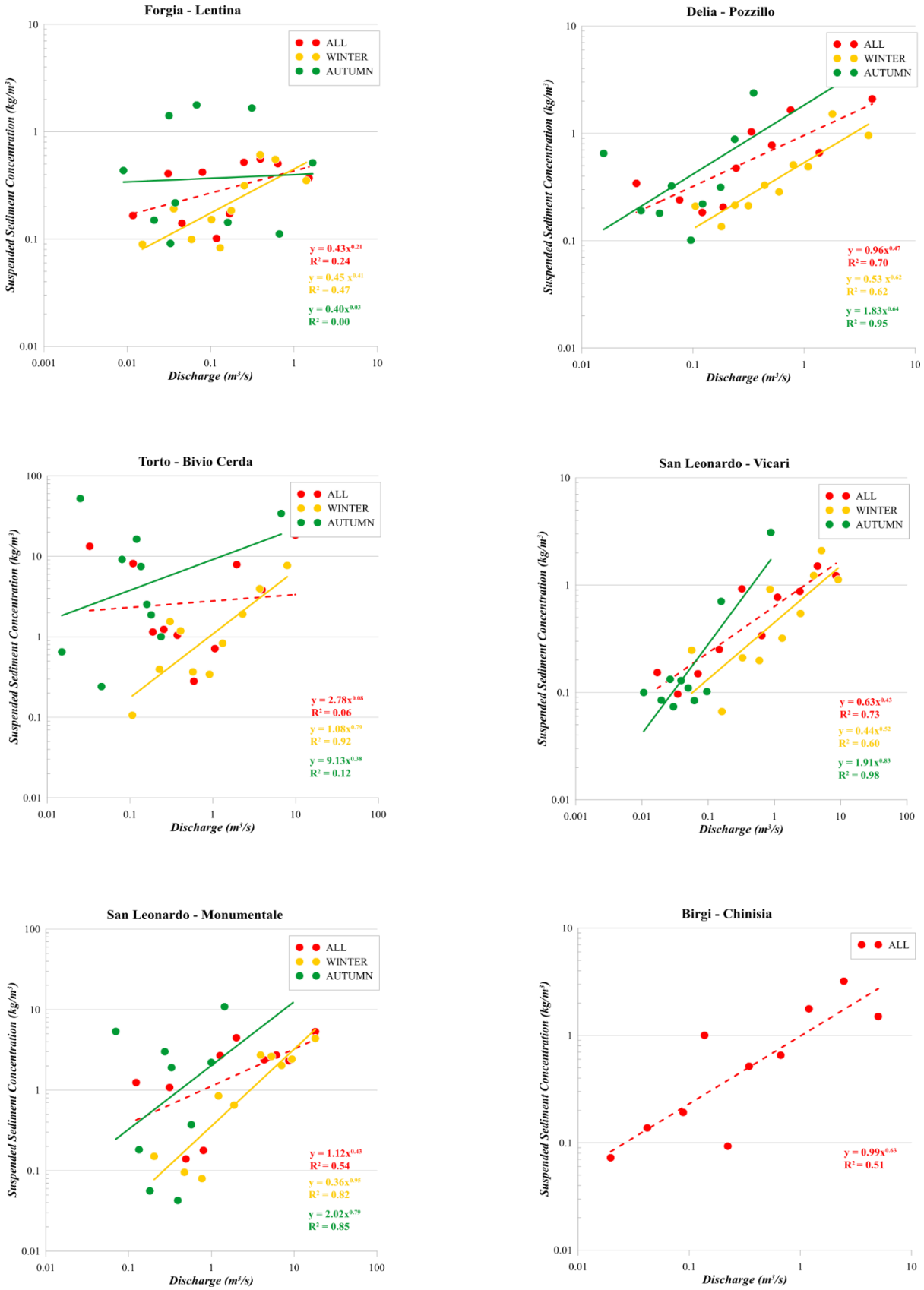

Fig. 3.1.16 b) -Sediment Rating Curves for the eight selected Sicilian gauges.

River	Gauge	ALL			AUTUMN (JUL-NOV)			WINTER (DEC-JUN)		
		a	*b*	R^2	*a*	*b*	R^2	*a*	*b*	R^2
Torto	Bivio Cerda	2.78	0.08	0.06	9.13	0.38	0.12	1.08	0.79	0.92
San Leonardo	Vicari	0.63	0.43	0.73	1.91	0.83	0.98	0.44	0.52	0.60
San Leonardo	Monumentale	1.12	0.43	0.54	2.02	0.79	0.85	0.36	0.95	0.82
Eleuterio	Risalaimi	0.63	0.76	0.68	1.20	1.03	0.82	0.52	0.84	0.79
Forgia	Lentina	0.43	0.21	0.24	0.40	0.03	0.00	0.45	0.41	0.47
Birgi	Chinisia	0.99	0.63	0.51				0.99	0.63	0.51
Delia	Pozzillo	0.96	0.47	0.70	1.83	0.64	0.95	0.53	0.62	0.62
Imera Meridionale	Drasi	1.11	0.67	0.79	1.75	1.10	0.86	0.23	0.96	0.76

close to the mouth

inner (far from mouth)

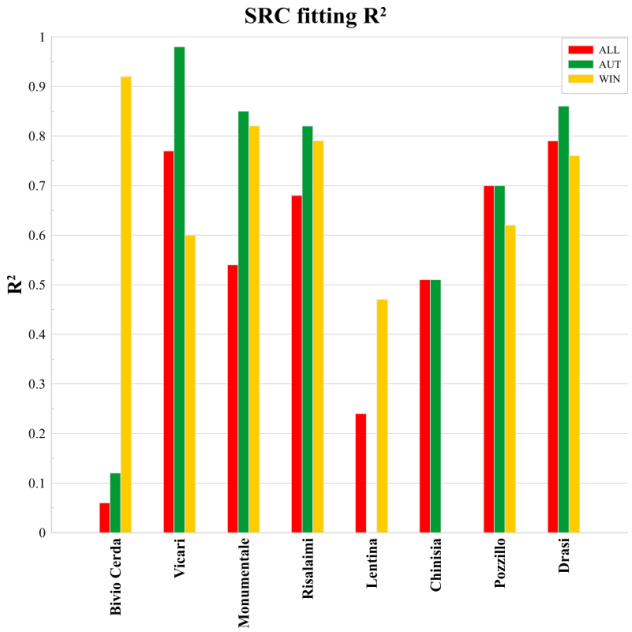

Fig. 3.1.17 -Comparison of the fitting quality between year and seasonally split data.

In general, the winter series are characterized by lower "a" values, suggesting a lower sediment availability with a supply limited condition, whilst autumn series mark a transport limited stage, as expected (Fig. 3.1.18). At the same time, an increase of "b" from winter to autumn is observed for the two markedly inner gauge stations (Eleuterio – Risalaimi and San Leonardo – Vicari), whilst the reactivity of the winter is higher for the close-to-mouth gauge stations. The Forgia – Lentina data clearly show odd results associated with low R^2.

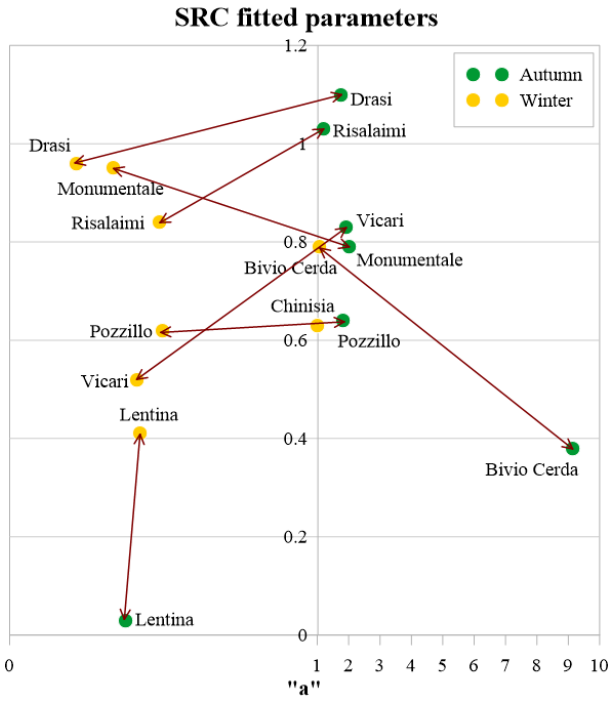

Fig. 3.1.18 – “a” Vs. “b” shift plot.

By computing the distance between autumn and winter “a” Vs. “b” plots it was possible to select those gauge stations which vary in a larger extent their behaviour depending on the season (Fig. 3.1.18). From the obtained values a very marked change of water erosion dynamic arises for the Torto – Bivio Cerda catchment, with a dominant general shift direction toward higher values of “a” from winter to autumn, associated to concomitant “b” increase for Drasi, Risalaimi and Vicari, and “b” decrease, for Monumentale, Bivio Cerda and Pozzilo. The Lentina gauge station confirms its odd behaviour, with a coupled “a” and “b” decrease.

3.1.4 Analysis of sediment/discharge hysteresis

One of the specific aspects of the erosion process is the strong connection between the antecedent conditions on the observed data at a given day or month. In this sense, considering the hysteresis component on the SRCs is very important to recall the role of sediment routing cycles and actual sediment delivery ratios more deeply. Besides, by coupling the sediment yield hysteresis with the seasonal pattern of the climatic forcing, furnishes a complete picture suitable for assessing a reference geomorphological model of the sediment erosion morphodynamic. Intense erosion in a transport limited stage, can prepare a following sediment supply limited branch and this kind of phenomena cannot be captured by a simple SRC analysis.

In their simple types, hysteresis curves take circular, elliptical, bilobate or lemniscate shape, with either clockwise or counterclockwise branches. For example, if the sedimentation process is dominant the hysteresis is usually clockwise, bed and bank erosion dominance drive to counterclockwise hysteresis (Malutta, 2020).

In analytical terms, the hysteresis loop is the result of the temporal uncoupling (Yang and Lee, 2018) between solid (SSC) and liquid (Q) discharges (Fig. 3.1.19).

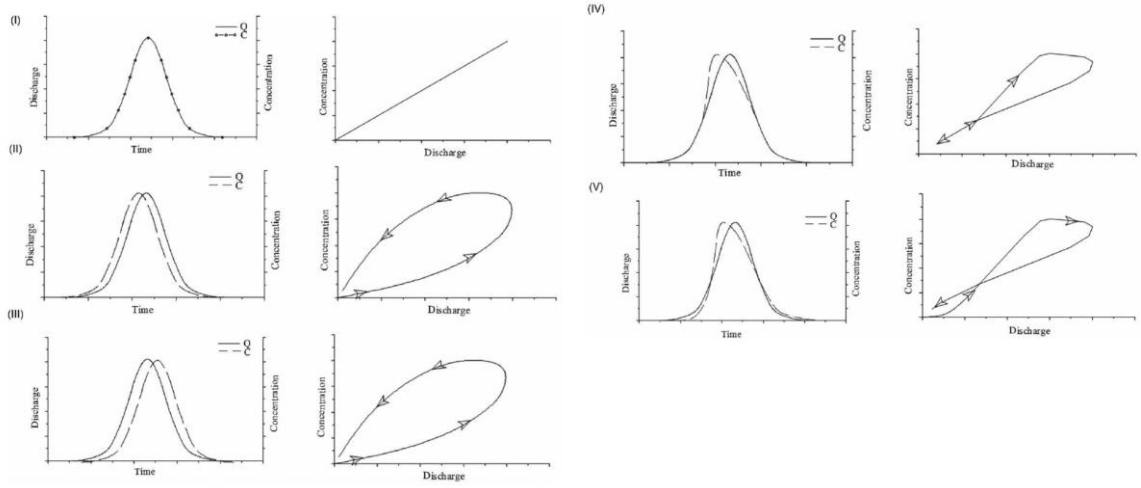

Fig. 3.1.19 – An analytical scheme for hysteresis loop types.

Malutta et al. (2020) suggest a comprehensive interpretation of the hydro-morphologic causes responsible for the main types of hysteresis loop curves (Tab. 3.1.1.).

Patterns	Cause of hysteresis
I. Single-valued line	Discharge travel time equals the sediment travel time Abundance of fine-grained sediments in the channel Low availability of fine sediment Uninterrupted supply of sediment/remobilization and transport of in-channel followed by a supply from distant sources
II. Clockwise loop or positive hysteresis	Mobilization followed by depletion of in-channel/ nearby sediment sources/exhaustion effects after an initial flush of sediment
	Formation of armored layer before peak discharge Bank erosion Increased base flow after peak discharge leading to dilution of sediment concentration Snowmelt runoff events Individual floods Wash load (silt/clay) Areas of the sediment yield are short/near-channel source/early sediment supply by the tributaries or flowpaths temporal and spatial differences between SS production and water discharge generation in small basin
III. Counterclockwise loop or negative hysteresis	Floodwave traveling faster than mean flow velocity/ sediment wave travels slower than the discharge wave High soil erodibility Bed and/or bank erosion
	Distant sediment source/upstream tributaries/late sediment supply by the tributaries
	Seasonality, lower concentrations early in the year followed by increasing sediment concentrations Exhaustion of sediment available due to previous event Valley slopes form the most important sediment source The distribution of non-uniform sediment yield in the basin
	Small events with high rainfall intensity and very dry soil conditions Channel deposition (analyses sub-basin) During winter freezing – river cross-sections are often fully closed with ice Influence of the sea tide on hysteresis Landslide Very high moisture and high antecedent rainfall conditions
IV. Single line plus a loop	This indicates if the sediment travel time is distinct from the flow travel time in separate runoff states Occurs under extreme dry conditions
V. Figure eight	Ice breakup Delayed contribution of sediment from sub-basins Influences of drainage system Multiple peaks
	Sediment contribution from the streambed and its banks
VI. No hysteresis/random/ stationary	Uninterrupted supply of sediment/sediment was still available/soil surface was not protected sufficiently with vegetation cover Snowmelt and rain events Long events; multiple peaks; multitude of factors of sediment delivery

Tab. 3.1.1 – Summary of potential causes for the loop shape.

The very uncommon single-valued line is given by a pure suspended transportation event, where neither re-sedimentation or re-mobilisation occur. The clockwise loop is produced when in the falling limb the SSC-Q relation decreases, with a transport limited behaviour; counterclockwise loop attests for sediment supply limited conditions or far sediment yield areas. According to Eder et al. (2000), the lemniscate pattern "can be related to: (i) the sediment deposited on the bed or banks of the channel that goes into resuspension; (ii) the time of sediment travel in upstream sub-basins; (iii) the fact that there may be an upstream storage area in the basin and, after its saturation, the contribution of the discharge and sediment downstream; and (iv) influences of the drainage system".

In Figures 3.1.20 - 3.1.26 the annual hysteresis loops for the analysed database are depicted. The general scenario is marked by a large number of different shapes and directions, with recurrent very irregular cases attesting the complexity of the dynamic which rules the erosion process in the Sicilian catchments.

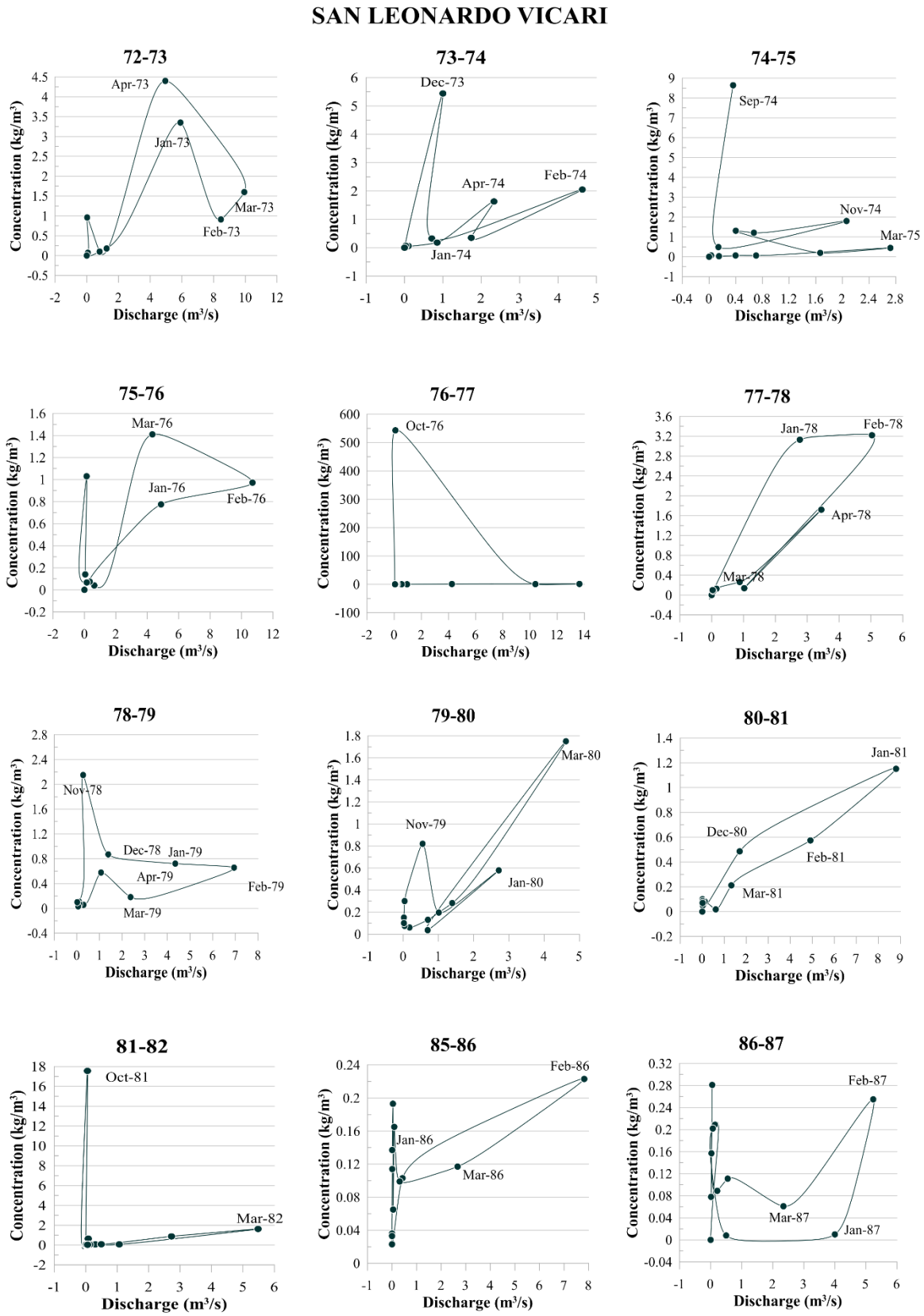

Fig. 3.1.20 – Hysteresis loops for the 'Vicari' section of the San Leonardo River basin.

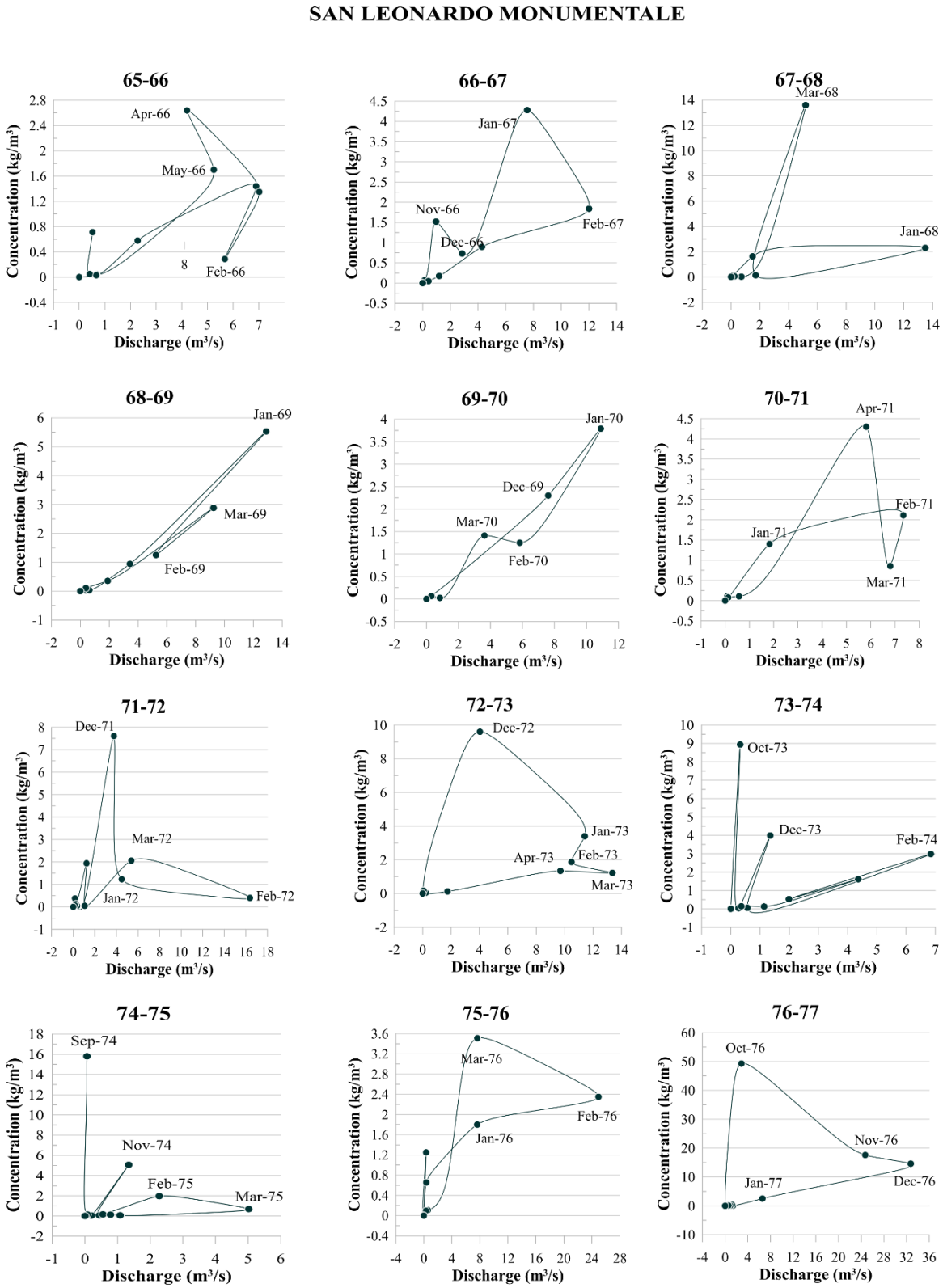

Fig. 3.1.21 a) – Hysteresis loops for the 'Monumentale' section of the San Leonardo River basin.

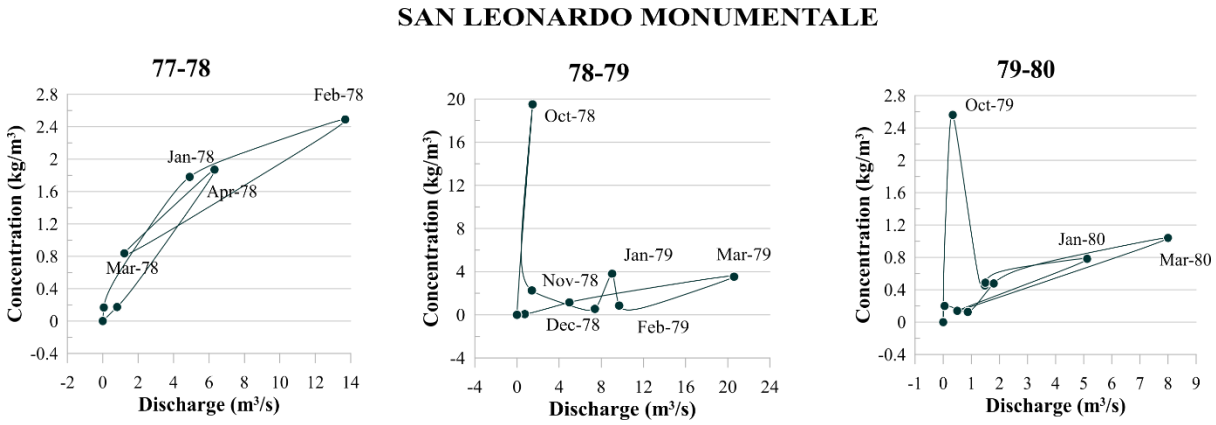

Fig. 3.1.21 b) – Hysteresis loops for the 'Monumentale' section of the San Leonardo River basin.

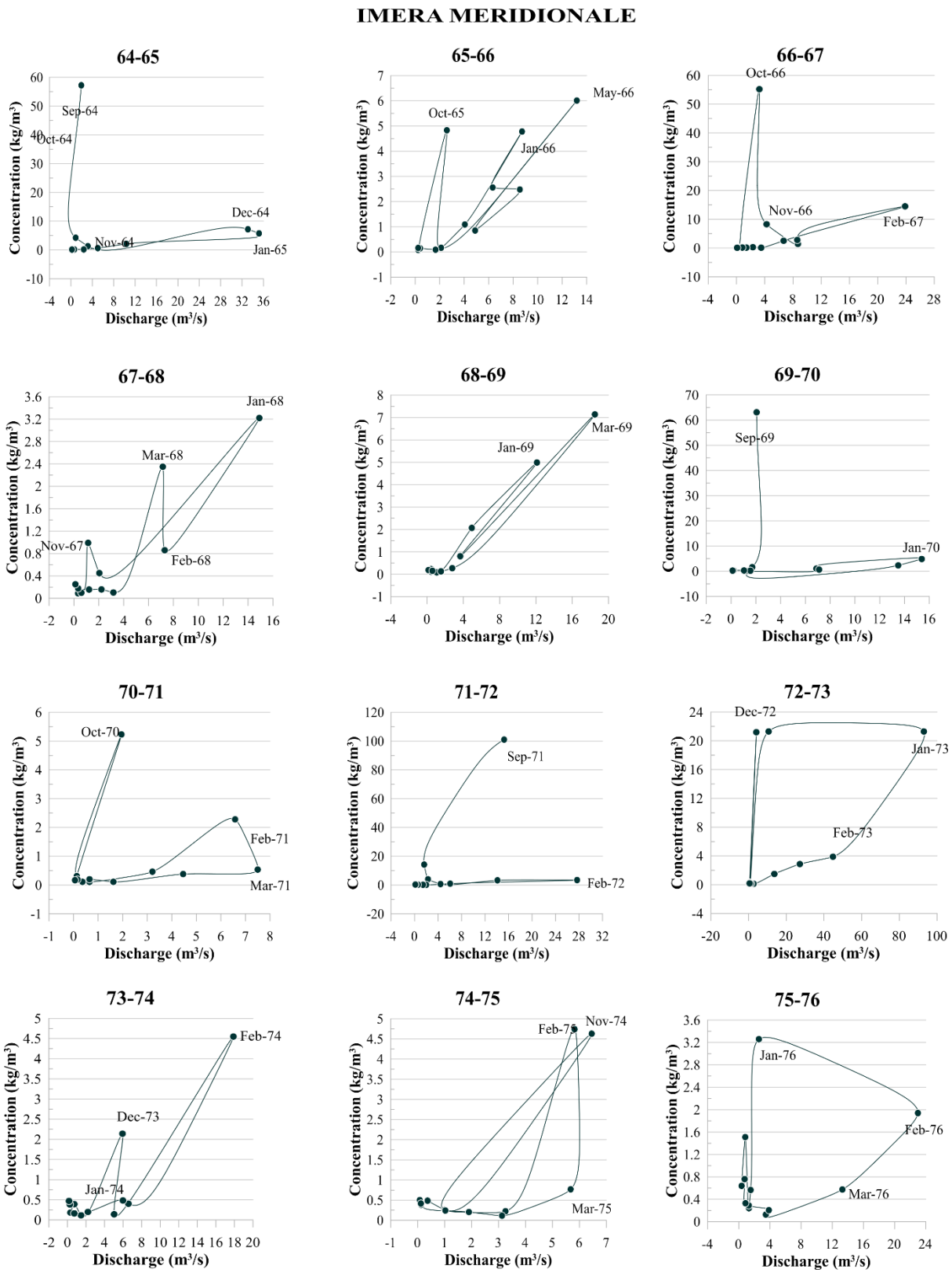

Fig. 3.1.22 a) – Hysteresis loops for the 'Drasi' section of the Imera Meridionale River basin.

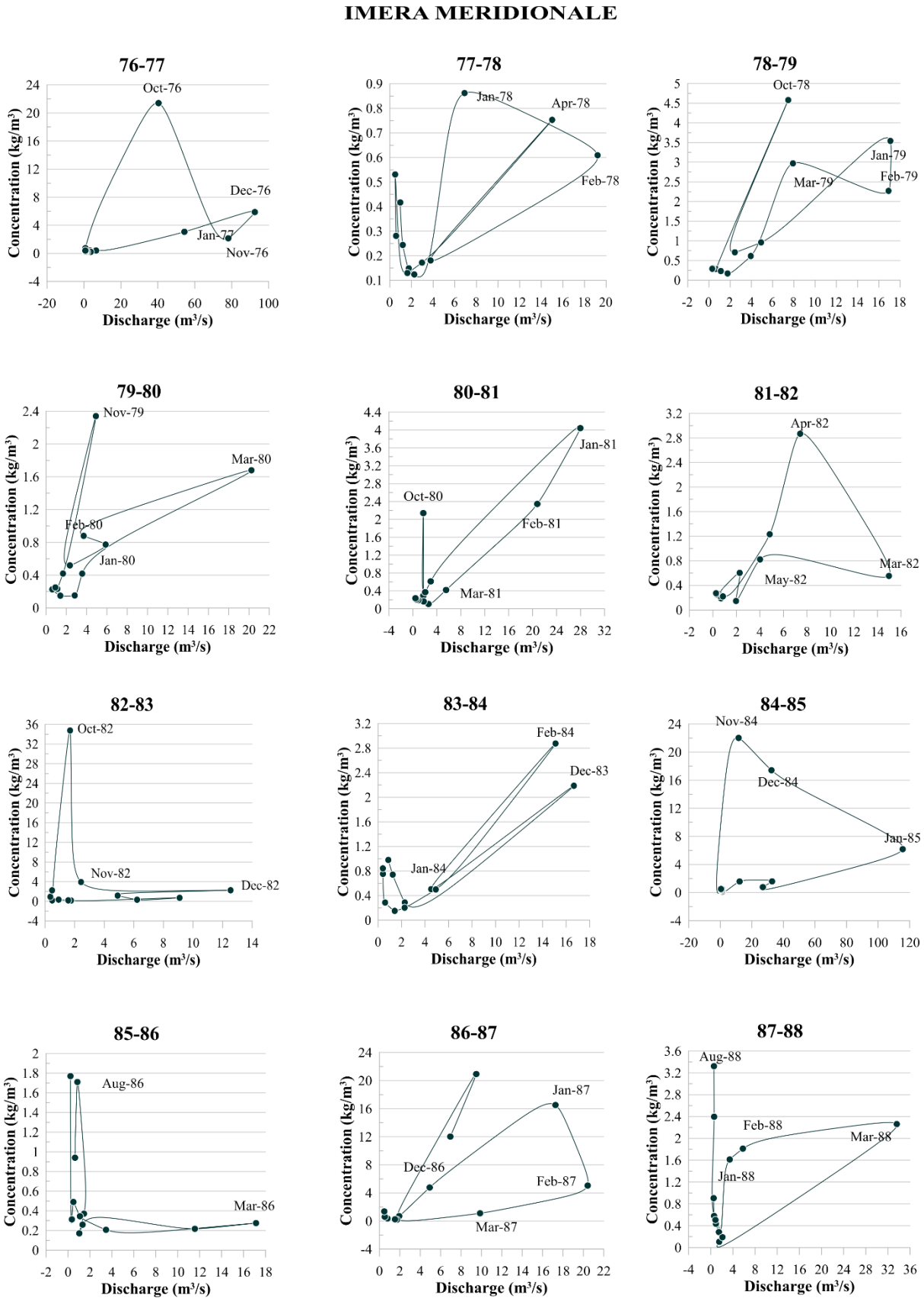

Fig. 3.1.22 b) – Hysteresis loops for the 'Drasi' section of the Imera Meridionale River basin.

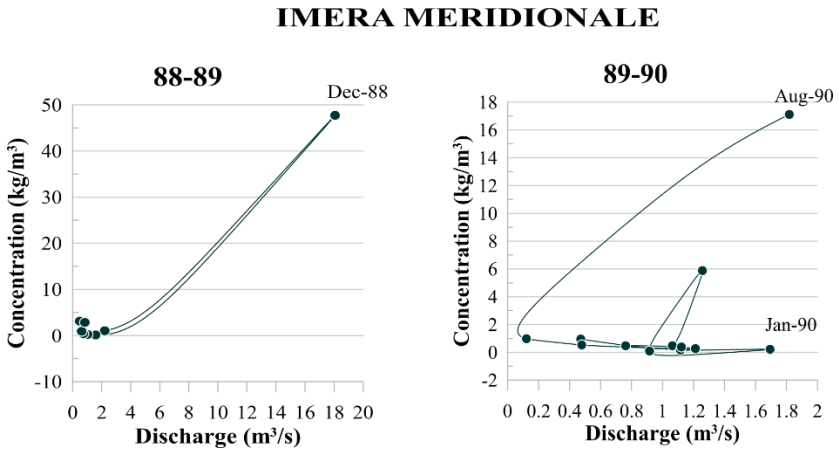

Fig. 3.1.22 c) – Hysteresis loops for the 'Drasi' section of the Imera Meridionale River basin.

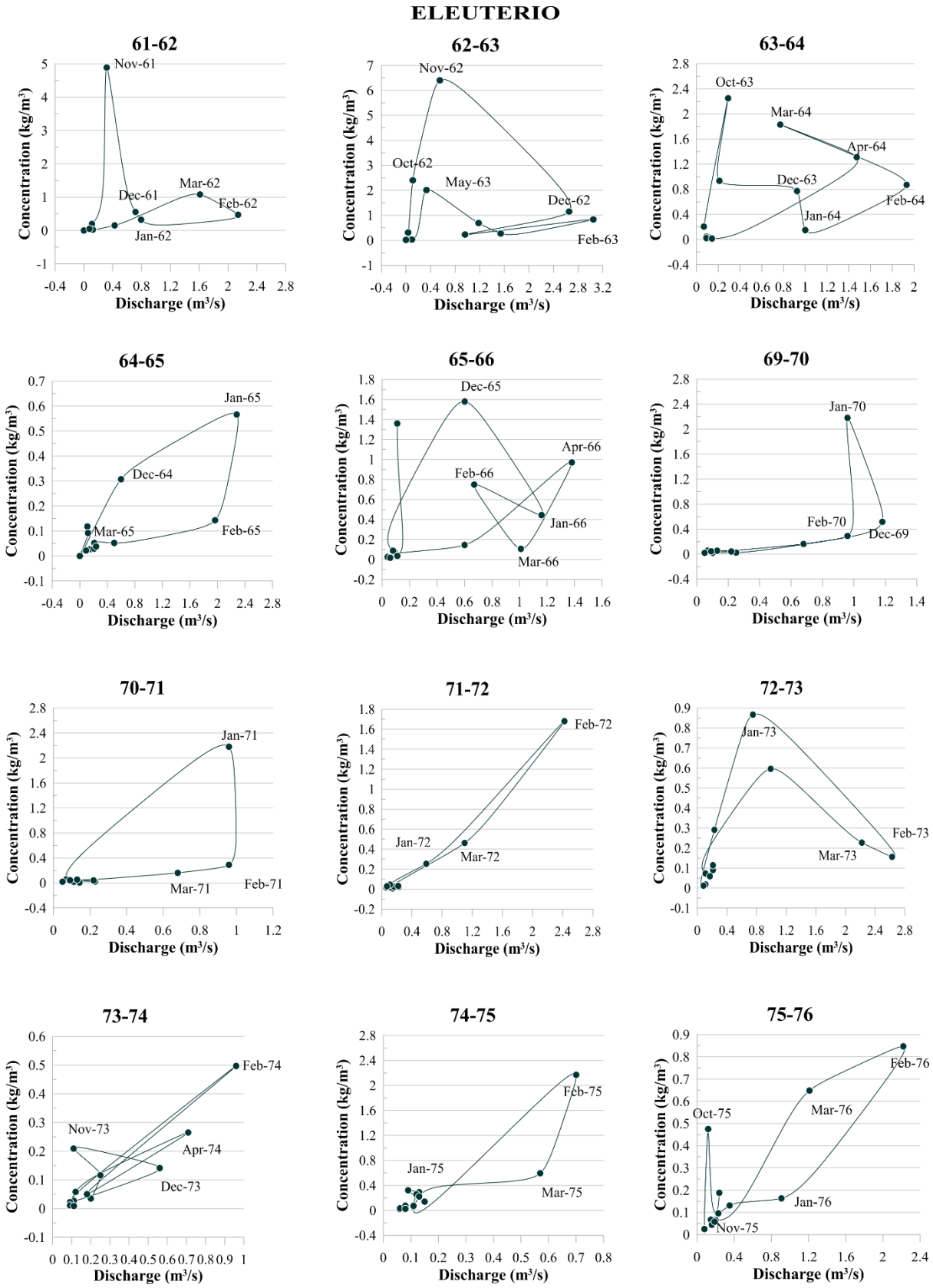

Fig. 3.1.23 a) – Hysteresis loops for the 'Risalaimi' section of the Eleuterio River basin.

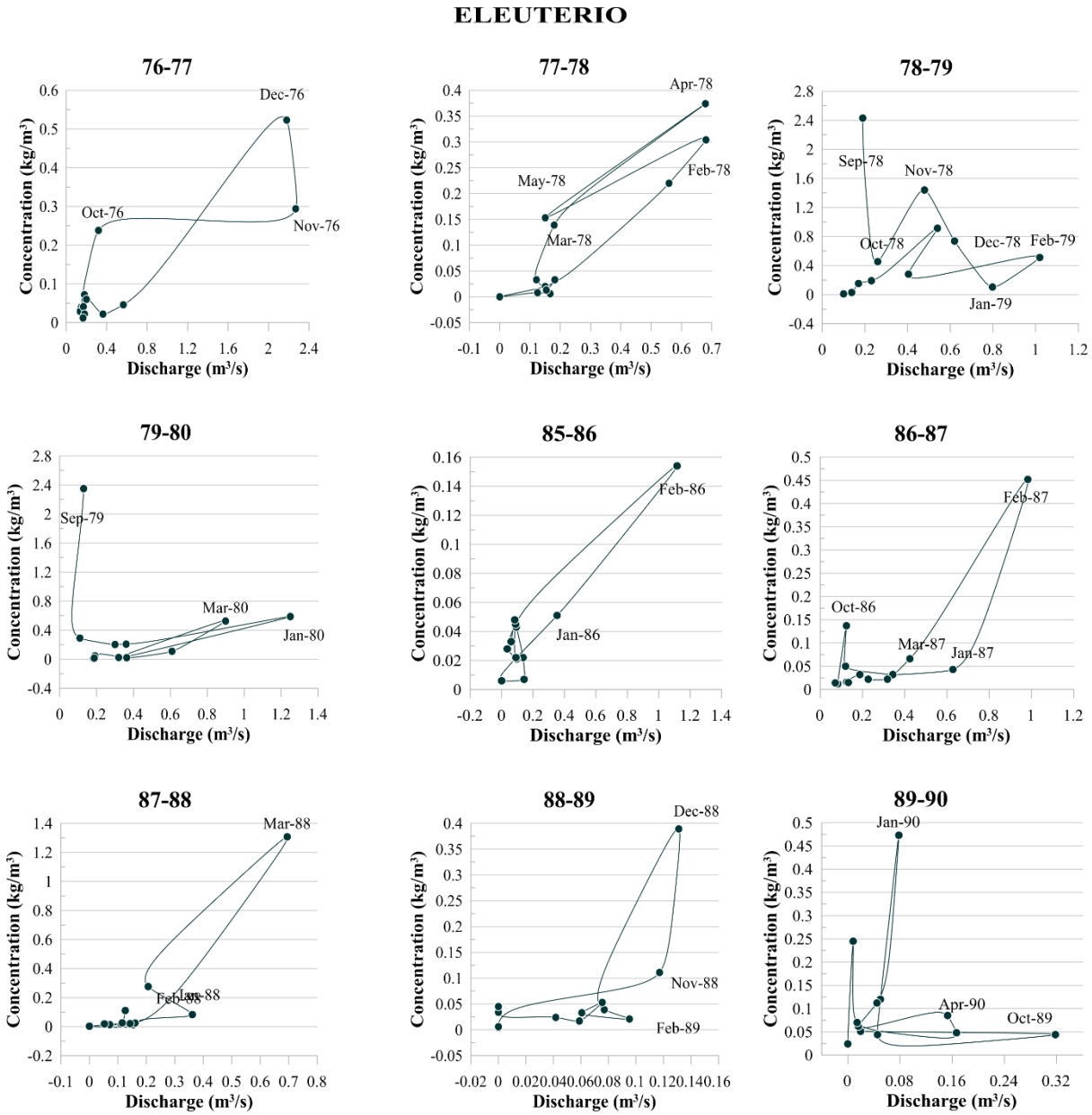

Fig. 3.1.23 b) – Hysteresis loops for the 'Risalaimi' section of the Eleuterio River basin.

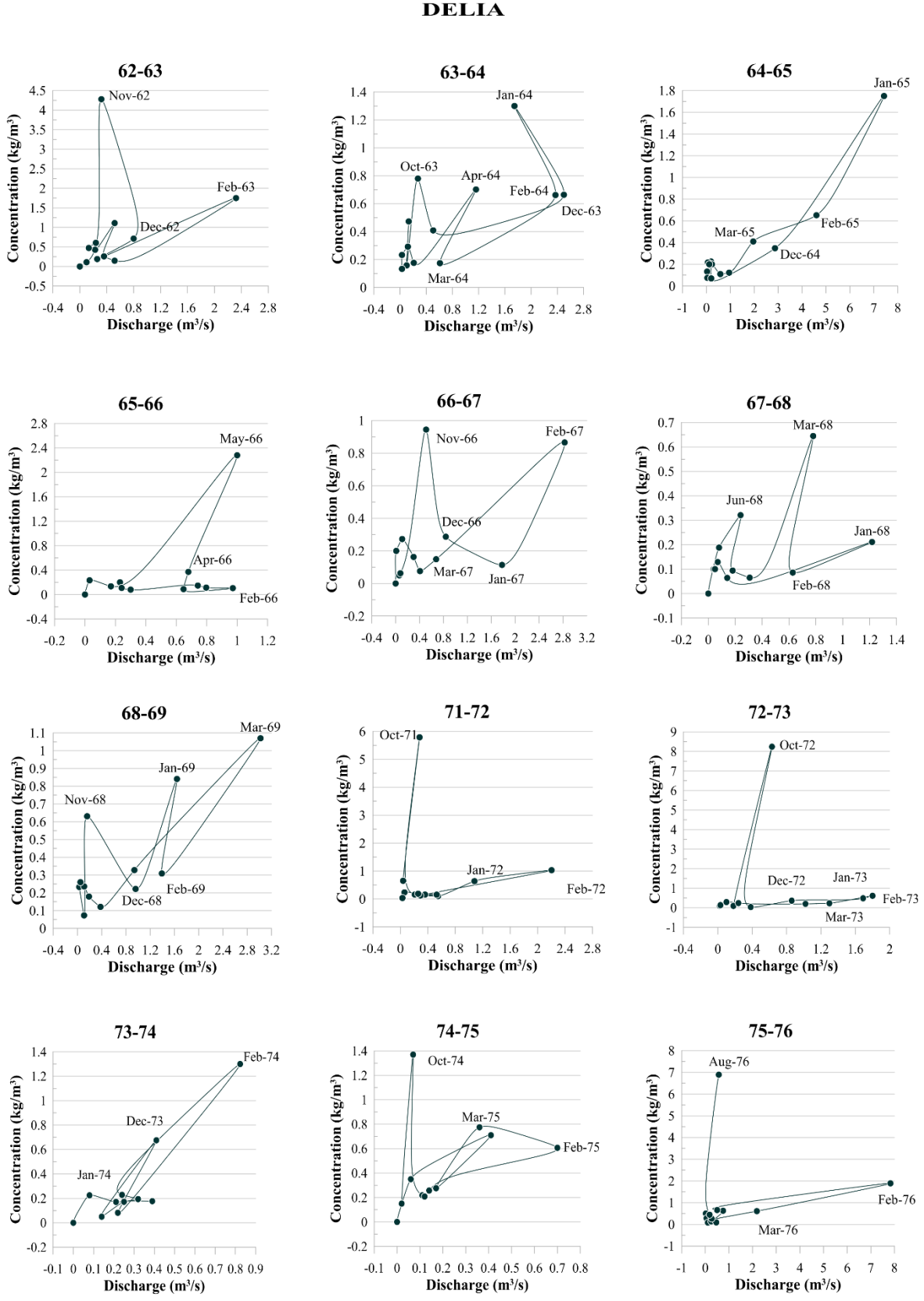

Fig. 3.1.24 a) – Hysteresis loops for the 'Pozzillo' section of the Delia River basin.

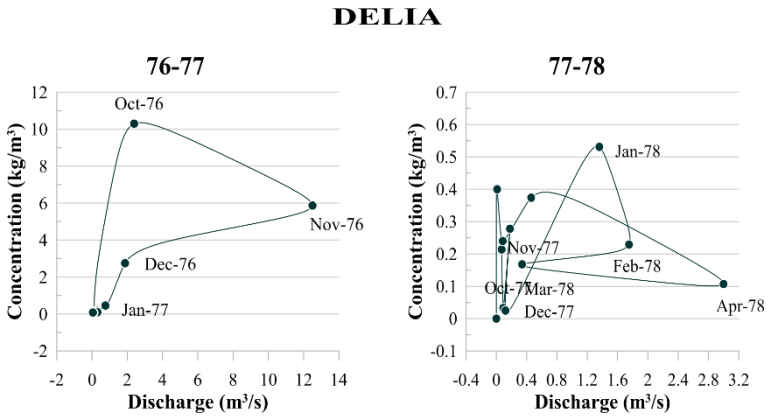

Fig. 3.1.24 b) – Hysteresis loops for the 'Pozzillo' section of the Delia River basin.

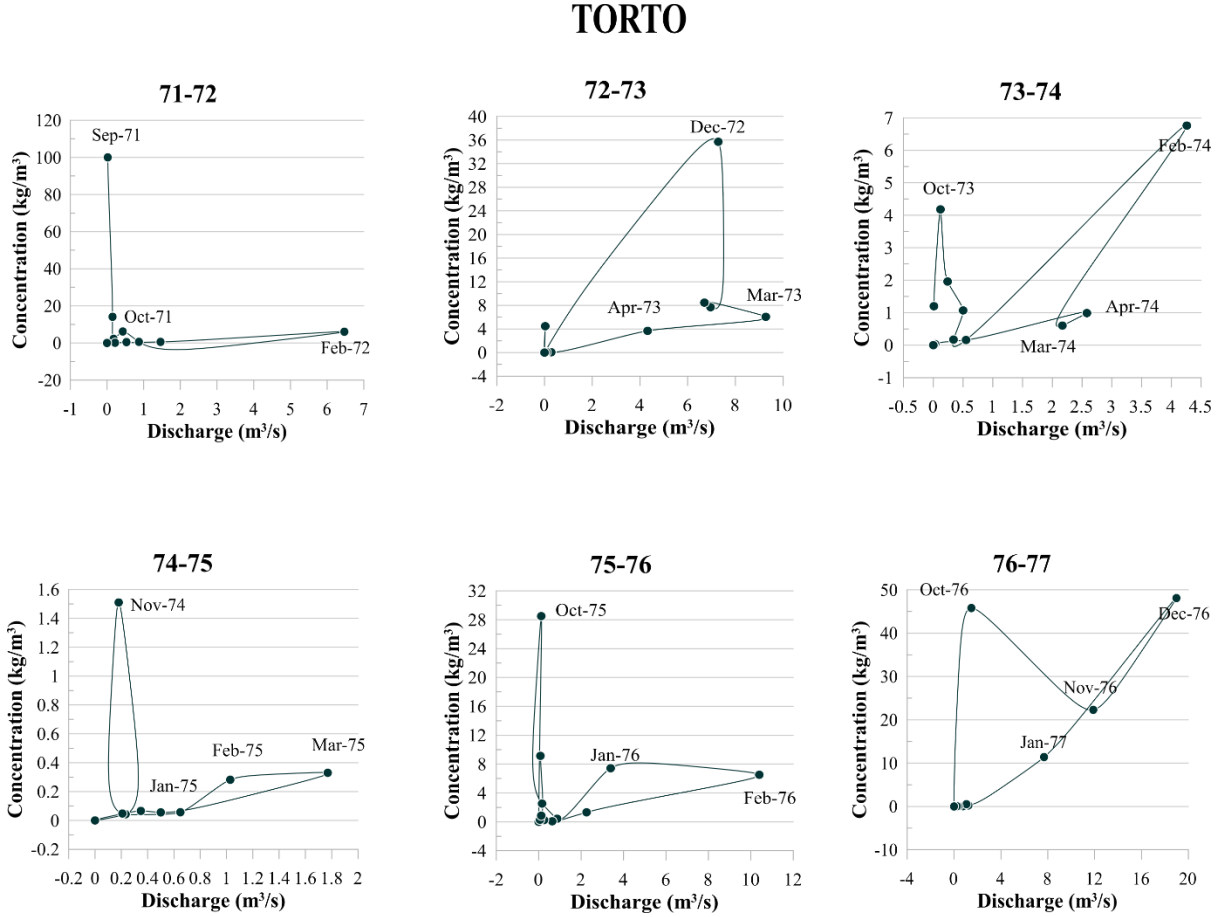

Fig. 3.1.25 – Hysteresis loops for the 'Bivio Cerda' section of the Torto River basin.

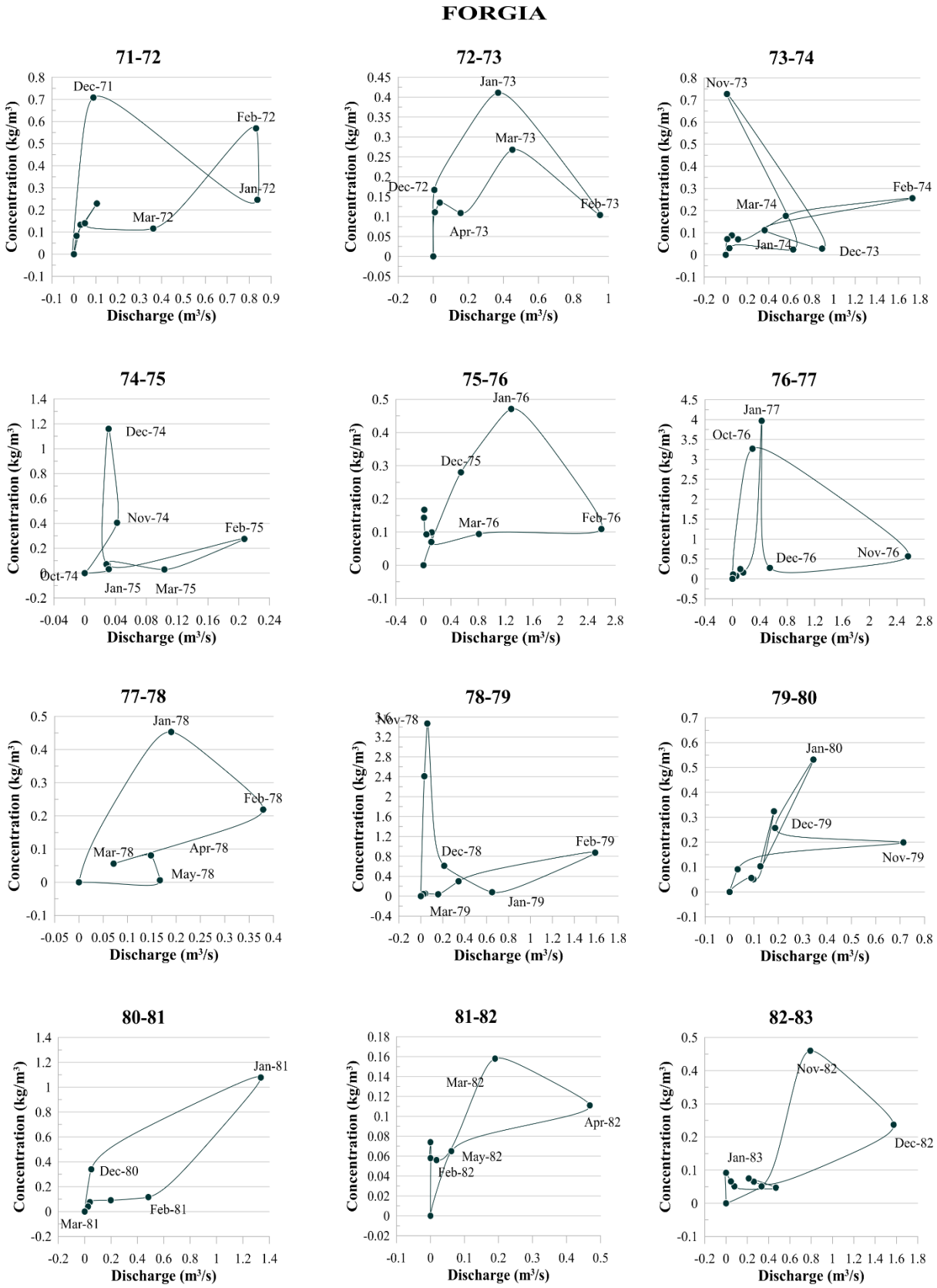

Fig. 3.1.26 a) – Hysteresis loops for the 'Lentina' section of the Forgia River basin.

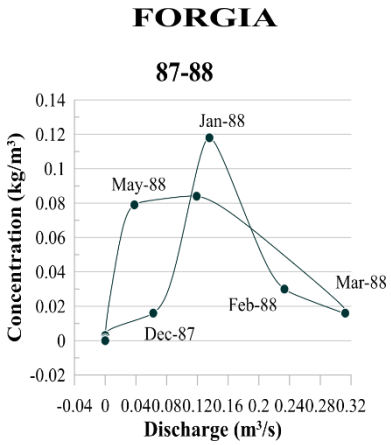

Fig. 3.1.26 b) – Hysteresis loops for the 'Lentina' section of the Forgia River basin.

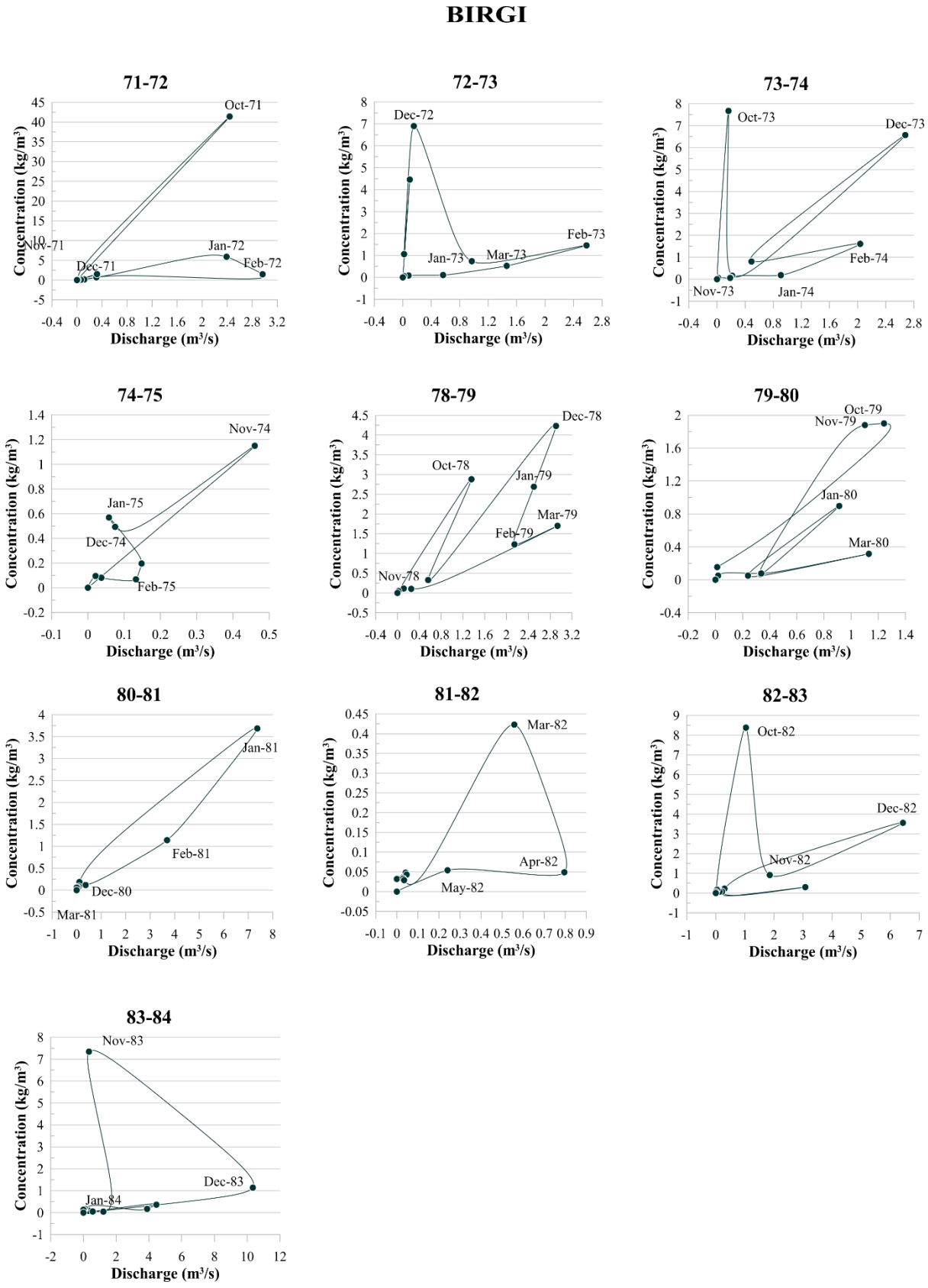

Fig. 3.1.27 – Hysteresis loops for the 'Chinisia' section of the Birgi River basin.

In order to derive a more regular and general scenario of the hysteresis loops, mean annual values were plotted for each gauge station. In this way, the singularity of very peaked events was blurred an more regular loops were observed, which can be interpreted referring to the main general hydro-morphodynamic of both the erosion and transportation phenomena.

According to the obtained hysteresis, the following pattern were recognized: Eleuterio – Risalaimi, Imera Meridionale – Drasi showed a marked high autumnal lobe and a near linear winter lobe. In the case of Forgia – Lentina and Delia – Pozzillo, a clockwise winter short lobe is recognized, whilst at San Leonardo – Monumentale a clockwise lobe marks the winter stage. The same San Leonardo River, at the Vicari gauge station gave a clear lemniscate pattern, with high counterclockwise winter lobe. The absence of autumn data at the Birgi – Chinisia gauge station results in a regular semielliptical counterclockwise pattern, while at the Forgia – Lentina gauge station, a circular counterclockwise pattern is associated with a small clockwise flake in winter. Finally, the Torto – Bivio Cerda pattern is strongly affected by high discharge in February and high transportation in September.

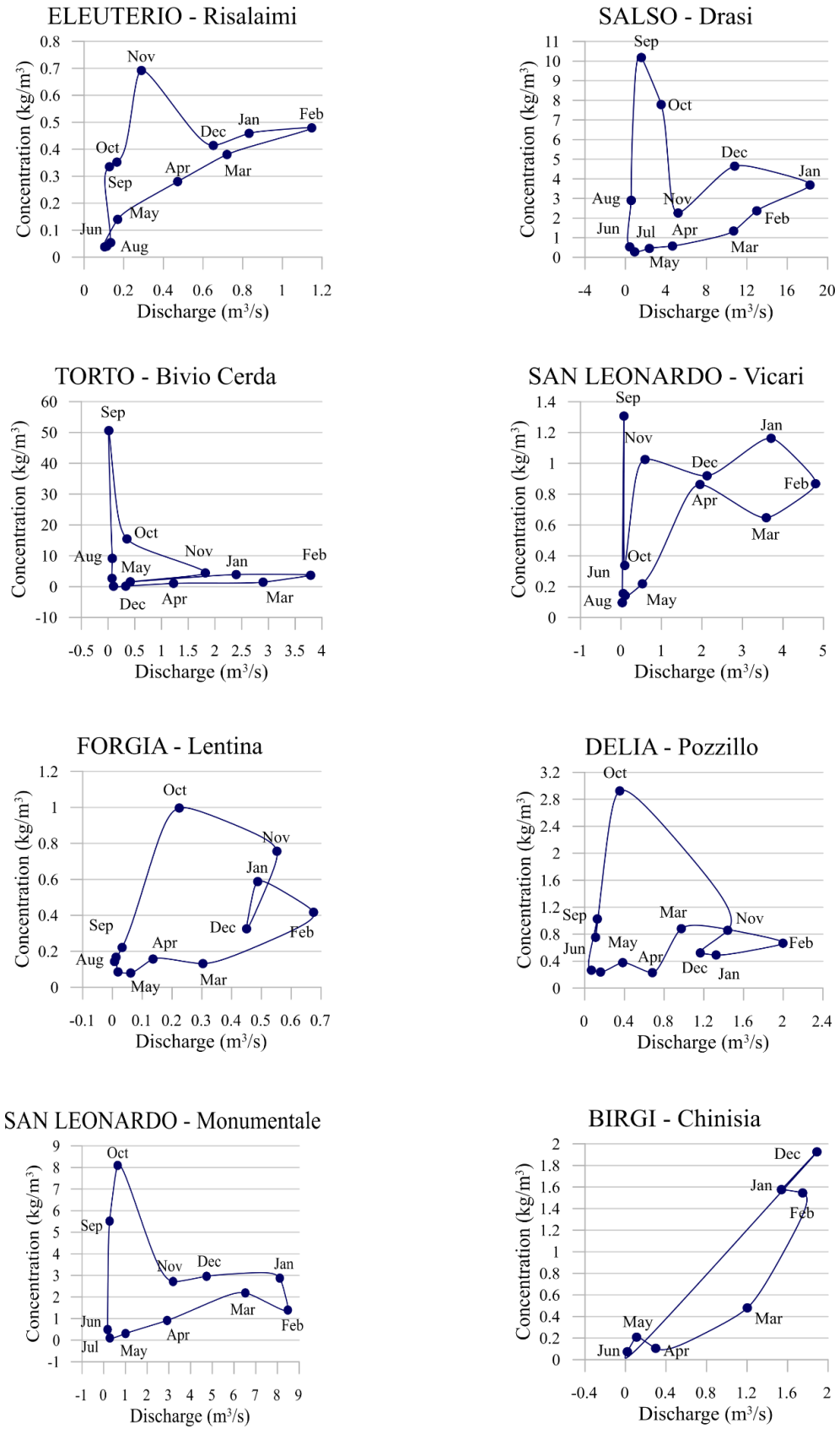

Fig. 3.1.27 – Mean hysteresis loops for all the river basins.

3.1.5 Discussion and Conclusions

Thanks to the analysis of the sediment yield data which was carried out in the framework of this thesis work, a first picture of water erosion processes in Sicily, under moderate anthropogenic disturbances was drawn. This reference picture characterization furnishes a useful comparison term for investigating any climate change-induced effect on the soil loss risk scenario.

The main characteristics of the SRCs and SSC Vs. Q trend (both at the annual and hysteresis temporal scale) attests to the complexity and variability of the erosion processes in Sicily, with two strongly different stages, each characterized by a specific behavior. In spite of a general regional trend which suggests for transport limited processes, going at local scale it has been possible to recognize both a transport limited autumn stage and a supply limited winter season. This is potentially due to very intense sediment production on the hillslopes in the autumn season which cannot is not efficiently delivered to the main channel for a lack of runoff connectivity and transport capacity. At the same time, the inner gauge station indicates that intense near-channel process allows for the low discharge to transport suspended sediment. In the winter season, the higher discharges on the channel are not efficiently supplied by sediments because the near-channel sediment has been washed out during autumn and, still, the annual sediment production on the hillslope is only partially delivered through the drainage network down to the main channel.

With a hydro-geomorphological perspective, soil erosion processes in Sicily seem to be controlled by the following phenomena:

Autumn rainfall is typically characterized by short duration, high intensity, and intermittence, which result in high erosivity but low runoff coefficients. At the same time, the summer season leaves soils very dry and cracked; this also produces very low water content and high infiltration of soils, which results in severe water capturing at the first rainfall event stage. This rainfall forcing results in:

- Intense soil erosion processes on the hillslopes.
- Poor connectivity between soil yield areas and the main channel through the drainage network.
- Effective near-channel erosion production caused by bank erosion and flow slope foot landslides.
- Intermittent and low-discharge base flow.

The result of the interplay between the above-mentioned conditions is a transport-limited scenario, where small water volumes characterised by high turbidity cross the gauge stations.

Winter rainfalls are typically characterised by long periods with less intensity, resulting in lower erosivity and high runoff coefficients. This type of rainfall forcing results in:

- Moderate erosion processes on the hillslopes.

- Moderate connectivity between soil yield areas and the main channel through the drainage network.
- Effective near-channel erosion production caused by bank erosion and flow slope foot landslides.
- High base flow.

The result of the interplay of these conditions is a sediment supply which is higher in volume but not high enough to fit the available transport capacity, probably due to an irregular runoff connectivity.

The above described scenario seems to result in a positive sediment balance, with a short duration transport limited high erosive autumn stage and a long duration supply limited less erosive winter stage. The comparison with the denudation processes on the hillslopes suggests the possibility that very extreme events could easily capture all the available sediment from hillslope to channel, preparing long lasting supply limited periods.

The analysis of the historical suspended sediment concentration means monthly data required an adaptation of both of the approaches and interpretative models in SRCs and hysteresis loops analysis, allowing to reconstruction of the main erosive behavior for the Sicilian catchments. In particular, a clear seasonal changing on the dominant relations between liquid and solid discharges has been recognized, which can be taken as a reference pattern for comparing any available present data series to explore potential disturbances induced by the climatic (global warming) or anthropogenic stresses (land use changings).

3.2 MODELLING SOIL EROSION WITH SWAT IN MEDITERRANEAN WATERSHED

Water erosion is a major concern for land degradation in a wide range of natural environments, particularly in semi-humid to arid areas. In areas with a Mediterranean climate, quantification of soil erosion and sediment transport is a challenge, depending on the great variability of the physical characteristics of the watersheds and on the peculiarity of the hydrological regime of streams that are generally intermittent. Moreover, the Mediterranean region is especially vulnerable to water erosion because of climate changes that cause long dry periods followed by extreme rainstorms, as well as the recent increase in human activity and agricultural practices. Healthy plant growth on abandoned lands and soil and water conservation can significantly reduce soil erosion. In contrast, unsustainable farming methods, wildfires, deforestation, overgrazing, land abandonment, roads and railway construction can increase the risk of soil erosion susceptibility and land degradation. While numerous models can predict soil erosion and sediment yield, only a select few simulate the water cycle, making them ideal for evaluating the impacts of climate and land-use changing as well as management practices. One of the models that is widely used globally is the Soil and Water Assessment Tool (SWAT). It has shown promising results, particularly at annual and monthly scales, in assessing runoff and sediment yield, even for large catchments where data are poorly available. The goal of this study was to find out if SWAT was capable of accurately predicting discharge and sediment transport in a Mediterranean watershed using a historical dataset.

3.2.1 CASE STUDY AREA

In this research, the SWAT model was applied to the San Leonardo Watershed (Fig. 3.2.1). This basin is situated in the northern sector of Sicily, draining into the Tyrrhenian Sea. It covers an area of 506 km^2 exhibiting a sub-circular shape with a northern extension in the NNE-SSW direction. Its width reaches a maximum of approximately 22 km to the south while it diminishes to just over 1 km, around 3.5 km from the mouth, at the Rosamarina gorge, where the dam of the same name has clocked the river.

The basin is located between the coastal chain of Trabia Mountains, Mount San Calogero, and the Sicani Mountains, and it is bordered on the southeast by the Torto Watershed, on the south by the Platani and Verdura Watershed, on the southwest by the Belice Watershed and, on the west by the Milicia Watershed.

In particular, the watershed divide develops east along the peaks of Mt. Pileri (378 meters), Mt. Guardiola (700 meters), Mt. Rotondo (845 meters), Mt. Sughero (620 meters), and Mt. Castagna del Barone (714 meters). Still to the east, the path continues along the peaks of the Montagnola (833 meters) and Mt. Todaro (875 meters). To the south, proceeding from east to west, the watershed develops along the peaks of Mt. Volturo (1.103 meters), Mt. Sparagio (1.118 meters), and Mt. Cangialoso (1.457 meters). To the west, the watershed follows the ridge generated by the succession of the peaks of Mt.

Barracù (1.420 meters), Mt. Cardellia (1.266 meters), Rocca Busambra (1.614 meters), and Mt. Bileo (1.007 meters). The path continues along the peaks of Mt. Lungocucco (718 meters), Mt. Cascio (1.054 meters), Mt. Garofano (1.204 meters), and, finally, Mt. Rosamarina (540 meters).

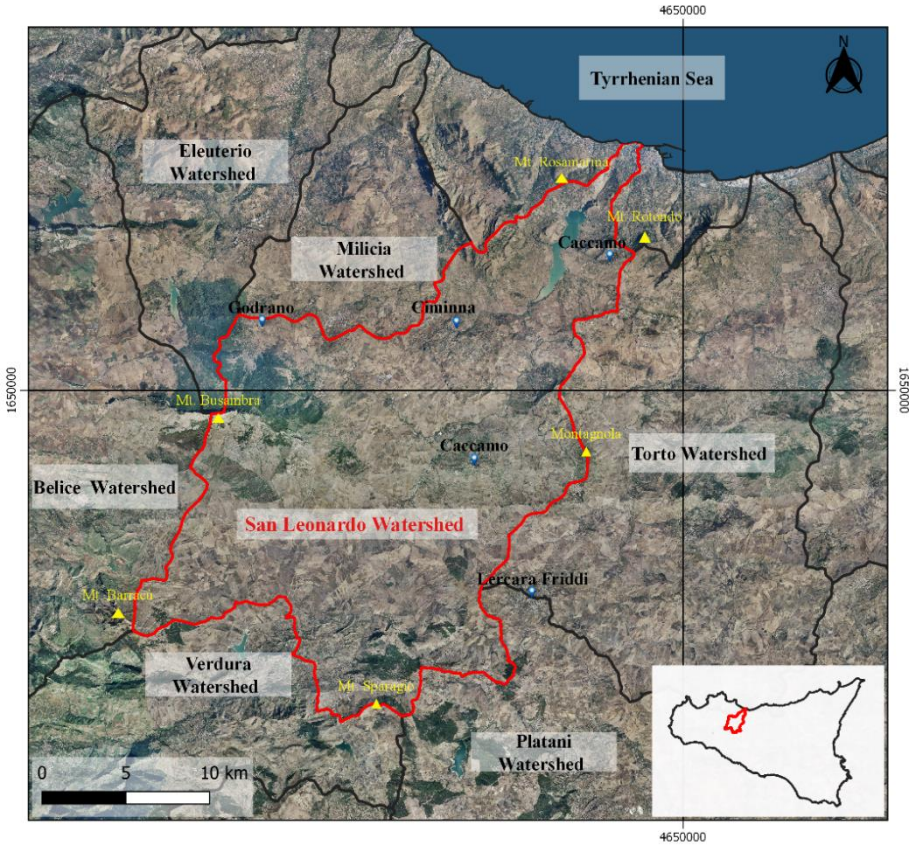

Figure 3.2.1 - Location of Study Area

The topography and geomorphology of the San Leonardo basin are the result of the constructive (Miocene and Plio-Quaternary compressive tectonic phase) and destructive (by the exogenous agents) forces that followed the collision between the African and the European plates and the construction of the western Sicily Fold and Thrust Belt. This determined a profound deformation of the Paleozoic-Mesozoic to Paleogene rock assemblages of distinct paleogeographic domains (carbonate basinal and platform successions) which belonged to the "Tethyan" ocean and the African continental margin and the formation of a complex chain of thrust imbricates, locally more than 15 km thick, consisting of Structural Stratigraphic Unit (U.S.S.). These bodies are bound by clear, mappable tectonic features (faults, thrust surface, etc.), and each one is characterized by homogeneous lithologies and the same structural behavior and setting.

In particular, in the area object of this study, the following Structural Stratigraphic Units can be recognized:

- U.S.S. deriving from the deformation of the Sicano Domain:
    - Mt. Barracù – Mt. Colomba (Upper Trias. – Tortonian)

It consists of a sequence of marls with foraminifera, calcilutites and partly silicised and dolomitic limestone, red and green marl, radiolarites, calcilutites with calpionelle, biocalcarenites, glauconitic biocalcarenites and marl sandy.

  - Mt. Rose (Upper Trias – Tortonian)

    It consists of Noric limestones, followed by marls and calcilutites of the Eocene "Scaglia", covered in discordance by limestones and sandy clays.

  - Roccapalumba. (Upper Trias. – Lower Miocene)

    The lithotypes are represented by terrigenous-carbonates clastic deposits (Fm. Lercara), stratigraphically followed by calcilutites and calcarenites with radiolaria and lamellibranch (Halobia).

- U.S.S. deriving from the deformation of the Trapanese Domain:
  - Monte Kumeta (Upper Trias – Lower Miocene)

    This unit outcrops between the south-eastern slopes of Rocca Busambra and the town of Campofelice di Fitalia and consists of calcilutites and calcarenites.
- U.S.S. deriving from the deformation of the Imerese Domain:
  - Pizzo di Cane (Upper Trias – Upper Eocene)
- Unit of the Numidic Flysch (Oligocene – Lower Miocene)

  This unit consists of pelites and clayey pelites with interbedded arenaceous layers, biocalcarenites and carbonates megabreccias; quartzarenitic strata with microconglomeratic layers and sandy siltstones. These deposits are followed, through a sharp unconformity, by brown-yellowish sandy-pelitic marls with interbedded layers of micaceous and glauconitic arenities with arenaceus and planktonic foraminifera, calcareous nannofossils (Tavernola Fm, Upper Burdigalian – Langhian).
- Unit of the Sicilide Complex (Cretaceous – Lower Pliocene)

  It consists of Cretaceous clays, reddish marls, chaotic at the bottom, varicolored argillites with intercalation of calcarenites, and greenish calcilutites with ichnofossils. Grey to whitish marly limestones, locally thinning laminated, alternating with greyish and bituminous marly clayey layers containing planktonic foraminifera and calcareous nannofossils (Polizzi Fm, Middle - Upper Eocene).

  The outcrops consist of "klippen" that emerge in the north-eastern areas of the basin, in municipal territory of Caccamo.

This heterogeneous scenario influences the topography and the morphology of the basin with frequent and rapid variations in altitude attributable to the alteration of successions of “hard” and “resistant” rocks hundreds of meters thick (Mesozoic carbonate units) coincident with the mountain range and the isolated peaks with very steep slopes, and “weak” and easily erodible rocks (calcilutites, marls, and clays of the Mesozoic basin units), that constitute rounded hills with gentle slopes. Gravity, flowing water, and weathering are the main forces behind the hillslope processes. The lithoid outcrops with

steep and sub-vertical slopes are weakened by weathering processes that act in synergy with the differences in altitude, making them optimal sites for occurring gravitational phenomena such as rockfalls and topples.

In the clayey hillslopes, the environmental modeling is exerted by the erosive action of the water, which acts as unconcentrated surface flow or concentrated flow generating rills and gullies, mainly where a low percentage of forest covers the area. The process of erosion and denudation is exacerbated, resulting in calanchi, particularly in steep and unvegetated slopes that delimit the stream segment near Ciminna and Caccamo.

There are different types of gravitational hillslope processes in the San Leonardo River Basin, mainly affected areas with a prevalence of clayey outcrops. The most common typologies of landslides are flow, rotational and translational landslides, and complex landslides. In the presence of chalky rocks, karst modeling phenomena are observed, such as dolines of circular or elliptical shape and other microforms (grooves, karren etc.).

The hydrologic setting of the San Leonardo Basin is also influenced by the rough morphology of the environment. The smaller river segments, of low stream order, have a high slope gradient and create a sub-dendritic drainage network, while the segments of higher order show meandered channels indicating low slope gradients.

The San Leonardo River was born on the slopes of Mt. Cangialoso (1456 m) in the municipality territory of Corleone with the name of "Vallone Margi". It proceeds from the spring to the mouth, along a path of almost 58 km, crossing the territories of Vicari, Ciminna, Caccamo, and Termini Imerese and assuming different names. At an altitude of 290 meters and about 245 km from the source, the river receives on hydraulic right the waters of Margana River and after this confluence, is called "Vicari River". The river takes the name of San Leonardo River after the confluence with San Domenica River, at an altitude of about 270 meters and a distance from the source of about 27 km. It ends its path flowing into the Tyrrhenian Sea a short distance from the Termini Imerese town.

The longitudinal profile of the San Leonardo River shows a very low average slope, equal to 2.33%. However, lithological changes and/or tectonic discontinuities generate variation in the gradients.

3.2.2 Input Data & Model Set-Up

The QGIS extension, QSWAT, was employed to implement the Soil and Water Assessment Tool (SWAT) model, which involves three modules for data preparation. The first module is the SWAT Watershed Delineator, allowing users to discretize the watershed and sub-watershed based on data derived from the Digital Elevation Model (DEM). Subsequently, the SWAT HRU (Hydrologic Response Unit) analysis tool integrates information from land use, soil characteristics, and slope maps to discretize the HRUs. The third module, the SWAT Input Editor, facilitates the creation of an input database and the modification of all model parameters.

- SWAT Watershed Delineator

To delineate the San Leonardo River Basin watershed, a Digital Elevation Model (DEM) with a 2-meter resolution obtained from LIDAR data in 2012-2013 (https://www.sitr.regione.sicilia.it/geoportale/) was used and resampled to a 25-meter resolution using B-spline Interpolation in SAGA GIS.

Since this model of digital elevation (DEM) shows the effect of the Rosamarina dam, it was necessary to eliminate this influence and recreate a model of elevation that reflected the topographical situation before the construction of the dam. To achieve this goal, the map sheet 259 of Termini Imerese, of the IGM series and dating back to 1970, was used. The elevation was reconstructed from this map using the Topo to Raster tool in Arc Gis Pro and later, using the SAGA GIS mosaicking tool, this elevation was merged with the original DEM, creating a unified grid.

The following step was the subdivision of the watershed into subunits called subbasins, each containing a main channel or reach. To delineate these subbasins and the channel network, the unified DEM has been processed using various analysis tools of the Library Hydrology in SAGA GIS. The watershed delineation resulted in 29 subbasins (Fig. 3.2.2) that gave a suitable representation of the observed drainage network geometry and density.

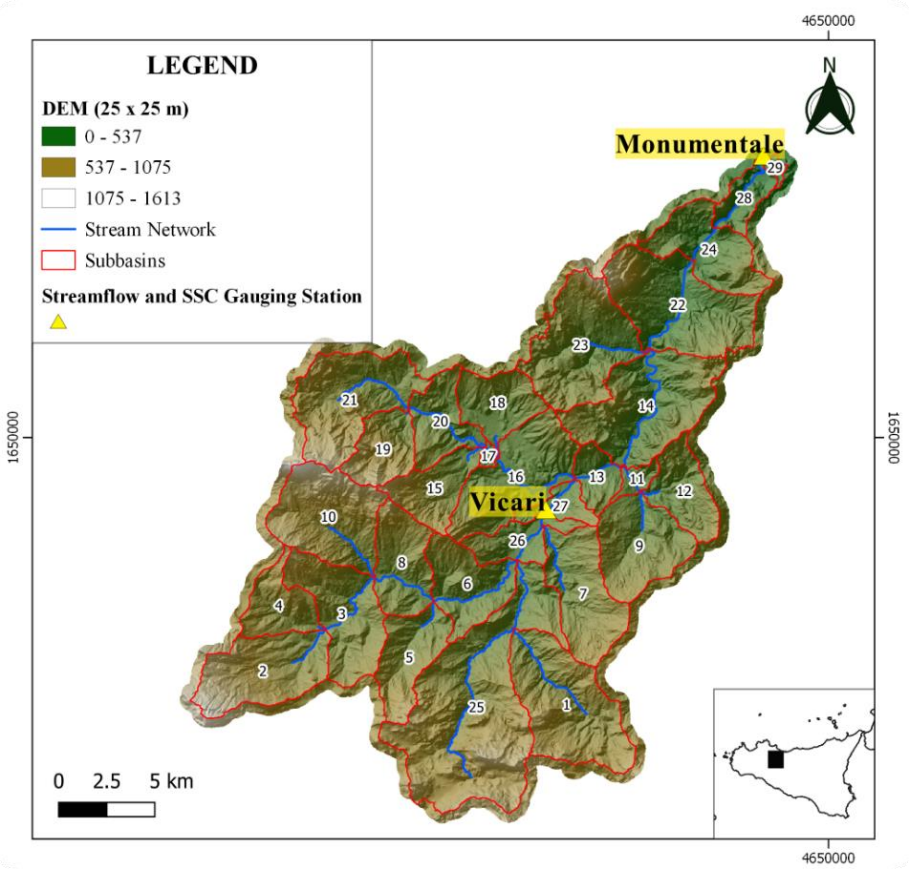

Figure 3.2.2 -The subdivision in subbasins obtained for the San Leonardo Basin

- SWAT HRU analysis

Each subbasin was then divided into hydrologic response units (HRUs), delineated portions distinguished by unique land use, management, and soil attributes. The underlying assumption in the

HRU concept is that there is no interaction among HRUs within a single subbasin. Loadings (runoff with sediment, nutrients, etc., transported by runoff) from each HRU are calculated separately and subsequently aggregated to determine the overall loadings for the subbasin. Adopting HRUs offers an advantage in enhancing the accuracy of loading prediction within the subbasin.

The key components that define the HRUs in the SWAT model are:

Land Use (LU): HRUs are defined based on land use categories, representing the specific vegetation type or land cover in each area.

Soil Type (ST): Different soil types have different hydrological properties, affecting water infiltration, runoff, and nutrient transport.

Slope (SL): Slope influences surface runoff and erosion potential. HRUs consider slope ranges to capture the impact of terrain gradients on hydrological processes.

Land Use Data

Land cover data was obtained from a land use map that was created between the late 1980s and early 1990s. The decision to use this map instead of the latest Corine map was made to ensure a representation of the land that was plausibly closer to the existing conditions during the period referenced by the flow and sediment data used for model calibration (from 1965 to 1987). The used map was generated at a 1:250000 regional scale through the photointerpretation of Landsat satellite imagery. The imagery comprised two series of Landsat satellite images captured in 1987 and 1988 during Spring (April-May) and Summer (June-August).

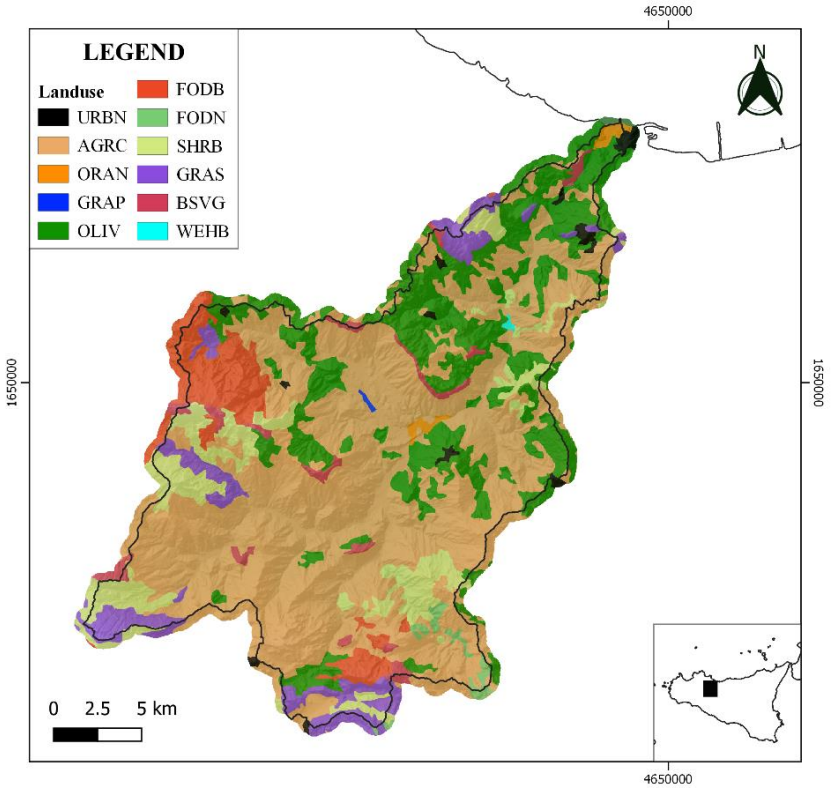

Figure 3.2.3 - Land Use Map used for the SWAT model

Each land type in this land cover map was associated with a standard land use category from the SWAT database (Figure 3.2.3). This plant growth database delineates growth parameters, defining plant development under ideal conditions and quantifying the impact of various stresses on plant growth.
The land cover classes were reassigned to align with the SWAT land cover classes (Figure 3.2.4 a), and a lookup table was generated to convert the numerical values present in the land use map into corresponding SWAT land use names. As illustrated in the doughnut plot of the image (Fig 3.2.4 b), the predominant land covers in the studied area include arable lands and complex cultivation patterns, followed by olive groves and association of shrub and/or herbaceous vegetation.

a)

CODE	LAND USES CLASSES	SWAT CODE	NAME
111	Continuous urban fabric	URBN	Residential
112	Discontinuous urban fabric		
133	Extractive areas		
211	Arable land irrigated and not, locally with tree crops; fodder; horticulture	AGRC	Agricultural Land-Close-grown
231	Complex cultivation patterns		
232	Association of annual crops		
221	Citrus grove	ORAN	Orange
222	Vineyard	GRAP	Vineyard
223	Olive grove	OLIV	Olives
311	Broadleaf trees	FODB	Deciduous needleleaf forest
314	Partially wooded land or degraded forest		
312	Coniferous	FODN	Deciduous broadleaf forest
321	Shrubland	SHRB	Shurbland
322	Grassland	GRAS	Grassland
323	Sparsely vegetated areas	BSVG	Baren or sparsly vegetated
331	Erosion scars, badlands, rock outcrops		
332	Wetlands	WEHB	

b)

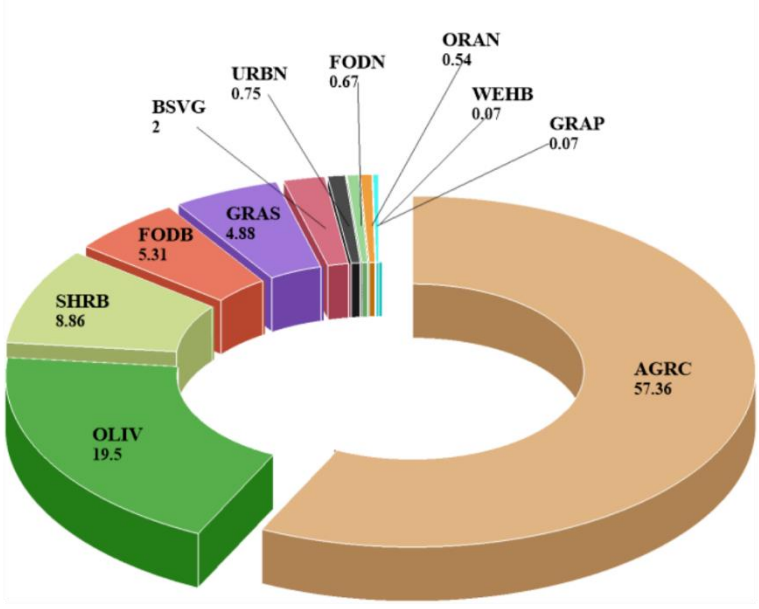

Figure 3.2.4 - a) Original Land Uses Classes and the associated SWAT Code; b) Percentual of Land Use in the studied area.

In order to evaluate the influence of human activities on the San Leonardo watershed, the land cover and water management practices were detailed. The HRU management file, which includes input data for planting, harvest, irrigation, nutrient and pesticide applications, and tillage operations, was modified, in particular the management activities for winter wheat cultivation were scheduled according to specific dates, as shown in the following table 3.2.1:

Crop	Date (day/month)	Management Operations
Winter Wheat	01 July	Harvest and kill operation
	12 Sept	Tillage operation (Generic Conservation Tillage)
	13 Sept	Tillage operation (Cultivator 1 Row)
	20 Sept	Plant/begin growing season
	29 Sept	Auto fertilization initialization
Olive	01 Jan	Plant/begin growing season
	1 Apr	Tillage operation (Cultivator 1 Row)
	1 Nov	Harvest only operation

Table 3.2.1 - Management operation changed for the San Leonardo watershed

Soil Data

Soils play a crucial role in hydrological modeling. Soil properties, including soil texture and hydraulic conductivity, impact infiltration and surface runoff, significantly influence the overall water balance within watersheds. The soil data used by SWAT can be divided into two groups: physical characteristics and chemical characteristics. The physical properties of the soil govern the movement of the water and air through the profile and significantly impact the water cycling within the HRU. While the physical properties are required, information on chemical properties is optional. It is well known that the SWAT hydrological model's accuracy depends on the input data; therefore, detailed local soil databases should be used if they are available. However, the lack of detailed soil information in Sicily led to the use of the open-source soil dataset. The variables included in the SWAT usersoil table are listed in Table 3.2.2, which also indicates the data source.

Variable Name	Definition	Data source	Resolution
HYDGRP	Soil hydrologic group (A, B, C or D)	HYSOg250m (Ross et al., 2018)	250 m
TEXTURE	Texture of soil water	Texture USDA Class - LUCAS 2018 (Ballabio et al., 2016)	500 m

SOL_BD	Moist bulk density (Mg/m^3 or g/cm^3)	bdod – SoilGrids 2.0 (Poggio et al., 2021)	250 m
SOL_AWC	Available water capacity of the soil layer (mm H_2O/mm soil)	EU - SoilHydroGrids ver1.0 (Tóth et al., 2017)	250m
SOL_K	Saturated hydraulic conductivity (mm/hr)	EU - SoilHydroGrids ver1.0 (Tóth et al., 2017)	250m
SOL_CBN	Organic carbon content (% soil weight)	SOC – SoilGrids 2.0 (Poggio et al., 2021)	250m
SOL_CLAY	Clay content (% soil weight)	clay – SoilGrids 2.0 (Poggio et al., 2021)	250m
SOL _SILT	Silt content (% soil weight)	silt – SoilGrids 2.0 (Poggio et al., 2021)	250m
SOL_SAND	Sand content (% total weight)	sand – SoilGrids 2.0 (Poggio et al., 2021)	250m
SOL_ROCK	Rock fragment content (% total weight)	cfv – SoilGrids 2.0 (Poggio et al., 2021)	250m
SOL_CBN	Organic carbon content (% soil weight)	soc - SoilGrids 2.0 (Poggio et al., 2021)	250m
SOL_ALB	Moist soil albedo	Surface Albedo – Copernicus Global Land Service (https://land.copernicus.eu/global/products/sa)	1 km
USLE_K	USLE equation soil erodibility factor (K) (units: 0.013 (metric ton m2 hr(/(m3-metric ton cm))	Soil Erodibility (K- Factor) – ESDAC (Panagos et al., 2014)	500 m
SOL_EC	Electrical conductivity (dS/m)	LUCAS SOIL 2018 (Orgiazzi et al., 2018)	500 m

Table 3.2.2 - Soil properties used in SWAT model

As reported in the Table 3.2.2, most of the soil properties that SWAT uses for the hydrological model have been taken from SoilGrids 2.0 database, currently the most detailed global soil properties dataset available at a medium spatial resolution (250-meter cell size). This dataset was created by incorporating soil profile observations from the ISRIC World Information Service (WoSIS) and environmental covariates describing vegetation, terrain morphology, climate, geology, and hydrology. The soil properties employed in SWAT include bulk density, organic carbon content, soil texture fractions, and the proportion of coarse fragments. These properties were modeled for six standard depth intervals: 0-5, 5-15, 15-30, 30-60, 60-100, and 100-200 cm. Built upon the soil information from SoilGrids250m, two datasets have also been employed: the multi-layered European Soil Hydraulic Database (EUSoilHydroGrids ver1.0) and the HYSOs250m dataset. The former contains soil hydraulic

properties, including field capacity (FC) and water content at the wilting point (WP), used to calculate Available Water Capacity of soil AWC, and saturated hydraulic conductivity (KS). The latter was used here to extrapolate information about hydrological soil groups. These are crucial components of the USDA curve-number method for estimating rainfall runoff. These groups categorize soils into four hydrologic soil groups to infer runoff potential. HSG-A has the lowest runoff potential (typically contains more than 90% sand and less than 10% clay), HSG-B has moderately low runoff potential (typically contains between 10 to 30% clay and 50 to 90% sand), HSG-C has moderately high runoff potential (typically contains more than 40% clay and less than 50% sand).

Due to computational constraints, executing SWAT for every individual soil property grid cell is not feasible. Instead, modelers often rely on digital soil property maps to establish their hydrological models. These digital soil property maps are composed of a spatial database of soil properties, which are represented by geographic information system layers. This approach was also adopted in this study, where the grid data representing soil properties were aggregated into spatial units with homogeneous properties. These spatial units were used to generate a digital soil property map for the basin. By employing this map, the spatial variability of soil physical properties was assessed and integrated into the hydrological model. In order to investigate the multivariate relationship among soil properties at various depths, Principal Component Analysis (PCA) on the correlation matrix involving standardized variables was conducted. Then Clustering was used to identify homogeneous zones. Fig 3.5 shows the overall process for developing the soil map, this analysis was executed using a script developed by David G. Rossiter, implemented on Google Earth Engine (https://www.css.cornell.edu/faculty/dgr2/_static/files/R_html/SoilGridsPCA.html#).

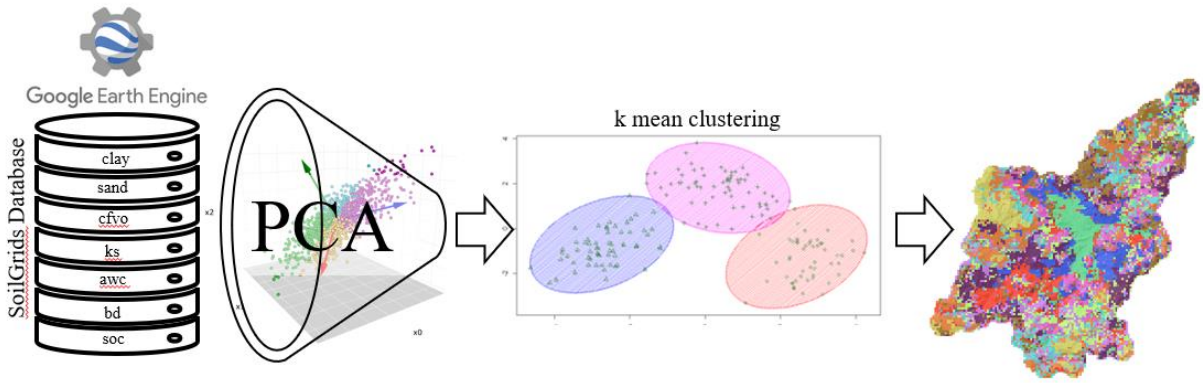

Figure 3.2.5 - Statistical process to create a digital soil map from soil properties data

In this analysis, various soil characteristics were used here to delineate zones with similar soil properties. These characteristics include clay and sand content, the presence of coarse fragments, saturated hydraulic conductivity, available water capacity, bulk density, and organic carbon concentration. Each of these characteristics has a resolution of 250 meters, and for each soil property, data were imported from four depth layers: 0-5 cm, 5-15 cm, 15-30 cm, and 30-60 cm. Therefore, there are a total of 28 layers. These layers were stacked into one multiband layer, where each band represents

a different soil property. Subsequently, to ensure uniformity across different property ranges and assign equal importance to all variables, the mean and standard deviation were computed for each band and converted to a constant image stack. The mean and standard deviation were finally used to standardize each band, subtracting the mean and dividing by sample standard deviation; this adjusts the values so that each band has a mean of 0 and a standard deviation of 1.

The original soil properties were then transformed using Principal Component Analysis (PCA) to capture certain patterns in the soil data.

PCA starts with the computation of the covariance matrix of the soil data that represents the relationships between different soil properties; then the eigen analysis is performed on the covariance matrix to extract eigenvalues and eigenvectors. In the eigen decomposition, the vector space made up of the original observations, which in this case are a stack of pixel values in a set of images, is projected onto another vector space. In this space, the new synthetic images, called principal components (PCs), are orthogonal to each other, i.e., completely uncorrelated. Eigenvalues represent the amount of variance explained by each principal component, when the synthetic images are arranged in decreasing order of variance explained, it was found that 14 principal components are needed to capture 95% of the variance of the standardized variables, these are the significant PCs. The resulting image is a multiband image, with each band corresponding to a different principal component, and the pixel values in each band indicate the contribution of that PC to the original data.

Each PC represents a distinct pattern of variation that exists in the soil property data. The pixel values in each band of the PC image quantify how similar that cell's soil is to the patterns described by these PCA. For example, suppose a particular pixel has a high value in the first band of the PC image. In that case, it suggests that the corresponding pattern of variation captured by the first PC is prominent at that location in the original soil property data. Conversely, low values in a specific PC band indicate less contribution of that pattern to the variability in the original soil properties at that location.

The PCs image obtained was subsequently analyzed with cluster analysis to group the observation that exhibit similar patterns. The aim of the cluster analysis is to create clusters such that members of each cluster are similar, and clusters are dissimilar, i.e., internally homogeneous, and externally heterogeneous. One commonly used centroid-based clustering method is *k-means*, which determines cluster centroids as the means of a group of objects. The choice of the number of clusters in k-means should reflect the desired level of detail; more clusters yield greater internal homogeneity but may lead to closely positioned classes.

In this work, the number of clusters was determined based on the expected number of soil associations derived from the Fierotti soil map published in 1967. Since the Fierotti soil map delineates 11 soil associations for the area under study, this number was chosen for the cluster analysis. A set of training pixels was established to construct the clusters, and the Manhattan distance between points in multivariate space was utilized to mitigate the influence of outlier values in the principal components

(PCs). Once the clusters were identified, they were used to classify the PC stack into an image with cluster numbers assigned to each pixel (Figure 3.2.6).

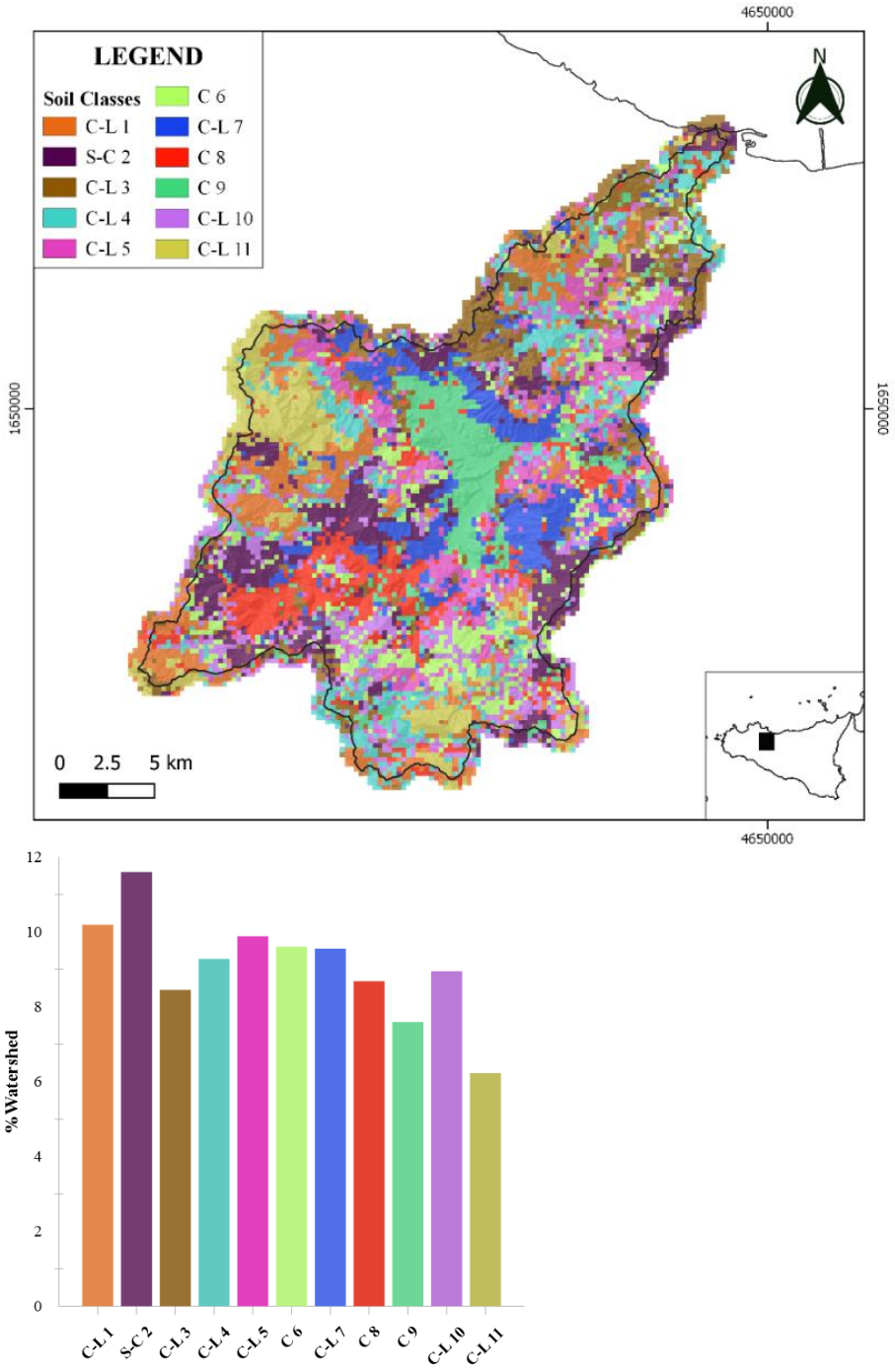

Figure 3.2.6 - Soil Map created for SWAT model and, in the bar plot, percentual of each cluster in the watershed

Finally, to validate the effectiveness of the clusters in representing different homogeneous zones in term of soil properties, the mean values for each of the soil characteristics inside each cluster were calculated, and the MANOVA test was performed. This test allows us to assess whether there are statistically significant differences in the mean values of soil properties among clusters.

The p-value obtained with the MANOVA test and shown in Figure 3.2.7 – a, is much smaller than the commonly used significance level; it implies that the difference in the mean values of soil properties among clusters are statistically significant, so the clusters represent distinct groups with varying soil properties. Then, the ANOVA test was performed to identify which variables contribute significantly to the observed differences among clusters. The p-values and boxplots (Figure 3.2. - b) indicate that rock fragments and silt play a greater role in separating the clusters.

MANOVA Results	*p*
	2.842e-14 ***

ANOVA Results

	F value	*p*
Clay	0.9018	0.5378
Silt	3.2749	0.002204**
Sand	1.0772	0.3953
Rock Fragment	13.889	8.40E-12***
Organic Carbon	0.0923	0.9998
Bul density	0.569	0.8319
Available Water Capacity	0.5118	0.8745
Saturated Hydraulic Conductivity	0.4277	0.9269

a)

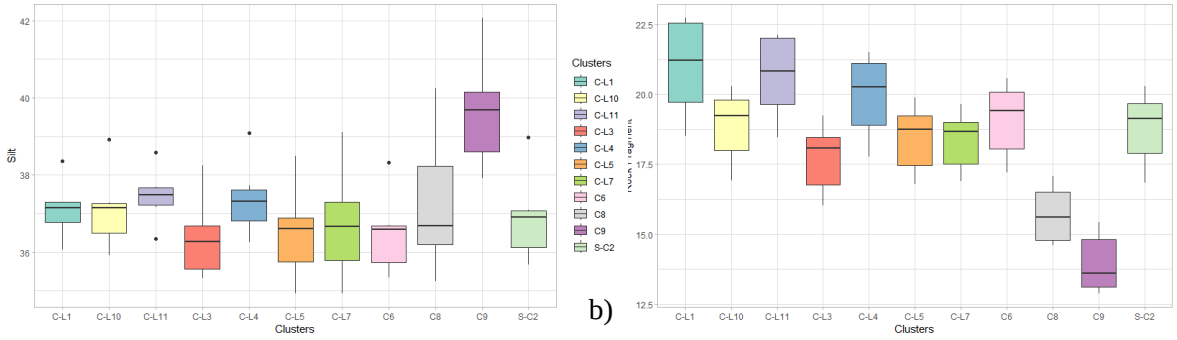

Figure 3.2.7 - a) The MANOVA results of the cluster analysis and ANOVA results of soil properties on each cluster; b) The distribution of silt and clay for each cluster.

Finally, by combining these three factors (Land Use, Soil Type, and Slope), 1577 HRUs were found. The HRUs provide a more detailed and accurate representation of the landscape's heterogeneity.

The SWAT model then simulates hydrological processes, such as runoff and sediment transport, separately for each HRU.

Climate data

SWAT requires daily records of precipitation, maximum and minimum air temperatures, solar radiation, wind speed, and relative humidity. These records are essential for providing the moisture and energy inputs that regulate the water balance and for determining the relative significance of various components within the hydrologic cycle. These data can be obtained either from observed data records or generated using a weather generator. For this study, precipitation and temperature data were sourced from 9 meteorological stations (managed by the Osservatorio delle Acque della Regione Siciliana) located inside the contributing catchment and covering the period from 1965 to 1987 (Table 3.2.3). Data

for the other variables, air humidity, wind velocity, and solar radiation, are unavailable for the same time period. Therefore, SWAT uses simulated data from observed monthly statistics extracted from the CFRS_World weather database. Figure 3.2.8 shows the location of the weather stations.

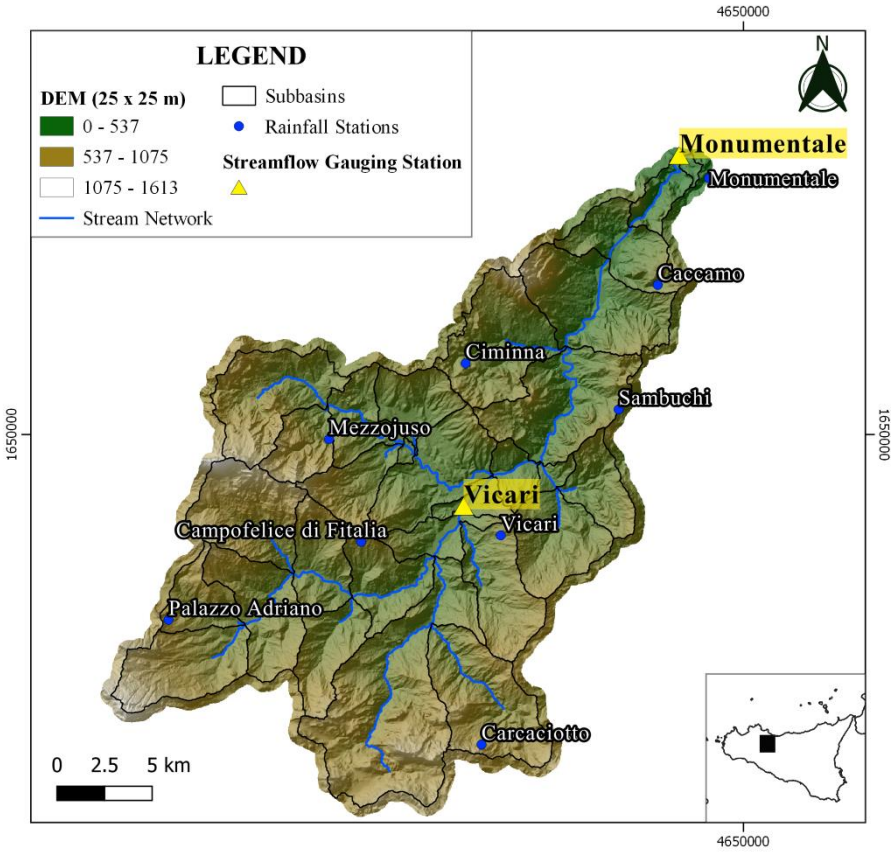

Figure 3.2.8 - Location of the meteorological station in the San Leonardo watershed

Weather Stations		Period covered
	Pcp Tmp Slr Wnd Hmd	'65 '66 '67 '68 '69 '70 '71 '72 '73 '74 '75 '76 '77 '78 '79 '80 '81 '82 '83 '84 '85 '86 '87
Vicari		
Mezzojuso		
Ciminna		
Palazzo Adriano		
Carcaciotto		
Campofelice		
Caccamo		
Monumentale		
Sambuchi		
	Osservatorio delle Acque Database	
	WGEN-CFSR-SICILY	

Table 3.2.3 - Period of operation of meteorological stations

The thermometric analysis relied solely on data collected from the Ciminna station. This station, situated within the San Leonardo Basin, was the only one equipped with a thermopluviograph. The climogram (Figure 3.2.9 a) constructed using the data from the study period revealed a relatively moderate temperature regime. The mean annual temperature across the entire territory was 15 °C. During the warmest months (July and August), average temperatures reached 24 °C, with maximum

peaks exceeding 40 °C. Conversely, the coldest months were January and February, with average temperatures of 8 °C. Minimum temperatures rarely dipped below 0 °C, with such occurrences restricted to higher elevations.

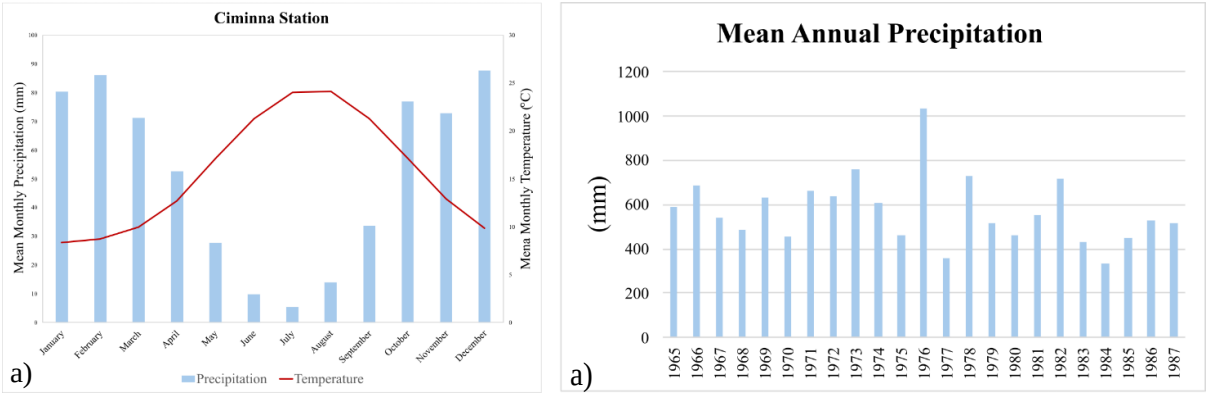

Figure 3.2.9 – a) Climogram and (b) precipitation analysis for the San Leonardo basin

Precipitation analysis was conducted for the studied period. The average annual rainfall (Figure 3.2.9 b) was approximately 600 mm. Interannual variability was observed, with 1976 and 1973 being the wettest years, recording 1032 mm and 757 mm, respectively. Conversely, 1984 was the driest year, receiving only 330 mm. November 1976 stands out as the wettest month during the study period, with 208 mm of precipitation.

In detail, the analysis of heat maps from meteorological stations (Figure 3.2.10 a and b) reveals the typical pattern of the Mediterranean climate, characterized by mild, humid winters and hot and dry summers. Additionally, precipitation is irregularly distributed throughout the year, with a higher concentration occurring over a few days between September and March. Examining the cumulative monthly precipitation values, the highest value of 330 mm was recorded in November 1976 at the Palazzo Adriano station.

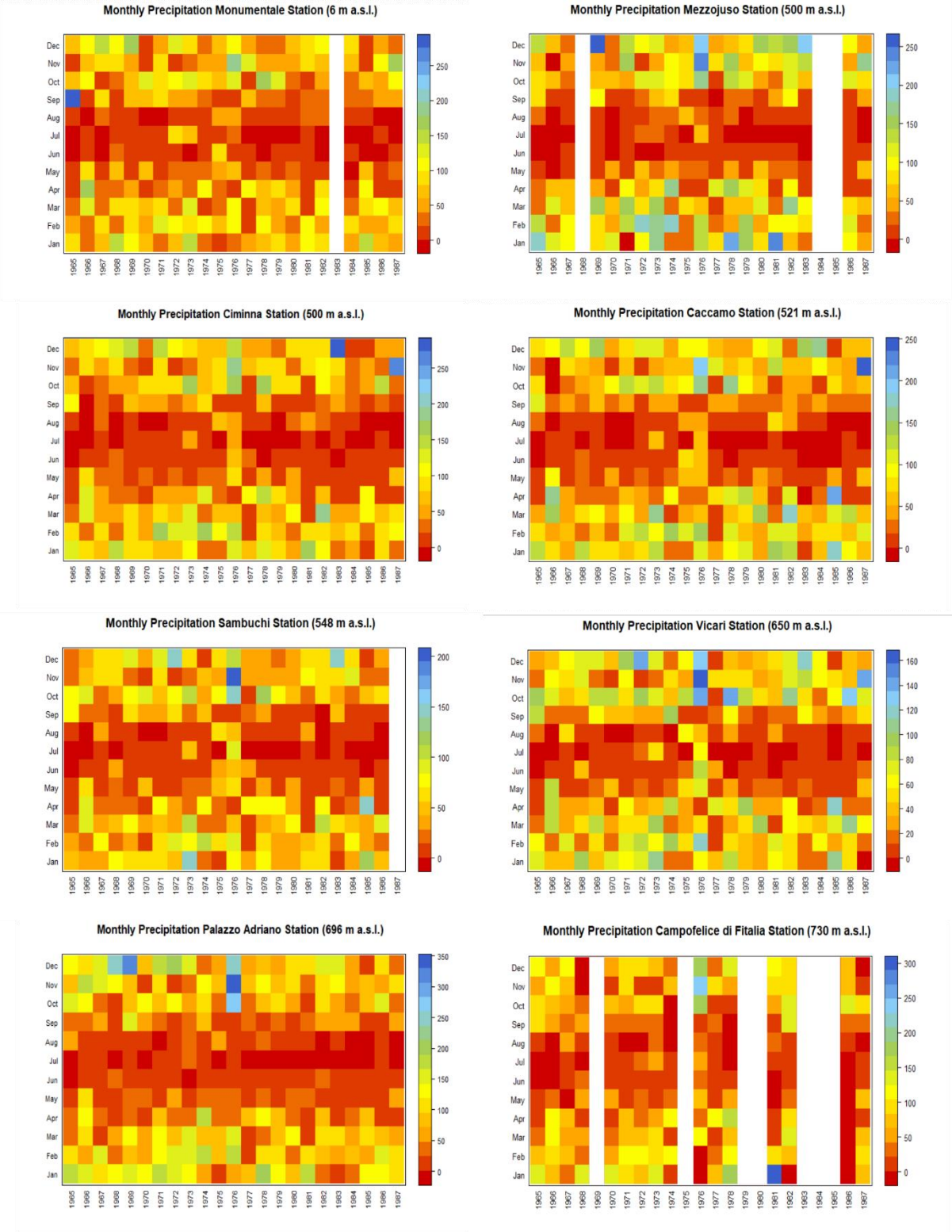

Figure 3.2.10 a) - Heatmaps for all the meteorological stations inside the studied watershed

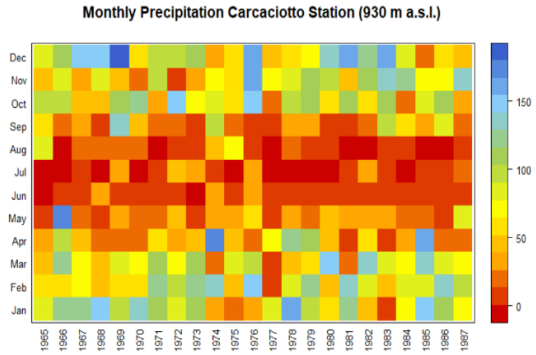

Figure 3.2.10 b) - Heatmaps for all the meteorological stations inside the studied watershed

Analysis of annual cumulative precipitation across all stations revealed 1976 as a significant outlier. This year exhibited a substantial deviation from the precipitation patterns observed in other years.

Discharge and Sediment data

Monthly discharge and sediment transport records obtained from the Vicari and S. Leonardo Monumentale gauging stations were used for model calibration and validation. The S. Leonardo Monumentale station's hydrometer is located 0.9 kilometers from the estuary at an elevation of 1.5 meters above sea level. Its contributing area is approximately 498 km². Conversely, the Vicari station's hydrometer is situated 30 kilometers from the estuary at an altitude of 250 meters above sea level, with a contributing area of 245 km².

The operational period of both liquid and solid flow recording stations spans from 1965 to 1972, with differing operational periods between the two stations. Furthermore, the Vicari station has missing data for two years, specifically 1983 and 1984, as delineated in the subsequent Table 3.2.4:

		‘65	‘66	‘67	‘68	‘69	‘70	‘71	‘72	‘73	‘74	‘75	‘76	‘77	‘78	’79	‘80	‘81	‘82	‘83	‘84	‘85	‘86	‘87
Stream Flow	Monumentale	■	■	■	■	■	■	■	■	■	■	■	■	■	■	■	■							
	Vicari								■	■	■	■	■	■	■	■	■	■	■	■	■	■	■	■
Sediment	Monumentale	■	■	■	■	■	■	■	■	■	■	■	■	■	■	■	■							
	Vicari								■	■	■	■	■	■	■	■	■	■	■			■	■	■

Table 3.2.4 - Period of operation for streamflow and suspended sediment concentration gauges in San Leonardo Basin.

The boxplot analysis of flow rate was conducted to investigate the variation in flow values across different months. The results indicate that the months between December and April exhibit the highest average flow values. In particular, February shows the highest average discharge.

Furthermore, the analysis of maximum discharges for the entire period of both stations reveals that the most extreme flow event occurred in December 1976 (Figure 3.2.11). During this month, the Monumentale Station recorded a maximum discharge of 1014 m³/s, while the Vicari Station recorded a maximum discharge of 420 m³/s. These values represent the most significant flow events recorded at each station during their operational periods.

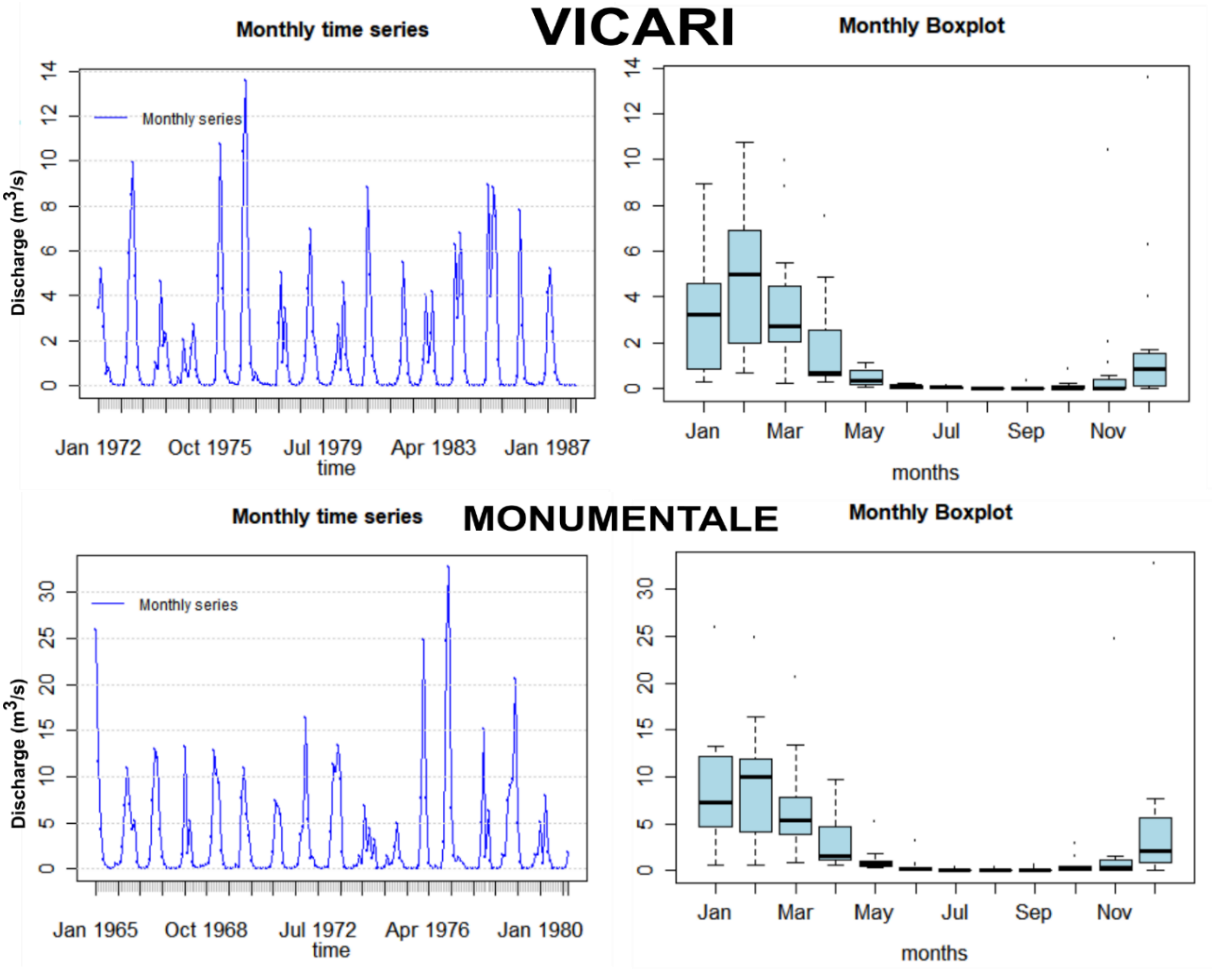

Figure 3.2.11 – Time series plot and boxplots of discharge values for both gauge stations

The suspended sediment yield analysis (Figure 3.12) revealed some interesting patterns. Firstly, the monthly mean values of the Monumentale Station, which was operational from 1965 to 1980, show that January and December have the highest average sediment transport values. On the other hand, August exhibits minimal sediment transport, with values that are almost negligible.

A similar pattern is observed in Vicari Station, which was operational from 1972 to 1987. Once again, January emerges as the month with the highest average sediment transport values. In contrast, August also experiences the lowest sediment transport values at this station.

Looking at the maximum values, these were recorded at both stations in December 1976, with a staggering value of 1,280,000 tons for the Monumentale Station and 13,100 tons for the Vicari Station. These events represent the most extreme sediment transport events recorded at each station during their respective operational periods.

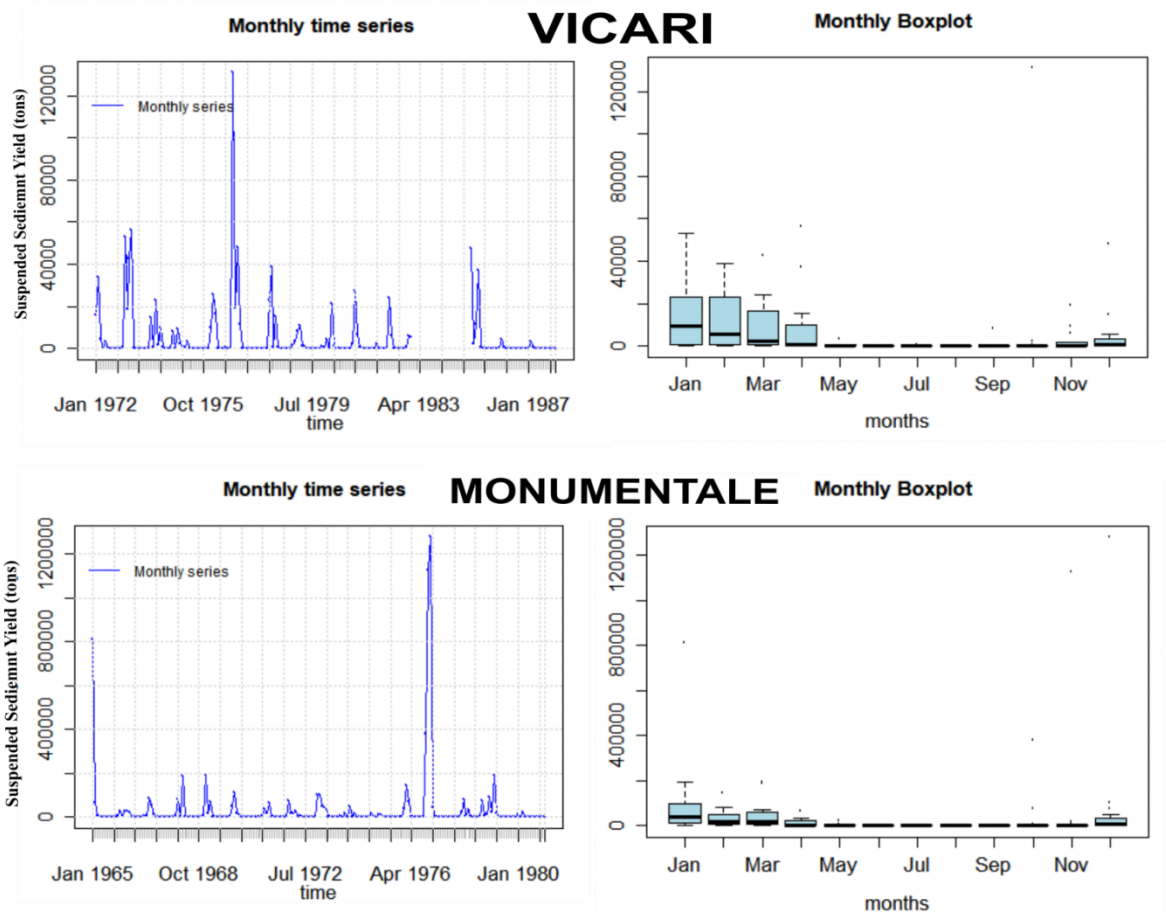

Figure 3.2.12 – Time Series plot and boxplots of Suspended Sediment Yield (SSY) values for both gauge stations

3.2.3 Calibration and Validation

The sensitivity analysis and calibration of the SWAT model are crucial steps in ensuring the accuracy and reliability of its predictions. During sensitivity analysis, it is explored how changes in input parameters affect the output predictions; the aim is to find an optimum set of parameters to represent all relevant hydrological processes while avoiding over-parametrization, which is one of the main sources of errors in the simulated results. The SWAT model contains more than 210 hydrological parameters. All of them do not significantly contribute to the output. Therefore, it is important to identify the most sensitive input parameters that significantly impact the model's output, allowing researchers to rank their calibration efforts (Arnold et al., 2012). Different sensitivity analysis techniques can be used, these techniques can broadly be categorized into two groups: local sensitivity analysis, which involves changing values one at a time, and global sensitivity analysis, which allows all parameter values to vary simultaneously.

Then, during the calibration process, different values for input parameters are tested to find the combination that produces simulated values closest to the observed data. This iterative process involves adjusting parameter values within reasonable ranges to fine-tune the model's performance (Moriasi, 2015). Multiple processes will be affected by many parameters due to the comprehensive nature of SWAT, which simulates process interactions. Surface runoff is directly impacted by CN, but as it

changes, all components of the hydrology balance change. Soil erosion and nutrient transport are also directly impacted by surface runoff. This is the primary reason why most of the manual calibration methods starts with the hydrology balance and streamflow, then move to sediment.

Examining the accuracy of output and process simulation is part of calibration to ensure that the model adequately captures the complex interactions and dynamics within the watershed.

Model performance is evaluated by qualitative and quantitative methods. The qualitative procedure consists of visually comparing the observed and simulated values in data-display graphics.

The quantitative methods that evaluate model performance are classified into two main groups: standard regression and dimensionless regression. Standard regression statistics evaluate the strength of the linear relationship between simulated and measured data while dimensionless techniques offer a relative assessment of model performance (N. Moriasi et al., 2007). Techniques used in standard regression methods include slope and y-intercept, Pearson's correlation (r), and coefficient of determination (R^2)

The slope and y-intercept of the best fit regression line can indicate how well simulated data match measured data. The slope reveals the relative relationship between simulated and measured values, while the y-intercept indicates any lag or lead between model predictions and measured data. A slope of 1 and y intercept of 0 suggest that the model accurately reproduces the magnitudes of measured data. However, it's important to note that these analyses are typically conducted under the assumption of a linear relationship between measured and simulated values, implying that all error variance resides in simulated values and that measured data are devoid of errors. Measured data is not always error-free, so it's important to be cautious when using regression statistics for model evaluation. Pearson's correlation coefficient and coefficient of determination describe the degree of collinearity between simulated and measured data. The correlation coefficient r, which ranges from -1 to 1, is an index of the degree of linear relationship between observed and simulated data. If the Pearson correlation coefficient is near +1 or -1, it indicates a strong correlation, while if it is near 0 it indicates a weak or no correlation.

$$r = \frac{\sum_{i=0}^{n}(O_i - \bar{O})\,(P_i - \bar{P})}{\sqrt{\sum_{i=0}^{n}(O_i - \bar{O})^2}\,\sqrt{\sum_{i=1}^{n}(P_i - \bar{P})^2}}$$

Where:

O_i is the *i*th observation data.

P_i is the *i*th simulated value.

$\bar{O}$ is the average of the observed data.

$\bar{P}$ is the average of the simulated data.

A limitation of the Pearson correlation coefficient is that it is sensitive to outliers and can be influenced by extreme values in the data. Moreover, the Pearson correlation measures only linear relationships between variables; hydrological processes often exhibit nonlinear behavior, especially during extreme

events such as floods or droughts. The Pearson correlation coefficient may fail to capture these nonlinear relationships, leading to underestimation or overestimation of the model performance.

Similarly, R^2 quantitatively measures how well the hydrological model fits the observed data. It indicates the proportion of the variance in the dependent variable (e.g., observed) that is explained by the independent variables (e.g., model predictions). R^2 ranges from 0 to 1, where 1 indicates a perfect fit between the model and observed data and 0 indicates no relationship; typically, values greater than 0.5 are considered acceptable.

$$R^2 = \left[\frac{\sum_{i=0}^{n}(O_i - \bar{O})\,(P_i - \bar{P})}{\sqrt{\sum_{i=0}^{n}(O_i - \bar{O})^2}\,\sqrt{\sum_{i=1}^{n}(P_i - \bar{P})^2}} \right]^2$$

Where:

O_i is the *i*th observation data.

P_i is the *i*th simulated value.

$\bar{O}$ is the average of the observed data.

$\bar{P}$ is the average of the simulated data.

R-squared(R^2) is limited by its tendency to increase with model complexity, even when the added complexity improves the model's predictive capability. Moreover, R-squared fails to distinguish between systematic and random errors in model predictions. If the model consistently overestimates or underestimates observed values, it's not certain that elevated R-squared values indicate accurate predictions. Furthermore, the validity of R-squared as an indicator of model performance is determined by the quality and representativeness of the observed data. The interpretation of R-squared may be misleading if observations are inaccurate or biased.

Regarding the dimensionless methods, one of the most used is the Nash-Sutcliffe efficiency (NSE):

$$NSE = 1 - \frac{\sum_{i=1}^{n}(O_i - P_i)^2}{\sum_{i=1}^{n}(O_i - \bar{O})^2}$$

Where:

O_i is the *i*th observation data.

P_i is the *i*th simulated value.

$\bar{O}$ is the average of the observed data.

Nash-Sutcliffe efficiency (NSE) is a normalized statistic that evaluates the relative magnitude of the residual variance ('noise') compared to the variance of the measured variance ('information'). NSE indicates how well the plot of observed versus simulated data fits the 1:1 line. NSE range between - ∞ and 1, where NSE= 1 represents optimal performance. Values between 0 and 1 are generally considered acceptable performance levels, whereas values less than or equal to 0 indicate that the mean observed value is a better predictor than the simulated value, reflecting unacceptable performance (N. Moriasi et

al., 2007). NSE is particularly useful because it accounts for both the mean and the variability of the observed data, offering a comprehensive evaluation of model performance and making it less sensitive to outliers. Due to its versatility in assessing various output responses (e.g., stream flow, sediments, nutrients), extensive information on reported NSE values is available for comparison. NSE has a few limitations, including its inability to identify model bias or differences in timing and magnitude of peak flow or recession curve shapes, which make it unsuitable for single-event simulations.

The recommended performance evaluation criteria for statistical metrics such as R-squared (R^2) and Nash-Sutcliffe Efficiency (NSE) for various spatial and temporal scales are outlined by Moriasi (2015) and tabulated in Table 3.2.3. These criteria are based on synthesizing earlier benchmarks reported in the literature. According to this table, for watershed-scale models, model performance can be deemed satisfactory for flow simulations on a daily/monthly or annual scale if R2 exceeds 0.60 and NSE surpasses 0.5; for sediment data, simulation model performance is satisfactory if R^2 exceeds 0.4 and NSE 0.45.

Output Response	Measure	Temporal Scale	Very Good	Good	Satisfactory	Non Satisfactory
FLOW	R^2	D-M-A	$R^2 > 0.85$	$0.75 < R^2 \leq 0.85$	$0.6 < R^2 \leq 0.75$	$R^2 \leq 0.6$
	NSE	M	NSE > 0.80	$0.70 < NSE \leq 0.80$	$0.5 < NSE \leq 0.70$	$NSE \leq 0.5$
SEDIMENT	R^2	D-M-A	$R^2 > 0.80$	$0.65 < R^2 \leq 0.80$	$0.4 < R^2 \leq 0.65$	$R^2 \leq 0.4$
	NSE	M	NSE > 0.80	$0.70 < NSE \leq 0.80$	$0.45 < NSE \leq 0.70$	$NSE \leq 0.45$

Table 3.2.3 - Final performance evaluation criteria for recommended statistical performance measures.

Modelers can benefit from the graphical performance figures as a complementary tool in supporting calibration and validation. They allow visual comparison of simulated and measured output response data, help identify model bias, identify differences in timing and magnitude of peaks (e.g., peak flows) and shape of recession curves, incorporate measurement and model uncertainty, and illustrate how well the model reproduces the frequency of measured daily/monthly values. One commonly employed graphical method is the hydrograph, which presents a time series representation of predicted and observed flow across the calibration and validation periods.

The final step is the validation of the component of interest. The process of model validation involves proving that a given site-specific model can perform simulations with sufficient accuracy. Validation involves carrying out a model with the parameters determined during the calibration process and comparing it to observed data that was not used during the calibration process. The calibration step ensures the model can generalize well to new conditions and accurately simulate hydrological processes beyond the calibration period.

The calibration procedure shown in Figure 3.2.13 was followed for this work. First, the model was simulated from 1965 to 1987, the entire period during which data were available from the two monitoring stations. The first three years of the warm-up period (1965-1967) were assigned in the model to initialize model parameters.

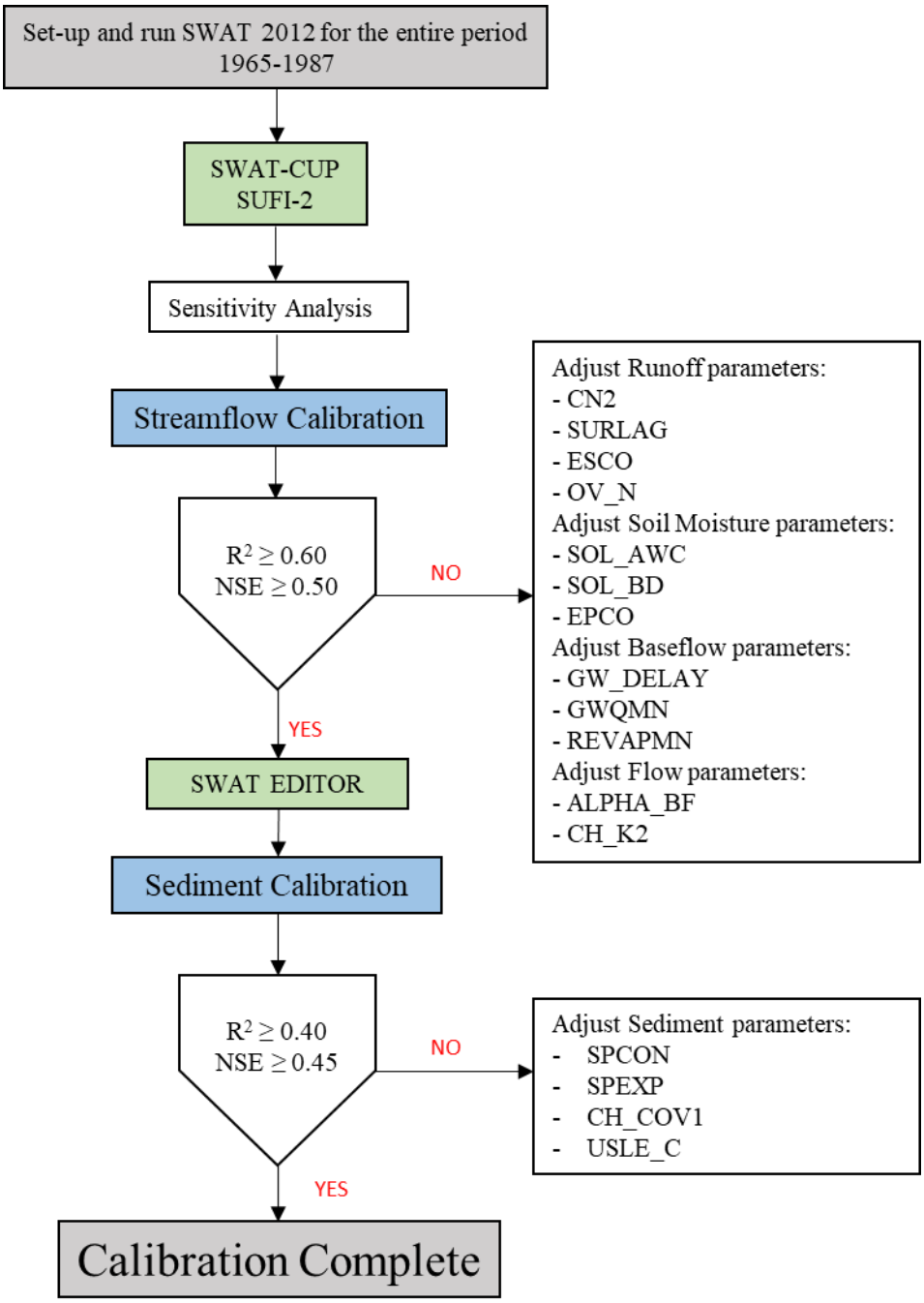

Figure 3.2.13 – Calibration procedure used in this work

The sensitivity analysis regarding the flow out was done using SWAT Calibration and Uncertainty Procedure (SWAT-CUP), where the sequential Uncertainty Fitting (SUFI-2) optimization algorithm was used for the uncertainty analysis. This method is based on the Bayesian framework, which uses probability to deal with uncertainty. In SUFI-2 the uncertainties of the parameters mainly include three aspects:

- The large amount of observational information, including precipitation, temperature, relative humidity, and soil database, often results in measurement and systematic errors, resulting in uncertainty in the input datasets.
- The hydrological model is a simplified representation of the real world, which can cause model uncertainty. This means it may not capture every detail perfectly. Simplifications and assumptions made in the model introduce uncertainty.
- The uncertainty of model parameters mainly includes parameters that control watershed attributes and hydrological processes, as these parameters are often difficult to measure directly.

SUFI-2 uses Latin Hypercube Sampling (LHS) to account for these uncertainties. This is a stratified sampling technique, which requires approximate random sampling from the multi-parameter distribution to ensure that the sample structure is similar to the overall structure, thereby improving the accuracy of the estimation. SWAT-CUP generates a range of model outputs for each simulation by running the model with different parameter combinations. This collection represents possible outcomes depending on the uncertainty in the model parameters. Instead of a single signal representing model output, SWAT-CUP considers an envelope of good solutions represented by the 95 percent prediction uncertainty (PPU) generated by specific parameter ranges.

The objective is to modify the model parameters such that most of the measured data in the natural system falls within this range known as 95% prediction uncertainty (95PPU) of the model. The 95PPU is calculated at the 2.5% and 97.5% levels of the cumulative distribution of output variables obtained through the Latin Hypercube Sampling method.

In the sensitivity analysis, 18 parameters (refer to Table 3.2.4) governing various hydrological processes were chosen, drawing from previous literature, for global sensitivity analysis.

Parameter Name	Definition	Process	Adjustment	Initial Range
ALPHA_BF.gw	Baseflow alpha factor (1/days).	Groundwater	2	0 - 1
GW_DELAY.gw	Groundwater delay time (days).	Groundwater	2	0 - 500
GW_REVAP.gw	Groundwater re-evaporation coefficient (mm H_2O).	Groundwater	2	0.02 - 0.2
GWQMN.gw	Threshold depth of water in the shallow aquifer required for return flow to occur (mm H_2O).	Groundwater	2	0 - 5000
REVAPMN.gw	Threshold depth of water in the shallow aquifer for “revap” or percolation to the deep aquifer to occur (mm H_2O).	Groundwater	2	0 - 500
RCHRG_DP	Deep aquifer percolation fraction.	Groundwater	2	0 - 1
CH_K2.rte	Effective hydraulic conductivity in main channel alluvium (mm/hr).	Channel routing	2	-0.05 - 500
CH_N2.rte	Manning's "n" value for the main channel.	Channel routing	2	-0.01 - 0.3
SURLAG.bsn	Surface Runoff lag coefficient.	Surface Runoff	2	0.05 - 24
ESCO.bsn	Soil evaporation compensation factor	Evaporation	2	0 - 1
EPCO.bsn	Plant uptake compensation factor.	Evaporation	2	0 - 1
CANMX.hru	Maximum canopy storage (mm H_20).	Evapotranspiration	2	0 - 100
OV_N.hru	Manning's "n" value for overland flow.	Overland flow	2	0.01 - 1
LAT_TTIME.hru	Lateral flow travel time (days).	Soil Water	2	0 - 180
CN2.mgt	Curve number for moisture condition II.	Surface Runoff	3	-0.3 - 0.3
SOL_K().sol	Saturated hydraulic conductivity (mm/hr).	Soil Water	3	-0.3 - 0.3
SOL_BD().sol	Moist bulk density (Mg/m^3)	Soil Water	3	-0.3 - 0.3
SOL_AWC().sol	Available water capacity of the soil layer (mmH_2O/mm soil)	Soil Water	3	-0.3 - 0.3

Table 3.2.4 Parameters chosen for the calibration of discharge.

A total of 250 simulations were executed using SUFI-2. The sensitivity of parameters in SUFI-2 is estimated by solving multiple regressions, which regresses the parameters produced by Latin Hypercube against the value of the objective function. Multiple regression method is considered as:

$$g = a + \sum_{i=1}^{m} \beta_i \, b_i$$

where g is the objective function, b is a parameter, α is a regression constant, β corresponds to the technical coefficient attached to the variable b that tells how much each parameter affects the objective function, and m is equal to the number of parameters (Singh and Jha, 2021). The t-test is then used to identify the relative significance of each parameter b_i, this test helps determine if a parameter has a meaningful impact on the objective function. The t-stat is calculated by dividing the coefficient of a parameter by its standard error. It is a measure of the precision with which the regression coefficient is measured. A large coefficient relative to its standard error suggests that the parameter differs significantly from 0, indicating its sensitivity. The p-value then helps to determine the results are statistically significant. Each term's p-value tests the null hypothesis that the coefficient equals zero, implying no effect. A low p-value (< 0.05) suggests rejecting the null hypothesis. A predictor with a low p-value is likely to be a valuable addition to the model because the value of the predictor is linked to the response variable. Conversely, a larger p-value suggests that changes in the predictor are not associated with changes in the response so the parameter is not very sensitive. Typically, a p-value < 0.05 indicates to reject the null hypothesis (i.e., the coefficient of that parameter is different from 0) indicating a 95% confidence level that the parameter's effect is real.

The model was ranked by sensitivity analysis from highest to lowest for parameters based on their sensitivity. Parameters with the highest rank were adjusted initially, followed by the adjustment of others. Calibration was not performed on parameters that had only a minor impact on the output.

The sensitivity analysis was carried out for model parameters for both stations; the results are shown in Figure 3.2.15. The most sensitive parameter is the baseflow alpha factor (APLHA_BF, 1/days), a direct index of groundwater flow response to changes in recharge.

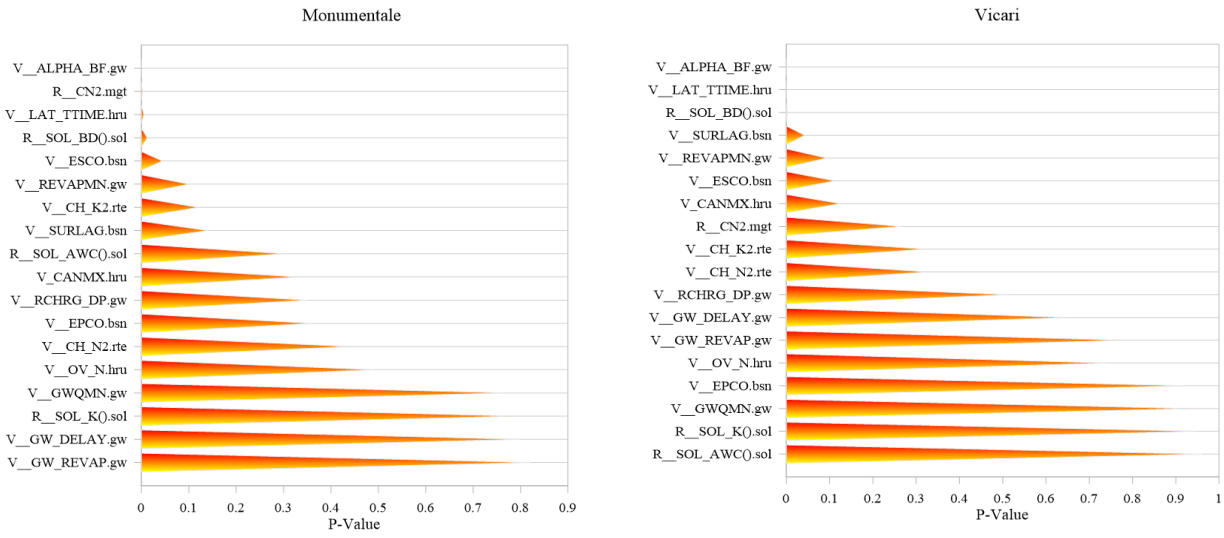

Figure 3.2.15 - Results of the sensitivity analysis for both the station

After sensitivity analysis, calibration and validation were performed by splitting the available observed data into two datasets: one for calibration and another for validation (Fig. 3.2.16). Data has been splitted by time periods, carefully ensuring that the climate data used for both calibration and validation are not substantially different, i.e., wet moderate, and dry years occur in both periods. Finally, based on the flowchart from the previous figure, three scenarios were examined (Fig. 3.2.16). Calibration and validation in Scenario 1 were solely focused on the liquid flow rate. In contrast, sediment discharge calibration and validation were conducted in Scenario 2 and Scenario 3; in the latter, the year 1976 was omitted from the analysis to see if its anomalous behavior could change the model's performance.

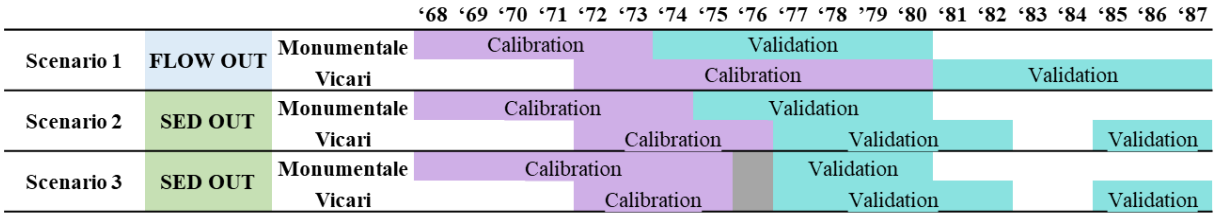

Figure 3.2.16 Three different scenarios used for this work

3.2.4 Results and Discussion

In the calibration process, the number of parameters was reduced by considering only those that showed a p-value lower than 0.5, indicating higher sensitivity. The initial set of 18 parameters was reduced to 12 for the Vicari Station and 11 for the Monumentale Station in the final calibration phase. This approach allowed for the selection of the most sensitive parameters, thereby improving the accuracy and reliability of the model.

Scenario 1

For the Vicari Station, the optimal statistical parameter values for the calibration of flow out were achieved in the fourth iteration and simulation n. 166. For the Monumentale Station, these values were

obtained in the third iteration and simulation n. 63. The best-fit parameter values are presented in the following tables:

Vicari (1972-1980)	
Parameter	*Calibrated Value*
CN2.mgt	75.8 – 85.3
SOL_BD(..).sol	1.18 -1.64
OV_N.hru	0.45
SURLAG.bsn	28.34
LAT_TTIME.hru	17.54
ALPHA_BF.gw	0.7
REVAPMN.gw	44.72
CH_K2.rte	120.42
CANMX.hru	87.68
GW_DELAY.gw	5.4
GWQMN.gw	1268.6
EPCO.bsn	0.92

Monumentale (1968 – 1973)	
Parameter	*Calibrated Value*
CN2.mgt	73.15 - 82
SOL_BD(..).sol	1.15 – 1.6
OV_N.hru	0.751
SURLAG.bsn	6.17
LAT_TTIME.hru	9.88
ALPHA_BF.gw	0.46
REVAPMN.gw	347.14
CH_K2.rte	203.98
RCHRG_DP.gw	0.016
CH_N2.rte	0.091
ESCO.bsn	0.74

Table 3.2.5 – The best-fit values obtained after the calibration of the streamflow

The parameters that were calibrated are related to different processes. Specifically, the initial SCS runoff curve number for moisture condition II (CN2), moist bulk density (SOL_BD), surface runoff lag coefficient (SURLAG), and the Manning's roughness coefficient are related to surface runoff generation. In particular, the SURLAG parameter in the SWAT model determines the fraction of surface runoff that will reach the main channel on the same day it is generated. This parameter is particularly important for large subbasins where the concentration time is greater than 1 day, meaning it takes more than a day for the water to flow from the farthest point of the subbasin to the main channel. When the value of SURLAG decreases, more water is stored instead of being released immediately, which delays the surface runoff reaching the main channel. This delay can help smooth out the simulated streamflow hydrograph, making it less peaky and more evenly distributed over time. As shown in Table 3.2.5, the calibrated values of SURLAG for Vicari and Monumentale are different, respectively 28.34 and 6.17. The difference can be attributed to the fact that the two contributing areas are different, leading to different times of concentration. Monumentale has a greater time of concentration than Vicari, which means it holds more water in storage. As a result, the fraction of surface runoff storage reaching the stream will be lower, and the delay will be greater.

The time of concentration also controls the lag in which the lateral flow is released to the main channel. In a large contributing area with a time of concentration greater than 1 day, only a portion of the lateral flow will reach the main channel on the day it is generated. Also, in this case, the Monumentale value is lower than Vicari. This difference could be related to the fact that increasing the time of concentration increases the lateral flow travel time and so decreases the fraction of lateral flow storage reaching the stream.

Other parameters subject to calibration in SWAT CUP have been those related to the groundwater processes. Water moves to the lowest depth of the soil profile by percolation or bypass flow through the vadose zone before becoming shallow and/or deep aquifer recharge. The lag between when water leaves the soil profile and goes into the shallow aquifer will be influenced by the depth of the water table and the hydraulic properties of the geologic formations in the vadose and groundwater zones. SWAT model accounts for the time delay in aquifer recharge once the water exits the soil profile with the parameter GW_DELAY.

Conversely, water can move from the shallow aquifer into the overlying unsaturated zone under certain conditions. Specifically, during periods when the material overlying the aquifer is dry, water in the capillary fringe that separates the saturated and unsaturated zones can evaporate and move upward. As water is removed from the capillary fringe through evaporation, it is replaced by water from the underlying aquifer. Additionally, deep-rooted plants can remove water directly from the aquifer, further contributing to water movement from the aquifer to the unsaturated zone.

SWAT models the movement of water into overlying unsaturated layers as a function of water demand for evapotranspiration. This process, called “revap, " is significant in watersheds where the saturated zone is not far below the surface or deep-rooted plants are growing. Because the type of plant cover will affect the importance of revap in the water balance, the parameters governing revap are usually varied by land use. Revap is allowed to occur only if the amount of water stored in the shallow aquifer exceeds a threshold value, called REVAPMN, specified by the user.

The shallow aquifer provides a steady flow of water to the main channel or stream in a watershed. This continuous flow, known as base flow, is only released into the stream when the water stored in the shallow aquifer exceeds a certain limit, which is specified by the user and referred to as GWQMN.

When a stream does not receive any groundwater contributions, water can be lost from the channel through transmission losses, which occur via the side and bottom of the channel. The estimation of transmission losses is based on an equation that utilizes the effective hydraulic conductivity of the channel alluvium (mm/hr) as a parameter, denoted as CH_K2. For both simulations, Vicari and Monumentale, the value of CH_K2 is higher than 125 mm/hr, indicating a high loss rate for the bed material. This could be attributed to the presence of very clean gravel and large sand, which are highly permeable materials. The high transmission losses suggest that a significant amount of water is being lost from the channel, which could affect the water balance in the watershed.

The baseflow recession constant, ALPHA_BF, indicates how quickly groundwater responds to changes in water recharge. In areas where groundwater reacts slowly to recharge, the recession constant typically ranges from 0.1 to 0.3. On the other hand, regions with rapid groundwater response may have recession constant values between 0.9 and 1.0. The value obtained during the calibration is different for Vicari and Monumentale, respectively 0.7 and 0.46.

Finally, the two calibrated parameters are related to the evapotranspiration process. One of these parameters CANM represents the maximum amount of water the canopy can hold when fully

developed. This parameter is crucial because it determines the limit on the amount of water the canopy can capture and retain before it evaporates or drips down to the ground. Instead, the ESCO parameter is associated with soil water evaporation. The SWAT model calculates the evaporative demand for each soil layer by subtracting the evaporative demand at the bottom of the layer from the demand at the top. However, SWAT does not allow a different layer to compensate for the inability of another layer to meet its evaporative demand, which can result in a reduction in actual evapotranspiration for the area. The ESCO has been added to permit the user to adjust the distribution of evaporative demand across the soil layers. Decreased ESCO value can increase the model's ability to draw more evaporative demand from deep soil layers.

Fig 3.2.17 a and b show the graphical results of streamflow simulation performance during the calibration and validation periods. The statistical performance of monthly streamflow simulation in Vicari Simulation is in a good range during calibration but only satisfactory during validation. On the other hand, for the Monumentale simulation, the statistical performance is within an acceptable range for both the simulation and calibration phases.

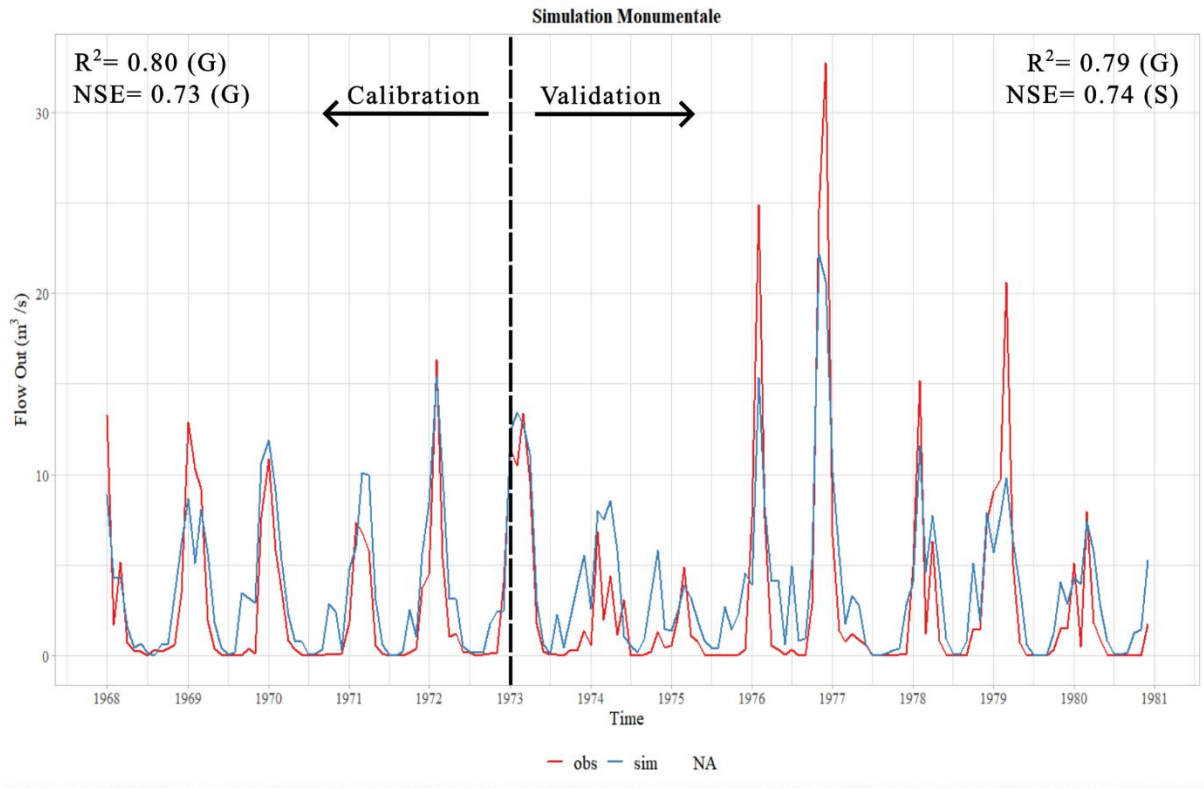

Figure 3.2.17 a) - Comparison between observed and simulated streamflow for scenario 1 in the Monumentale Station

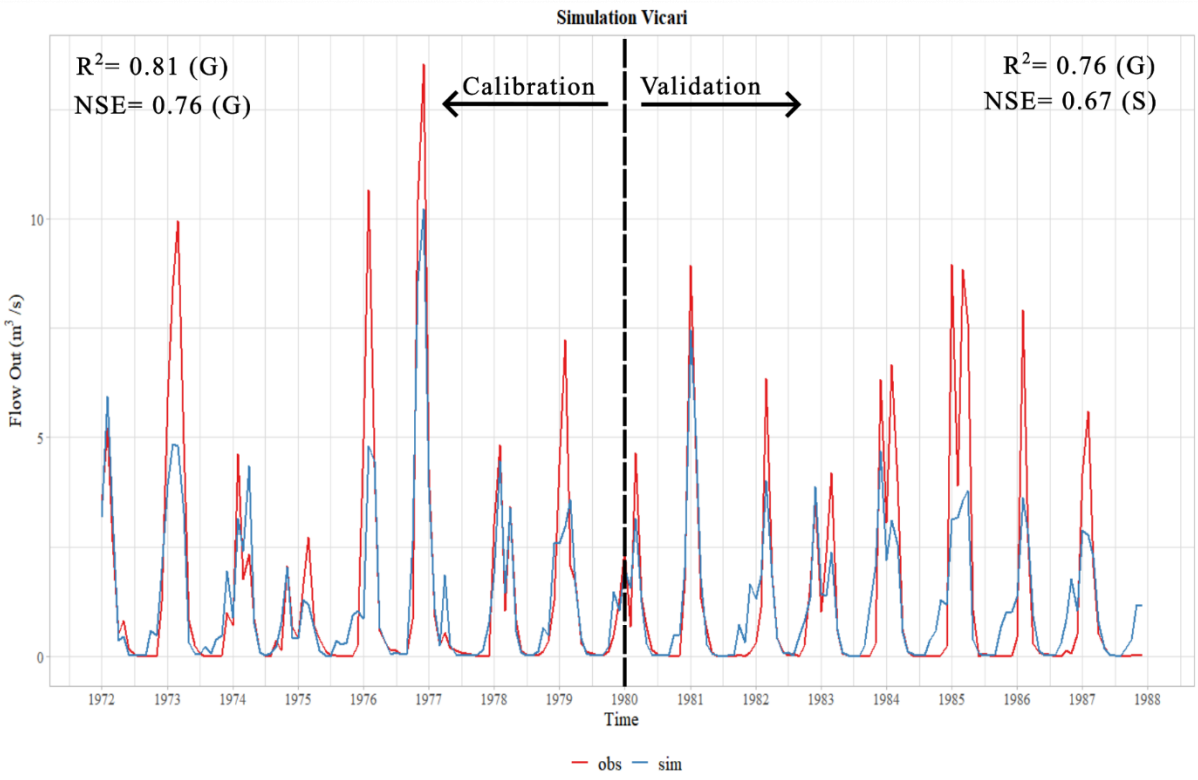

Figure 3.2.17 b) - Comparison between observed and simulated streamflow for scenario 1 in the Vicari Station

The analysis of the discharge values for both simulations in each month is shown in the boxplots of the following Figure 3.2.18. The observed data exhibits a higher degree of variability than the simulated data. In October, November, and December, the simulated data consistently has higher values than the observed data. Vicari exhibits a pattern where the simulated data are consistently lower than the observed data from January to May, except for April. Conversely, for the Monumentale station, the simulated data are consistently higher than the observed data from January to May, except for January.

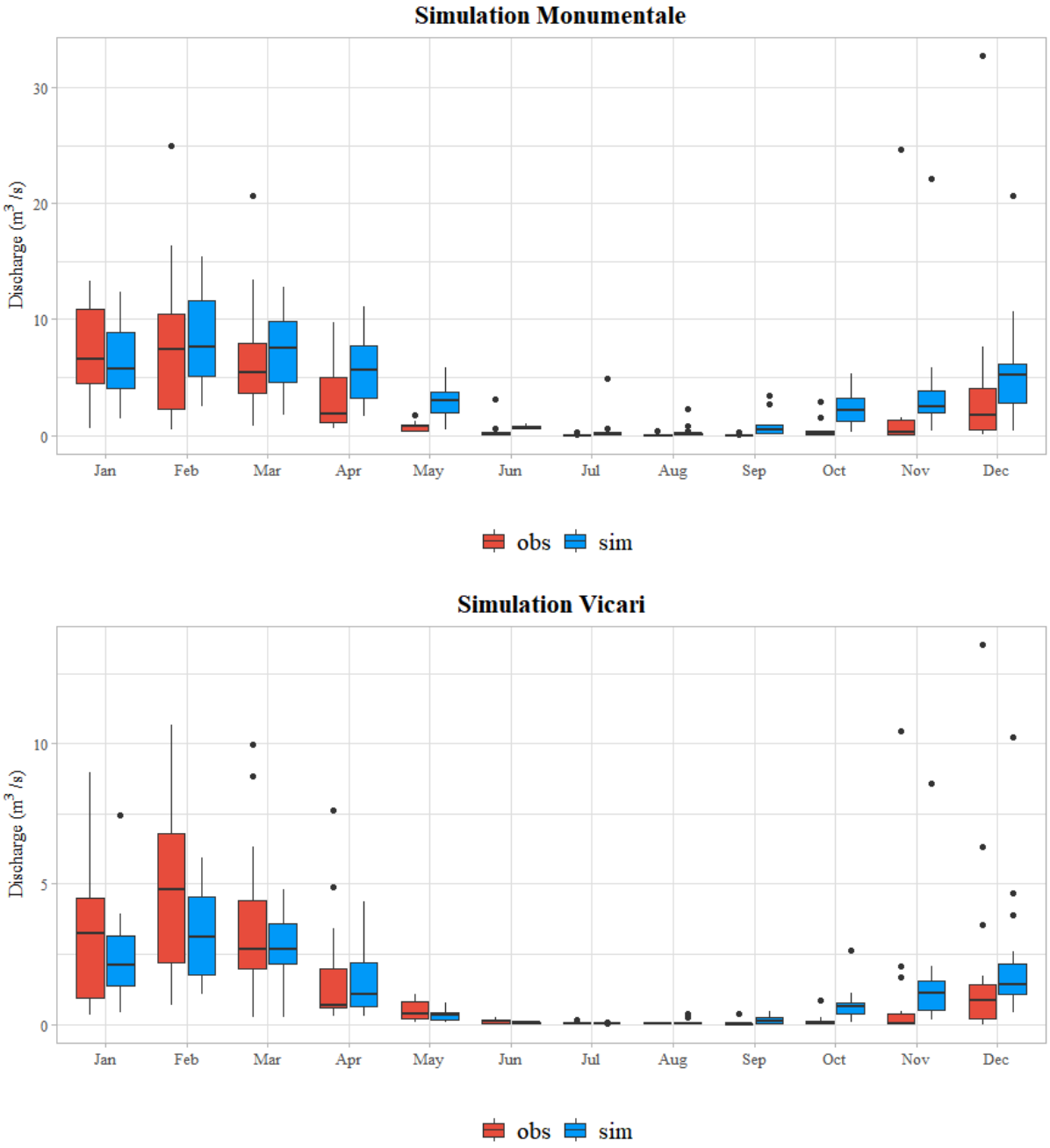

Figure 3.2.18 - Boxplots for observed and simulated data for both the station

The water balance components on the San Leonardo Basin illustrated in Table 3.2.6 show that the contributing area of the Vicari station exhibits higher potential and actual evapotranspiration. In contrast, the contributing area of the Monumentale section displays greater percolation, which is likely attributed to a higher presence of permeable soils.

	Precipitation		Potential Evapotranspiration	Actual Evapotranspiration	Percolation
	Average	Range	(mm/year)	(mm/year)	(mm/year)
Vicari (1972 - 1980)	52.30	0-330	39758.65	13690.06	656.59
Monumentale (1968 - 1980)	53.09	0-330	38767.27	11173.83	1687.67

Table 3.2.6 - The water balance components in the studied area

The contribution of surface runoff, lateral flow, and groundwater to the streamflow in mm/year have been illustrated in Table 3.2.7.

	Surface Runoff (mm/year)	%	Groundwater Contribution (mm/year)	%	Lateral Flow Contribution (mm/years)	%	Total Water Yield (mm/year)
Vicari (1972 - 1987)	1838	45%	201	5%	2040	50%	4081
Monumentale (1968 - 1980)	2514	38%	1116	17%	3068	46%	6699

Table 3.2.7 - The hydrology contribution for the studied area

Scenario 2

After the calibration and validation of liquid flow, the suspended sediment yield was calibrated and validated in this scenario. This process was conducted manually using the SWAT EDITOR software. Once the calibrated values were set as input data, the parameters that control erosion and sediment transport were subsequently adjusted (Table 3.2.8)

The initial step involved modifying the physical parameters associated with the main channel, specifically, the width (CH_W2) and depth (CH_D) when the channel is filled to the top of the bank, as well as their ratio (CH_WDR). The latter parameter is significant during the sediment transport calculation, SWAT allows for channel downcutting and widening, thereby enabling the channel dimensions to change during the simulation period. It is noteworthy that altering the depth and width of the channel can result in variations in the simulated discharge. Therefore, in this scenario, the comparison between the observed and simulated suspended sediment yield was preceded by a comparison of the flow discharge.

Parameter	Definition	Process	Range	Calibrated Value	
				Vicari (1972 - 1976)	Monumentale (1968 - 1974)
CH_W2.rte	Width of channel at top of banl (m)	Water Routing	0 - 1000	3	3
CH_D.rte	Depth of water in channel when filled to bank (m)	Water Routing	0 - 30	1	1
CH_WDR.rte	Channel width to depth ratio	Sediment Routing	0 - 10000	3	3
CH_COV1.rte	Channel erodibility factor	Sediment Routing	0.0 - 1.0	0.6	0.6
SPCON.rte	Coefficient in sediment transport equation	Sediment Routing	0.0001 - 0.01	0.0004	0.01
SPEXP.rte	Exponenet in sediment transport equation	Sediment Routing	1 - 1.5	1.1	1

Table 3.2.8 - The calibrated parameters relative to the suspended sediment yield

The other changed parameter is the minimum value for the cover and management factor for the land cover, USLE_C. The C-factor accounts for how land cover, crops, and crop management cause soil loss to vary from those losses occurring in bare fallow areas. The bare plot (no vegetation) with till up and

down the slope is taken as a reference condition, with C-factor value of 1. The soil loss from different land-cover types is compared to the loss from the reference plot, which is given as a ratio. The C-factor value for a particular land-cover type is the weighted average of those soil loss ratios and the range between 0 and 1. SLRs are computed as a product of five sub-factors: prior land use, canopy cover, surface cover, surface roughness, and soil moisture.

The values of the SWAT database have been changed using the values that were estimated at the European scale by Panagos et al., 2015 as reported in the following table 3.2.9:

Common Name	Plant Code	C_{USLE}	C-factor
Winter wheat	WWHT	0.03	0.15
Olives	OLIVE	0.001	0.19
Orange	ORAN	0.001	0.22

Table 3.2.9 -Values of USLE C-factor used for this study

The graphical results of streamflow and suspended sediment yield simulations performance during the calibration and validation periods are shown in Figures 3.2.19 and 3.2.20.

In Vicari Simulation, the statistical performance of monthly streamflow simulation falls in good range during calibration and also for validation. Similar results for stream flow have been achieved for the Monumemtale station.

The same results were not obtained for the simulation of sediments. The statistical parameters were not satisfactory both for Vicari and especially for Monumentale; only for the validation of Vicari were satisfactory statistical parameters achieved.

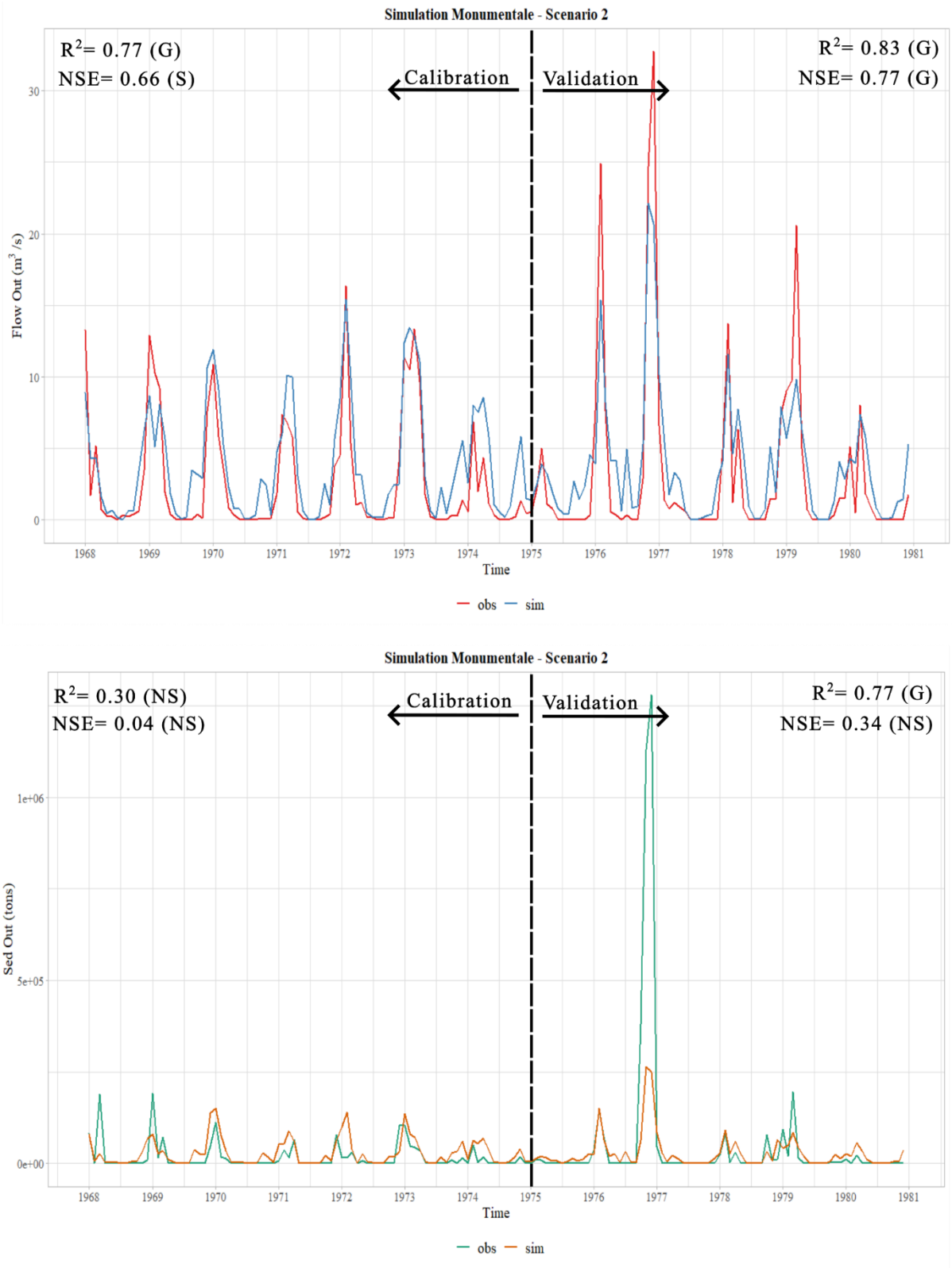

Figure 3.2.19 – Comparison between streamflow and suspended sediment yield for Scenario 2 for the Monumentale station

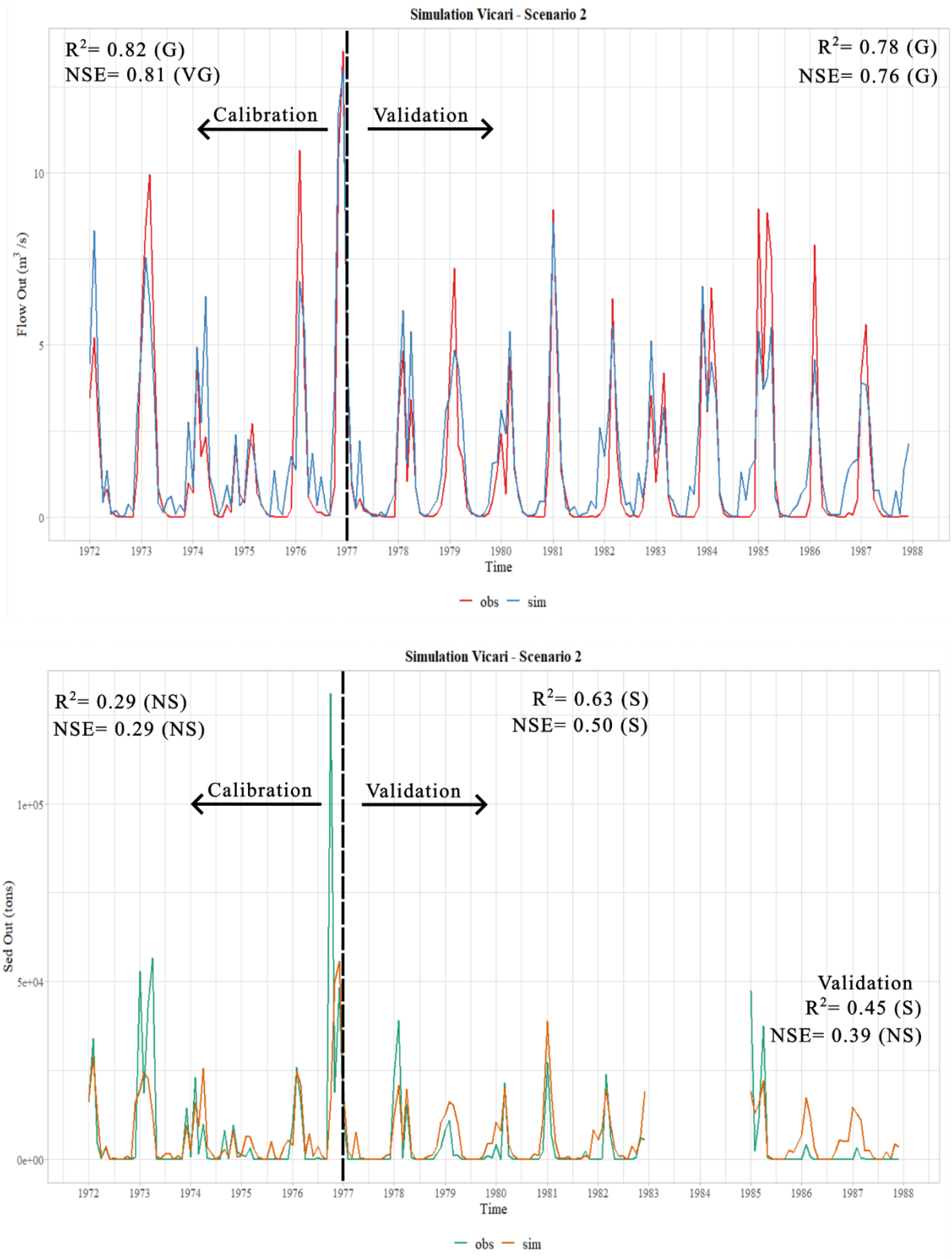

Figure 3.2.20 - Comparison between streamflow and suspended sediment yield for Scenario 2 for the Vicari station

Scenario 3

In this scenario, the year 1976 was omitted from the calculation of the performance of the model. The objective was to determine how the model's performance would be impacted by the unusual

precipitation, liquid, and solid flow values of this year. The Monumentale station's results are still unsatisfactory, but the Vicari station can still get satisfactory results even during the calibration phase.

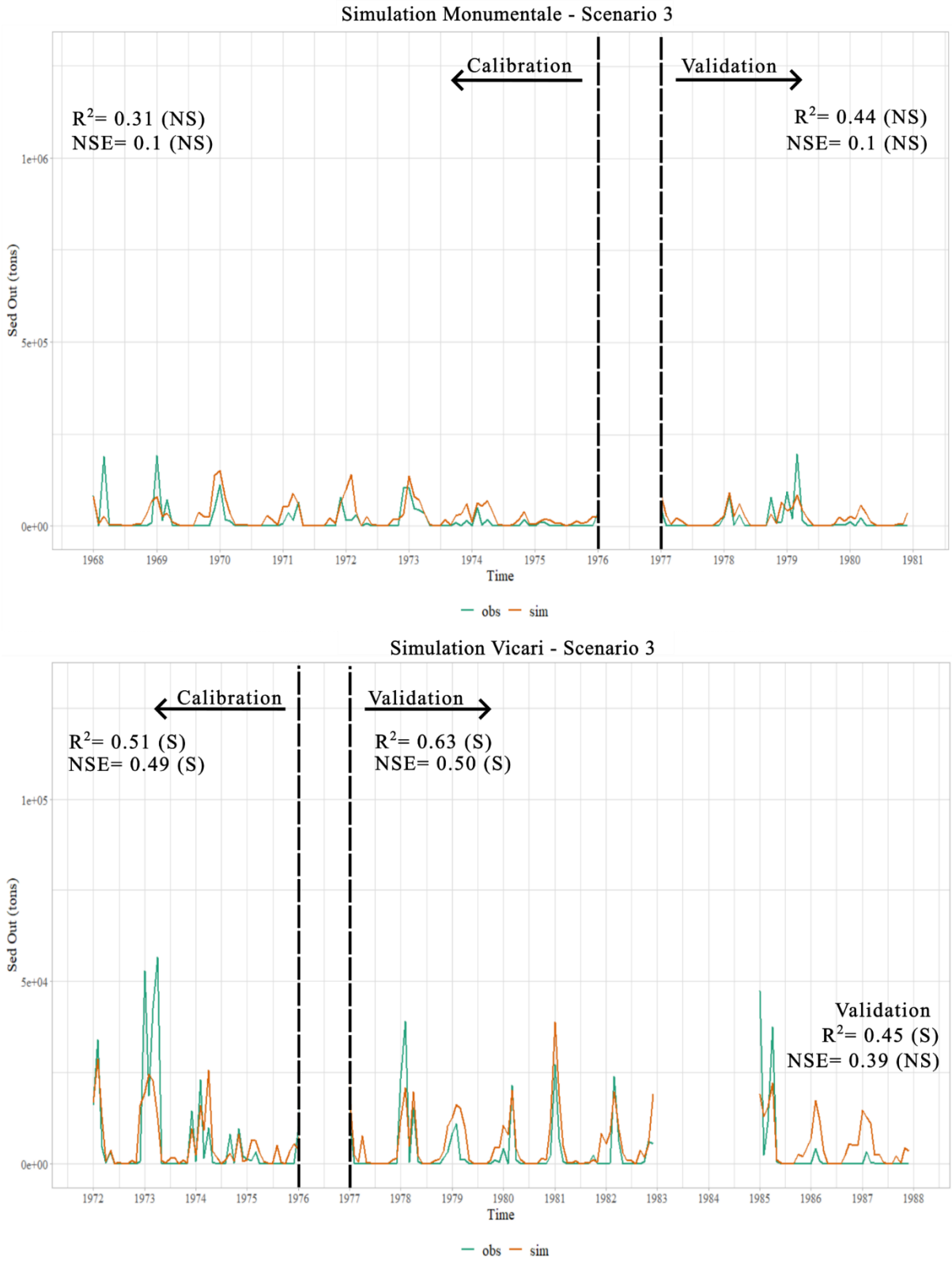

Figure 3.2.21 Comparison between Sediment Suspended Yield for Scenario 3 for both stations

3.2.5 CONCLUSIONS

This study represents one of the first applications of SWAT modeling for simulating sediment erosion in Sicily from historical monthly sediment yield data. Although the results obtained were unsatisfactory for the Monumentale station, satisfactory results were obtained at the Vicari station, which is characterized by a smaller drainage area. Some causes can be hypothesized to explain the observed SWAT limits. First, the historical database of solid transportation is based on averaged monthly data, missing any possibility of calibrating at the daily scale (which is the typical design of application adopted in SWAT modelling). Besides, the quality of the spatial layers that have fed the SWAT suite is low for some critical factors: soil type and land use maps. At the same time, in light of the differences in fitting between Monumentale and Vicari gauges, it is probably to be expected a more limited suitability of SWAT in deciphering the erosion process and related sediment budget for the complete catchment under the Mediterranean climatic context. In this sense, the specificity of time lags between sediment production and transportation stages is well simulated when the alluvial plain is absent, including only hillslope erosion processes (landslides, solifluction, creep, sheet-, rill- and gully erosion) and surface runoff for sediment delivery to the main channel. According to the results of this thesis work, SWAT seems to suffer in describing large river systems, where specific climatic tuning both on channel erosive processes and sediment delivery dynamics probably made the estimation of the sediment transportation at far channel sections too specific.

Finally, depending on the specific climatic forcing in Sicily, sediment stocks could be delivered to the main channel in form of massive landslide body foot, constituting highly erodible source of sediments for channel erosion processes, uncoupling the estimated and predicted sediment budget.

More accurate (soil and land use maps) and high-resolution (daily sediment yield) data efforts could be obviously exploited to search for higher fitting for SWAT. However, the focus of this study was to recover the long-term sediment budget behaviour in the San Leonardo river and test whether a reference historical pattern could be obtained.

3.3 AN APPROACH FOR THE VALIDATION OF A COASTAL EROSION VULNERABILITY INDEX USING WATEM/SEDEM

The last IPCC report, AR6 (Intergovernmental Panel On Climate Change, 2023), highlighted that climate change is already influencing weather and climate variables. Since 1950, the increase in temperature, and the increase in frequency, and intensity of extreme events has had an impact on various environments on Earth, including coastal areas. Coasts are highly dynamic and everchanging systems, especially in correspondence with beaches, where changes are easily visible through the advancing/retreat of the shoreline (Bird, 2008). The fragile balance of the coastal environment is affected by multiple physical phenomena, such as wave motion, tidal fluctuations, and currents, and human actions need to be taken into account.

Additionally, continental processes play a predominant role in coastal dynamics; sediment budget is one of three factors (sediment budget, sea level, and wave energy) that control coastal systems. The sediment budget refers to the balance between sediment added to and removed from the coastal system and the sources that deliver sediment to the coast. The principal sediment suppliers to most coasts are rivers that deliver sand directly to the beach. When more material is added than removed, there is a surplus of sediment, and the shore builds seaward. On the other hand, when more material is removed than is added, there is a deficit in sediment supply, and the shore retreats landward. For a given combination of anthropogenic impacts, such as deforestation, damming of the river, changes in land use and management patterns, and environmental forcing like rainfall and temperature, a river catchment will produce a certain amount of sediment flux, contributing significantly to increasing or decreasing sediment supply. In studying the vulnerability of the coastal system and in any management activity, it is therefore essential to have a model for estimating at the basin scale the amounts of eroded sediment and the amount of sediment transported by a river, from catchment to coast.

Coastal vulnerability is a spatial concept that identifies people and places susceptible to perturbations resulting from coastal threats, such as coastal storms and erosion phenomena (Koroglu et al., 2019). Coastal vulnerability is, in general, related both to the socio-economic interests and physical resilience of the involved population/structures and natural system, respectively. In particular, the proneness of a coastal sector to be modified by the interaction of natural phenomena such as marine and river processes can be investigated by analysing some of their controlling physical static and dynamic factors. Vulnerability values are frequently associated with coastal risk, in fact, they are part of the conventional procedures in consolidated practice in many management plans (Williams and Micallef, 2009).

Risk computation is performed through the well-known formula (Kron, 2005):

$$R = P \times V \times E$$

Where:

R is the risk, which expresses the expected loss of human life, injuries, and property, due to a particular event.
P is the hazard or the probability that in a given area, a potentially harmful event occurs with a certain intensity within a given time.
V is the vulnerability or the aptitude of a particular element to withstand the effects according to the intensity of the event.
E is the exposure value, referring to the element that must endure the event.
Vulnerability assessment can be performed through different methodologies, and these are often chosen according to the purpose of the application. In fact, a coast can be vulnerable to various physical phenomena, such as erosion, flooding caused by rising average sea levels, tsunamis, storm surges, etc. (Gornitz, 1991).

3.3.1 Literary review about Coastal Vulnerability Indexes

Many authors calculate vulnerability by referring to a classic "Coastal Vulnerability Index" (CVI), which measures the potential effects of erosion and marine flooding in a coastal area. The classical method for the estimation of CVI, which was introduced by the United States Geological Survey (USGS) (Gornitz and Kanciruk, 1989), requires four steps: the first concerns the choice of descriptive variables (e.g., geomorphology, shoreline changes, beach slope, tide and significant wave height), the second concerns the classification of variables through the definition of semiquantitative scores according to a scale ranging from 1 to 5 (1 indicates a low contribution to the coastal vulnerability of a specific variable and 5 indicates a high contribution), the third concerns the aggregation of the variables into a single CVI index (equal to the square root of the product of the classified variables divided by the total number of variables), and finally the fourth and conclusive step involves the classification of the CVI values in n different groups using the n percentiles as limits.
This procedure is widely used, but it ignores socio-economic aspects like the number of people affected, potentially damaged infrastructure, and economic costs. There are two possible approaches to consider the socio-economic aspects: using another index associated with the CVI or using descriptive variables regarding these aspects. Armaroli and Duo, 2018 estimated coastal vulnerability through another index, the "Social and Economic Status Vulnerability Index (ISEV)", which considers the effects of coastal phenomena on the social and economic status of the citizens who live in these areas (Tapsell et al., 2002).
In the 2010, Mclaughlin and Cooper, highlighted the importance of coastal vulnerability assessment for management plans. The authors noted that the calculation of coastal vulnerability due to erosion depends strongly on the aggregation of various parameters (indicators), which, when spatially analysed, allow the estimation mapping of the vulnerability. These indicators/parameters are usually applied on a global, national, and regional scale, causing various degrees of simplifications and aggregation of information. The desirable simplification degree depends on the management scale; therefore, a higher

resolution is required on the local scale than on the regional scale one. The aim of the Paola et al., 2011 research was to verify the vulnerability indices obtained with two different methodologies, namely that of USGS and Gornitz, (1991) and that of López Royo et al., (2016). The first calculates the coastal vulnerability index (CVI) using geological and physical parameters, while the second, instead, calculates a "coastal impact" indicator, introducing, for its estimate, new parameters such as wave motion, run-up, and long-term and seasonal erosion indexes. The authors, applying the two methods in the same coastal area, observed different results. This is mainly due to the distinctiveness of the methods used. Therefore, considering the results, the authors emphasize that the choice of a methodology for assessing the vulnerability of a given coastal area must be based on the available information and the physical characteristics of the area under study. Additionally, Koroglu et al., (2019) compared different methodologies in order to calculate the vulnerability index. Indeed, the authors' objective was to choose a method to calculate the CVI in a univocal way. Their results promote Shaw's method (Shaw et al., 1999) as the one that comes closest to reality. However, their study highlights the need to generate unique classes for the parameters that allow the calculation of the CVI and for the CVI parameters. In fact, the method applied for calculating CVI for a specific region with specific hydro-geomorphological conditions is not necessarily applicable to other regions.

Furlan et al., (2021) calculated a new vulnerability index, the Multi-Dimensional Coastal Vulnerability Index (MDim-CVI). This index, created to estimate the vulnerability to flooding caused by sea-level rise, integrates a composite set of physical, environmental, and socio-economic indicators. In particular, the authors consider a set of geomorphological vulnerability indicators (e.g., height above sea level, distance from the coast, coastal evolution trend), exposure and adaptability (e.g., sensitive segments of the population, GDP, land use patterns). The methodology was applied to a reference time horizon representing the current climatic and land use conditions and a future scenario, integrating both climate projections and data simulating the potential evolution of the system's environmental and socio-economic characteristics.

3.3.2 Study Area

Sicily is the largest island in the Mediterranean Sea, and its coast is about 1600 km long. Coastal environments have great variability in terms of geology, morphology, marine climate, anthropization, etc. About 30% of the total Sicilian coastline is rocky, divided into low carbonatic shelves and high rocky headlands. The remaining 70% of the Sicilian coastline comprises low coasts with sandy and/or pebble beaches. The latter are the majority in terms of length and often suffer from erosion phenomena. In this paper, the Sicilian coastline was classified into three macro-coastal sectors (Fig. 3.3.1):

- the Tyrrhenian coast between Boeo Cape and Peloro Cape.
- the Ionian coast between Peloro Cape and Passero Cape.
- the Central Mediterranean coast between Passero Cape and Boeo Cape.

The continental shelf facing the Tyrrhenian coastal sector has a width of about 7 km. From Boeo Cape to Palermo, the coast is characterized by a sequence of high rocky (carbonatic) coasts and sandy beaches limited landward by sea terraces and escarpments. In some cases, the coast becomes low and rocky. The coast near Palermo is mainly artificial due to its high urbanization (harbors, coastal structures, old demolition waste, etc.). In the eastern direction, towards Termini Imerese, the coastal landscape becomes flat with large alluvial areas. These areas are limited seaward due to wide beaches. Looking eastward, the coast is mainly characterized by narrow beaches separated by reliefs. The last sector near Peloro Cape derives from the dismantling of the Peloritani chain, which has produced a system of alluvial plains, which are connected to the sea through large beaches disconnected by high headlands. The Central Mediterranean coastal sector has an average continental shelf that is 20 km wide. The coast is characterized by several large sandy beaches bounded landward by large alluvial deposits. The north-west coast sectors are made up of marly active and inactive cliffs, while the south-east coast (near Passero Cape) is characterized by carbonatic cliffs which often enclose pocket beaches.

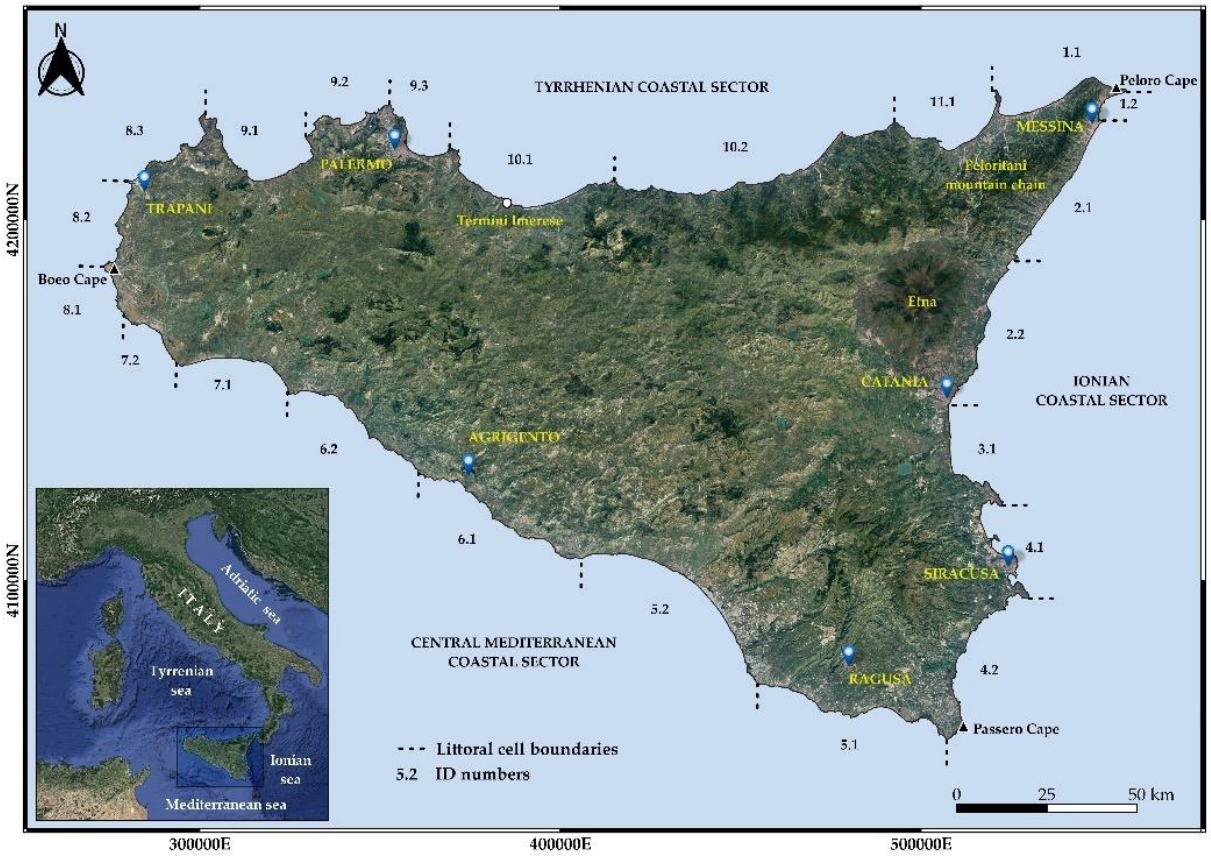

Figure 3.3.1 - Sicilian macro-coastal sectors divided into littoral cells of the second level. For each littoral cell, the first number identifies the first hierarchic order, and the second number identifies the second hierarchic order. For example, LC 5.2 means a littoral cell of the second hierarchic order of number 2 belonging to the littoral cell of the first hierarchic order of number 5.

Finally, the Ionian coastal sector has a 5 km wide continental shelf, smaller than the other two macro-coastal sectors. From Peloro Cape to the Catania urban area, the coast is similar to the Tyrrhenian coast because of the proximity of the Peloritani mountain chain. Additionally, this sector hosts wide beaches and rocky headlands (generally carbonatic rocks). In the Catania gulf, the geological substratum of the

coast changes, becoming mainly volcanic with basaltic rocks. Additionally, in this case, near Catania city, the coast is mainly armored. From the Catania Gulf to Passero Cape, the coast is characterized by a succession of narrow beaches and carbonate headlands. Carbonate reliefs bound the beaches landward. In this sector, small coastal marshes are protected areas due to their natural importance. In summary, the Sicilian coastal morphotypes can be classified as: (a) reflective pebble beaches on the eastern Tyrrhenian coast and Northern Ionian coast; (b) dissipative sandy beaches on the Mediterranean coast; (c) complex coastal areas such as marshes, littoral arrows, etc.; (d) active and inactive cliffs, mostly distributed on the Agrigento, Siracusa and Catania coasts; and (f) anthropized coasts where manmade structures characterize the coastline.

The Sicilian coast was segmented into 22 s-level littoral cells (LCs) to analyze the coastal dynamics and assess the erosion vulnerability. Littoral cells usually belong to a specific hierarchic order, at the first, second and third levels. Technicians and researchers choose the hierarchic order according to the study scale. The littoral cells or sediment cells contain sediment sources, transport paths and sinks. Each littoral cell is isolated from an adjacent cell and can be managed as a unit. In Sicily, there are 11 main littoral cells divided into 22 sub-cells named, respectively, first- and second-level cells. The first level of littoral cells has only natural boundaries, and the second level can include artificial boundaries (big harbors, sea work, etc.). Such a hierarchic classification is sufficient for regional study purposes because details are not needed at a large scale. Littoral cells are coded by two numbers such that the first number identifies the littoral cell of the first hierarchic order and the second number identifies the littoral cell of the second hierarchic order. For example, LC 5.2 means that we are observing the littoral cell of the second hierarchic order of number 2 belonging to the littoral cell of the first hierarchic order of number 5.

3.3.3 Materials and Methods

To assess the coastal vulnerability conditions, 500 m transects crossing the Sicilian coastline were generated with a 50 m interval between them, for a total of 23,680 transects. The CeVI evaluation was then applied to the 10,558 transects (Fig. 3.3.2) which cross the polygons that originated at coastline intersections. Transects where the shift between the two coastlines (years 2000 and 2020) was lower than the threshold of 6 m (pixel resolution value) were excluded from the analysis. This segmentation aimed at ranking different sections of coastline based on vulnerability and helped to determine high-priority areas for vulnerability reduction.

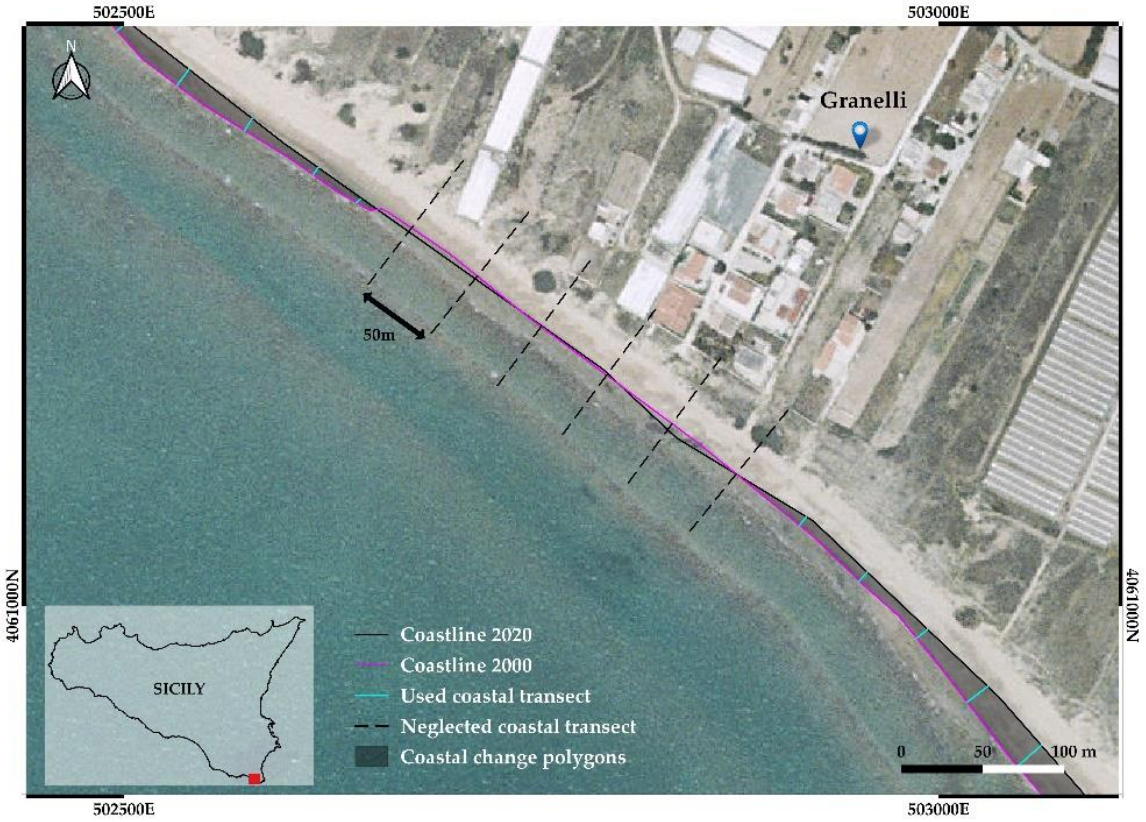

Figure 3.3.2 - Example of coastal transect generation (Littoral Cells 5.1). Black dashed lines show the transects neglected in CeVI assessment, while cyan lines mark those used to assess CeVI indicators. The red box on the south of Sicily represents the study area. The background image is the orthophoto "Volo IT2000" related to 2000.

According to the approach which was adopted in this study, the following heuristic method was applied (Figure 3.3.4): (1) a set of indicators which potentially control coastal erosion phenomena were computed and assigned to each transect; (2) each indicator was then reclassified according to expert-based criteria, and an overall Coastal Erosion Vulnerability Index was then obtained as a combination of the classes of the five indicators; (3) the estimated CeVIs were then compared with the observed coastal advancement/retreat signal; and finally, (4) to explore the importance of the sediment supply, which is not among the commonly used factors in models, included (complete) and not-included (leave-out) models were prepared and compared.

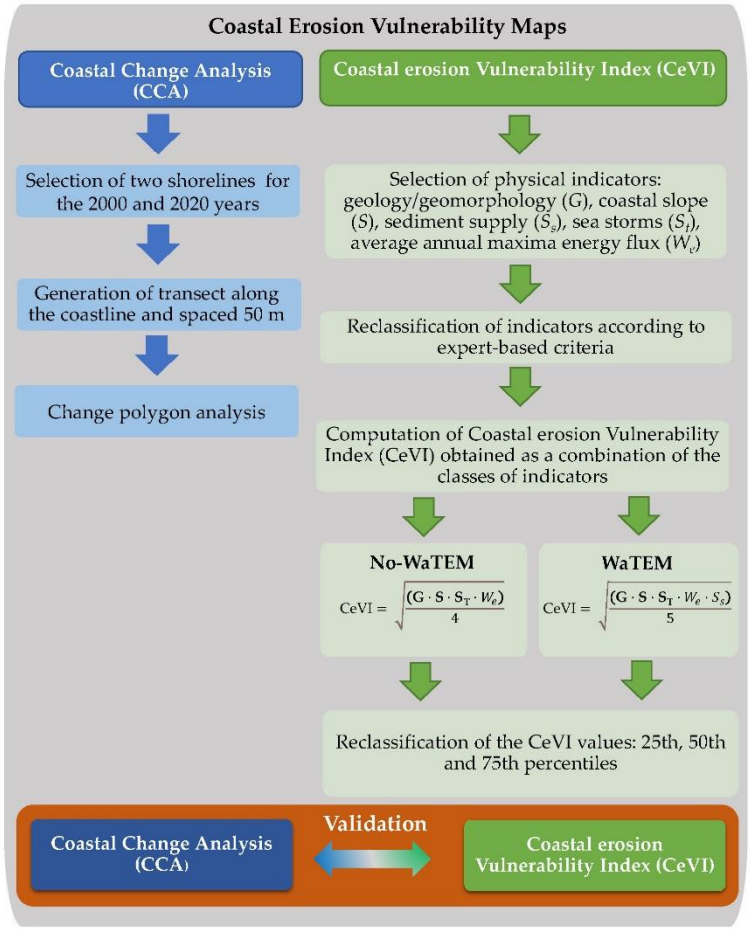

Figure 3.3.3 - Flow chart related to the new method applied.

- *CeVI Indicators*

Five physical indicators were used to assess the Sicilian coast's erosion vulnerability index: (1) a geological/geomorphological indicator (G), (2) a coastal slope indicator (S), (3) an erosion/sediment supply indicator (Ss), (4) a sea storm indicator and (St), and (5) an average annual maxima energy flux indicator (We) (Table 3.3.1). The coastal physical and environmental indicators (G, S, Ss) represent the resistance or susceptibility of coastlines to physical variations, and the wave climate-related indicators (St, We) represent the coastal forcing. As reported in the last column of Table --, the indicators were calculated and assigned to littoral cells (LC: Ss, St and We) or coastal transects (CT: G and S). The physical indicators have different data formats and were obtained directly or indirectly by calculating them from other parameters supplied by specific operational services. In particular, geomorphologic and geologic parameters were obtained from ISPRA (Italian Institute for Environmental Protection and Research), the coastal slope was computed from a 2 m × 2 m Digital Elevation Model (DEM) provided by the Sicilian SITR (Regional Territorial Information System), the sediment supply was obtained by analysing data from ESDAC (European Soil Data Centre), and finally the parameters linked to the sea were obtained by analysing the data provided by CMEMS (Copernicus Marine Environment Monitoring Service). The sediment supply, the number of sea storms, and the wave energy flux

indicators, computed directly from the raw data, were calculated for each littoral cell. A quartile reclassification was then applied, thus obtaining four intervals for each parameter, with these intervals expressing vulnerability ordinal scores in the range from 1 (lowest vulnerability) to 4 (highest vulnerability). The vulnerability scores of the indicators for the littoral cells were then assigned to each included coastal transect. In contrast, the geomorphology, geology, and coastal slope indicators were separately computed for each coastal transect.

Physical indicators	**Data type**	**Reprocessed data**	**Data source**	**Assessed using**
Geomorphology and Geology (*G*)	Shapefile	-	ISPRA (Italian Institute for Environmental Protection and Research)	CT
Coastal slope (*S*)	Raster file	✓·	DEM 2x2 – SITR Regional Territorial Information System)	CT
Sediment supply by river basins (S_s)	Raster file	✓·	WaTEM/SEDEM - ESDAC (European Soil Data Centre)	LC
Sea storms (S_t)	NETCDF file	✓·	CMEMS (Copernicus Marine Environment Monitoring Service)	LC
Average of annual maxima energy flux (W_e)	NETCDF file	✓·	CMEMS (Copernicus Marine Environment Monitoring Service)	LC

Table 3.3.1 - Data sources of the parameters used in CeVI assessment. (LC—Littoral Cells, CT—Coastal Transects).

Figure 3.3.4 shows a stretch of the Sicilian coastline, belonging to 5.2 LC, with the two different shorelines (2000–2020) and related transects. An ID identifies each transect, linked to the columns of the table in Figure 3.3.4 where the scores of all the adopted indicators are reported (Figure). As the last three columns of Figure 3.3.4 report the indicators related to the same littoral cell, they have the same values (Ss = 3, We = 2 and St = 1).

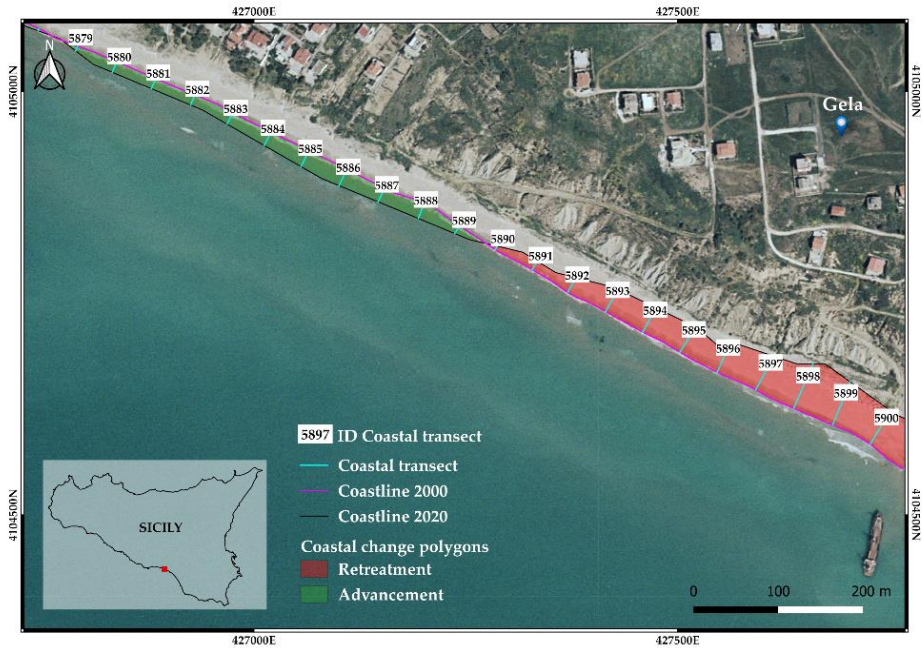

ID	G	S	S_t	W_e	S_n
5879	4	2	3	2	1
5880	4	2	3	2	1
5881	4	2	3	2	1
5882	4	2	3	2	1
5883	4	2	3	2	1
5884	4	2	3	2	1
5885	4	2	3	2	1
5886	4	1	3	2	1
5887	4	2	3	2	1
5888	4	2	3	2	1
5889	4	2	3	2	1
5890	4	3	3	2	1
5891	4	3	3	2	1
5892	4	4	3	2	1
5893	4	3	3	2	1
5894	3	4	3	2	1
5895	3	4	3	2	1
5896	3	4	3	2	1
5897	4	4	3	2	1
5898	4	4	3	2	1
5899	4	4	3	2	1
5900	4	4	3	2	1

Figure 3.3.4 - A coastal stretch of the Sicilian southern sector from LC 5.2. The orthophoto image corresponds to the year 2002 (ISPRA). Subplot (a) shows the polygons and related transects named with an ID. Subplot (b) shows a table linked to the indicator values for each transect. The red box on the south of the isle of Sicily represents the study area. The background image is the orthophoto "Volo IT2000" related to the year 2000

Geomorphology and Geology

Coastal geomorphology and the nature of the outcropping rocks play an important role in assessing coastal vulnerability because they express both its erodibility and the resistance degree to erosion (Thieler, 2000). Generally, the presence of low coasts and unconsolidated sediments (e.g., beaches, estuaries, lagoons, deltas, etc.) offers the least resistance to erosion and, therefore, very high vulnerability compared with higher coasts formed by substrates (consolidated sedimentary or crystalline rocks) (Gornitz and Kanciruk, 1989). The ISPRA (Italian Institute for Environmental Protection and Research) Coastal Geoportal was used to define the geomorphology and geology characteristics of the Sicilian coast (https://sinacloud.isprambiente.it (accessed on 23 December 2022)), by downloading the "coastline 2020" shapefile. This vector corresponds to the coastline of the whole Italian littoral corresponding to the year 2020, classifying the coast in terms of geomorphological and geological settings. In particular, three macro-elements are defined: natural, artificial, and fictional. The first is divided into high and rocky coasts and low coasts (sandy beaches, gravelly beaches, and gravelly beaches with boulders). The second divides the coast considering the presence of defense works, harbors, beach clubs, etc. Finally, fictional coasts are the stretches of coast that connect the start and end points of maritime work. For each coastal transect, the geomorphological and geological information was derived from the intersection of the coastal transect with the "coastline 2000" shapefile. Subsequently, vulnerability scores were assigned based on the relative erodibility of different landform types, varying from high cliffs to sandy beaches.

Coastal Slope

The coastal slope, expressed as a percentage, is one of the indicators of coastal vulnerability. On a gently sloping coast, the environment is dissipative, and the sea storm energy can produce consistent sediment transport phenomena. On the other hand, on steeply sloping coasts, the waves dissipate their energy by breaking on the rocks. It is important to highlight that the slope is only an indicator, and the overall results are related to several aspects. Clearly, very steep coasts can exist that are vulnerable, and conversely, gently-sloping coasts that are not vulnerable can exist. This is because the results are related to the combination of all of the indicators. The first step was to compute the subaerial coastal plain slope from the 2m x 2m DEM provided by the regional geo-information system. The value was calculated for the centroid of each transect. In particular, the mean value within a 25 m radius for each centroid was calculated. The vulnerability ranges related to the coastal slope parameters were chosen considering previous studies carried out on the Mediterranean coast. The mean slope was classified into ranges—from 0% to 2% (very high), from 2% to 4% (high), from 4% to 8% (moderate) and >8% (low)—following those proposed by Mclaughlin and Cooper, (2010).

Sediment Supply by River Basins

River sediment supply is critical in a dynamic and complex multi-functional system such as a coastal area. An alteration of the transfer of river sediment to littoral sediment budgets causes an increase or reduction in sediment discharge. To express this factor with an indicator, the quantitative estimates of net soil erosion and deposition rate obtained from the application of the spatially distributed sediment delivery model WaTEM/SEDEM (from this point forward named WaTEM) at the European scale were used Borrelli et al., (2018). Source data were directly acquired from the ESDAC (European Soil Data Centre) database as a 25 m-pixel-size layer based on the RUSLE (Revised Universal Soil Loss Equation) model and a transport capacity routing algorithm. By applying SAGA-GIS tools (zonal grid statistics), the contributing fluvial basins feeding the catchment area of each littoral cell were first identified. The sediment delivery budget at each littoral cell was then calculated as a sum of negative (soil loss) or positive (deposition) pixel values obtained from the WaTEM layer. Finally, using quartile ranges, four vulnerability classes were obtained from 1 (lowest vulnerability) to 4 (highest vulnerability). It is worth noting that the more negative the value, i.e., the more sediment lost from the basin, the greater the expected sediment supply towards the coastline underlying the same basin. Therefore, low values of sediment supply correspond to a low vulnerability class.

Sea Storm and Average of Annual Maxima Energy Flux

The Copernicus Marine Environment Monitoring Service (CMEMS) provides oceanographic products and services, and it aims to routinely make available quality-assured products on the past, present, and future state of the sea. The Copernicus data are useful for several studies, such as coastal flooding and wave conditions at sea, environmental assessments, and climate studies. To characterize the wave motion climate around the Sicilian coasts, the CMEMS dataset was used. Wave parameters were

obtained from "MEDSEA_ MULTIYEAR_WAV_006_012" data (https://resources.marine.copernicus.eu---last accessed on 18 October 2022), which offer a reanalysis dataset and an interim dataset covering the period after the reanalysis until one month before the present. The reanalysis dataset is a multi-year wave reanalysis starting from January 1993, composed of hourly wave parameters at 1/24◦ (about 4 km) horizontal resolution, covering the Mediterranean Sea. In particular, the parameters extracted from the CMEMS dataset are the spectral significant wave height (Hm0), wave period at spectral peak/peak period (Tp), and mean wave direction (q). The CMEMS dataset is computed using the wind data from the ECWMF (European Centre for Medium-Range Weather Forecasts) with a spatial resolution of 0.5◦ × 0.5◦. Figure 5 shows the CMEMS points around the Sicilian coasts and the related catchment areas. The wave climate of the Sicilian coast was analyzed for the time interval of the present study. Two hundred and two points were extracted from the CMEMS reanalysis dataset (Figure 3.3.5). The need to select a parameter characterizing each coastal stretch required spatial averaging. In particular, a mean value was assigned to each coastal littoral cell, obtaining Hm0, Tp, and q. The spatial average of the wave parameters was used to assign wave climate to the given coastal cell. These wave climate parameters are the basis for computing the CVI indicators regarding the wave climate. In particular, the following indicators were taken into consideration: the number of sea storms and the average of the annual maxima energy flux. Sea storms were defined using the approach proposed by (Boccotti, 2000). Therefore, a Mediterranean Sea storm was defined as a sequence of sea states in which the spectral significant wave height (Hm0) exceeds the threshold of 1.5 m and does not fall below this for a continuous-time interval greater than 12 h. The number of sea storms registered in the period from 2000 to 2020 was computed for each LC (see Table 3.3.2). The wave energy flux plays a key role in vulnerability assessment. To consider its variations, the annual average maximum was computed. For each studied year and for each littoral cell, the maximum value of wave energy flux was computed (P). Thus, these maxima were averaged over time, obtaining a unique value for each cell. The values of the number of sea storms in the study period vary between a minimum of 14 for the 1.2 littoral cells (Ionic sector) and a maximum of 661 for the 7.2 littoral cell (Mediterranean sector), with an average value of around 352; in general, the highest average values are found along the Central Mediterranean coast, whereas the lowest are in the Ionic sector. The average of the annual maximal energy flux has a maximum value of 143.83 kW/m for the 8.3 littoral cell in the Tyrrhenian sector, while the minimum value, 19.98 kW/m, is in the same littoral cell, in which the lowest number of sea storms occur.

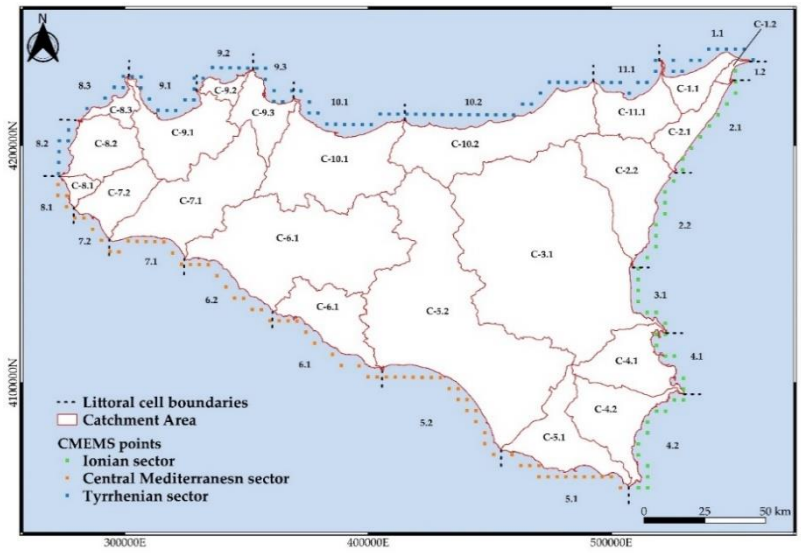

Coastal Sectors	Littoral Cells	Sea Storms (2000-2020)	P (kW/m)
Ionian	1.2	14	19.98
	2.1	103	50.65
	2.2	163	83.33
	3.1	168	84.17
	4.1	335	119.41
	4.2	279	101.2
Central Mediterranean	5.1	505	79.14
	5.2	421	76.12
	6.1	468	76.2
	6.2	460	72.6
	7.1	602	93.14
	7.2	661	111.95
	8.1	658	137.94
Tyrrhenian	8.2	464	90.01
	8.3	589	143.83
	9.1	181	53.57
	9.2	518	110.94
	9.3	126	43.65
	10.1	228	61.53
	10.2	355	90.39
	11.1	207	54.27
	1.1	250	68.32

Figure 3.3.5 - Sicilian hydrograph catchments related littoral cells and relative CMEMS points; Table 3.3.2 - Computed values of the sea state for each Sicilian macro sector.

- *CeVI Computation*

Once each coastal transect had been assigned a vulnerability class from 1 (low vulnerability) to 4 (high vulnerability) for each indicator (Table 3.3.3), the overall Coastal Erosion Vulnerability Index (CeVI) was calculated by applying the same scheme of the commonly adopted version proposed by (Gornitz and Kanciruk, 1989), as the square root of the product of the indicators, divided by the number of indicators n (Equation --):

$$CeVI = \sqrt{\frac{(G * S * S_s * S_t * W_e)}{n}}$$

Where:

G is the indicator pertaining to geomorphology and geology.

S is the coastal slope

S_s is the indicator related to sediment supply by river basins

S_t is the indicator related to the sea storms

W_e is the average of annual maxima energy flux

n is the number of indicator used.

Table 3.3.3 - Coastal vulnerability ranges for each physical indicator. UM—Unit of Measurement.

Physical indicators	**UM**	**Coastal erosion Vulnerability Index ranking**			
		1 - Low	2 - Moderate	3 - High	4 -Very High
Geomorphology and Geology (G)	nominal	High rock cliffs, Coastal embankment with	Low rock cliffs, Artificial shoreline (walk, quay) without beaches, Coastal	Gravel beaches, Estuaries, Sand beaches with boulders	Sand beaches

		construction, Harbor area	defense, Gravel beaches with boulders		
Coastal slope (S)	%	> 8	4	2	< 2
Sediment supply by river basins (S_s)	Mg/ha·year	< -1.3x10^7	-3.9x10^6	-1.7x10^6	> -1.7x10^6
Sea storms (S_t)	count	< 187.5	345	495	> 495
Average of annual maxima energy flux (W_e)	kW/m	< 63.23	81.23	99.19	> 99.19

The overall CeVI values were then re-classified into the 25th, 50th and 75th percentiles representing the CeVI's range of classes: class 1, low vulnerability (0–25th percentile); class 2, medium vulnerability (25–50th percentile); class 3, high vulnerability (50–75th percentile); and class 4, very high vulnerability (>75th percentile).

To calculate the CeVI values and to analyze the role of sediment supply, two approaches were followed. The first did not consider the contribution of sediments coming from river catchments (No-WaTEM; Ss = 0), whereas the second considered it (WaTEM). Therefore, in the No-WaTEM model, the indicators used to calculate CeVI were G, S, S_t, and W_a, whilst the WATEM model computed CeVI using G, S, S_t, and W_a and S_s. By means of the WaTEM and No-WaTEM models, the CeVI value was computed for each transect. Once we obtained the CeVI values, they were classified into 4 vulnerability classes (class 1: 0–25th percentile; class 2: 25th–50th percentile; class 3: 50th–75th percentile and class 4: >75th percentile).

- *Validation*

Unlike previous applications of the vulnerability index, which typically include historical coastline evolution data (erosion/accretion trend) as an indicator of the potential impact of climate change (López Royo et al., 2016), in this study the observed 2000/2020 coastline change rate (m/y) was rather used to validate the proposed CeVI methodology.

Coastline Change Analysis (CCA)

The coastal change analysis was performed using the two shorelines extracted for the years 2000 and 2020. These polylines are the result of the identification and vectorization of the shoreline by satellite images. Both the shorelines in 2000 and 2020 were obtained from the ISPRA database (https://sinacloud.isprambiente.it/portal/apps/sites/#/coste (accessed on 23 December 2022). ISPRA, to obtain the shoreline, chose the wet and dry limit as a specific geo-indicator (Boak and Turner, 2005). Indeed, among the different geo-indicators that can be identified in the aerial and/or satellite images (instantaneous rise line of the wave motion on the beach, vegetation line of the dune closest to the sea,

erosion step of the beach, storm line, resurgence line of the water, maximum breaking line, etc.), the wet/dry limit is the one most easily recognizable in aerial and satellite images. Despite being influenced by the sea climate, the wet/dry limit is a stable geo-indicator of the shoreline, and for this reason is more reliable than the indicator known as the instantaneous run-up limit. The use of the wet/dry limit, although among the most reliable for the location of the shoreline, does not, however, exclude the presence of uncertainties related to the exact position of the border. This obviously also applies to all of the other geo-indicators. The coastline intersections produced the change polygons which were used for the coastal change analysis. To assess the Sicilian coastal change, the polygon approach was adopted: the coastline intersections generated a series of change polygons which defined retreating or advancing coastal areas. Each area is equal to the coastal length multiplied by its width. On these geometric bases, the area between two coastlines corresponds to the change in area and the width is interpreted as the average shift in the shoreline in time (the period between the two shorelines) (Smith and Cromley, 2012). Positive areas (advancing) and negative areas (retreating) are linked to the shoreline cross points. The sum of these areas reflects the total coast area change over time. The coastline change analysis was carried out using QGIS software.

CCA and CeVI Comparison

To calculate the response value in terms of retreat or advance (meters), the coastal transects were intersected with polygons obtained from the CCA, and the coastline change rate (CCA—m/y) was derived as positive or negative values indicating accretion or erosion rates. Then, the historical coastline evolution data were classified as low, medium, high, and very high vulnerability (Table 3.3.4). The threshold for class 4 was selected as corresponding to the first quartile of retreat, whilst classes 1 to 3 were split considering the estimated error of 0.150 (3 m/20 years) that we assumed in the estimation of the coastline change rate.

Observed	**Coastal erosion Vulnerability Classification**			
response	1 - Low	2 - Moderate	3 - High	4 -Very High
CCA (m/year)	> + 0.150	≤ + 0.150	< - 0.150	< -0.510

Table 3.3.4 - Coastal erosion vulnerability classification.

A validation procedure of the overall CeVI values was applied to compare the vulnerability values of the coastline variation (CCA) and the overall CeVI values; this comparison provides a qualitative and relative assessment of the CeVI procedure effectiveness. Theoretically, transects with a high vulnerability class for coastline variation should have a high CeVI class and transects with a low vulnerability class for coastline variation should correspond to a low CeVI class.

3.3.4 Results and Discussion

The graphs obtained from the results of theWaTEM and No-WaTEM models are shown in Figure 3.3.6, where the classes of CeVI and the coastal change rate expressed in m/year are plotted. The boxplots show the distribution of coastline change rate measured along the transects (m/year) for the four CeVI classes and the magenta line refers to the reference coastline. For this reason, a median above the magenta line suggests coastal advancement, whereas a median below the magenta line indicates coastal retreat. The whiskers of the boxplots, for each class, represent the variability of the transects for each class. In both the adopted models (No-WaTEM and WaTEM), a gradual shift towards coastline retreat was recorded by moving from low to high vulnerability. In particular, the No-WaTEM and WaTEM models discriminate classes 1 to 3 from class 4 (p value < 2e-16), and class 1 from classes 2 to 4 (p value < 2e-16), respectively. At the same time, a similar behavior arises employing the reclassified CCA classification according to Table 3.3.4. Figure 3.3.7 shows the coupling among the four different classes of CeVI and CCA, reported by counts.

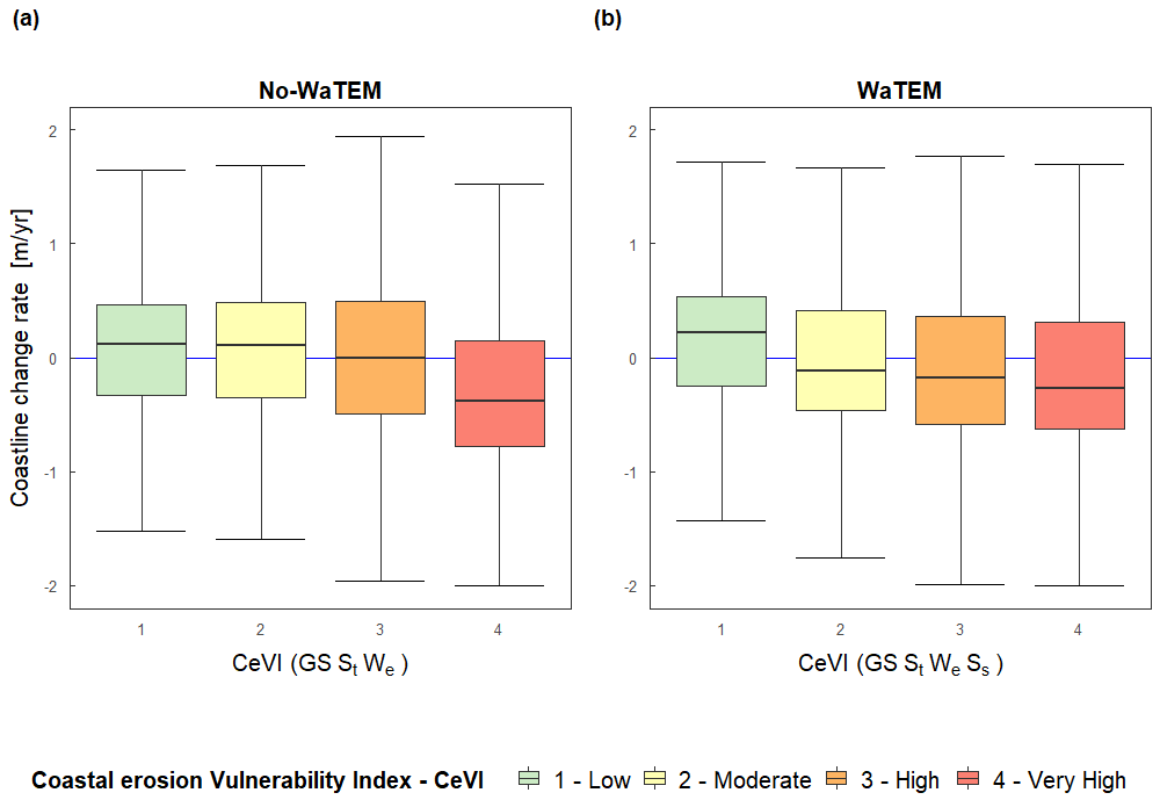

Figure 3.3.6 - Boxplot for No-WaTEM andWaTEM models. The first shows a median value decrement of the CCA values corresponding to the CeVI classes 3 e 4. The second shows a decrement median value of the CCA for all the CeVI classes.

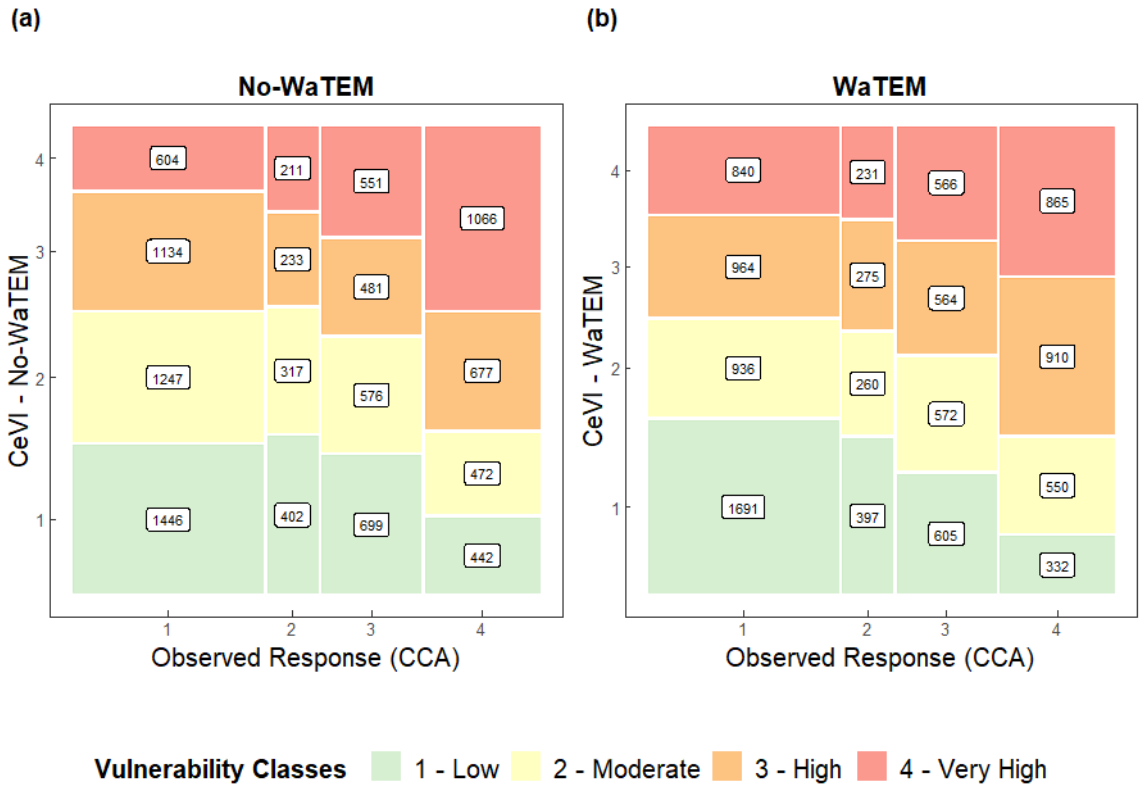

Figure 3.3.7 - Mosaic plot of the CeVI (No-WaTEM and WaTEM models) and CCA (calculated by polygonal approach) classes. The colors green, yellow, orange, and red correspond, respectively, to the classes CeVI low (1), moderate (2), high (3) and very high (4). The size of each box is relative to the number of cases of coupling (reported also as number).

Specific considerations for each LC can be done when looking at the maps of both approaches (Figure 3.3.8).

The erosion vulnerability map obtained by WaTEM model shows low-vulnerability coastal units in the central Tyrrhenian coastal sector (10.1 LC) and in the central (3.1 LC) and northern Ionian coastal sector (2.2 and 2.1 LCs). However, in the 2.1 and 3.0 LCs, there are coastal stretches with moderate vulnerability (class 2). High-vulnerability coastal areas are located on the eastern Tyrrhenian side, including littoral cells 10.2, 11.1 and 1.1.

Moreover, small coastal stretches are also found in 5.2 LC. The Sicilian coasts with very high vulnerability fall in the south-eastern side of the central Mediterranean sector (5.1 and 4.2 LCs) and on the opposite side in the western sector, including the 7.1, 7.2, 8.1, 8.2 and 8.3 LCs. Figure 3.3.8b shows the vulnerability erosion map obtained by the No-WaTEM model, with the difference compared to the map shown in Figure 8a. In the Tyrrhenian sector, the vulnerability class in LC 10.2 increases from class 3 for the WaTEM model to class 4. This is explained because the WaTEM model assesses high sediment supply (Ss = 1). In this way, the CeVI value decreased from 4 to 3. Another case in the Tyrrhenian sector is LC 1.1, where low sediment supply (Ss = 3) produces an increase in the CeVI value corresponding to high erosion vulnerability. In the Central Mediterranean sector, in LC 5.2, it is possible to observe an increasing (of one class, e.g., from 2 to 3) trend of the CeVI values. In this case, the WaTEM model suggests low vulnerability. On the southern Ionian coast (LC 3.1), the vulnerability

index increases from 2 to 3. In this case, using the WaTEM model, the CeVI vulnerability values are lower. The subplots from Fig 3.3.8c to Fig 3.3.8h show a magnification of some representative coastal stretches. Eraclea Minoa beach has a logarithmic spiral shape, and during recent years, it was struck by erosion phenomena.This dissipative beach is located far from defense structures and harbors, and for this reason the longitudinal sediment transport is not influenced. Nevertheless, the sediment supply load provided by the Platani river (at the northern part of the beach) is not sufficient to guarantee the sediment balance. This logarithmic spiral beach is characterized by intense wave diffraction causing high sediment transport effects. Considering the WaTEM model (Figure 3.3.8c), this beach has a high vulnerability (class 3), and this is due to the values of the indicators (e.g., S = 4; Ss = 1, St = 3; We = 2 and G = 4). With the No-WaTEM approach (Figure 3.3.8d), the class vulnerability increases. Casa Bianca beach (Messina) (Figure 3.3.8e) is a dissipative sandy beach between two headlands, and it is about 1.5 km long and about 22 m wide. The very high vulnerability values observed in this beach can be caused by a combination of two effects—the high mean values of longitudinal sediment transport and the low sediment load from the catchment areas. The WaTEM model (Figure 8e) shows very high vulnerability (class 4) obtained by indicators such as S = 4; Ss = 3, St = 2; We = 2 and G = 2. The No-WaTEM model decreases the vulnerability index from class 4 to class 3 (Figure 3.3.8f). Another case of very high coastal vulnerability is located on the rectilinear and dissipative sandy beach of Ispica (Ragusa) (Figure 8g). This beach is part of Pozzallo Gulf, where, on the north-western side, there is the Pozzallo harbor, which could trap longitudinal sediment transport. Additionally, in this case, the vulnerability values can be related to littoral currents and low sediment supply from rivers. The WaTEM model (Figure 3.3.8g) indicates very high vulnerability (class 4) obtained by indicators such as S = 4; Ss = 3, St = 2; We = 2 and G = 2. The No-WaTEM approach (Figure 3.3.8h) decreases the vulnerability index from class 4 to class 3. The results of the validation provide a qualitative and relative assessment of the CeVI procedure's effectiveness. The obtained validation results seem to confirm that the CeVI approach is suitable for estimating coastal erosion vulnerability on a regional scale. As expected, a loss in resolution power between the four vulnerability classes was observed for the intermediate classes (2 and 3), which that suggests better results could be achieved by using higher-resolution source layers or by exploiting a larger coastal change validation signal. However, the aim of this research was to test if by simply downloading and processing already available data (each one with its source resolution) a useful model could have been obtained. In this sense, the clear discrimination, down to a validation step, between the extreme classes (1 and 4) can be considered a point of strength for the method.

As regards the role of sedimental supply, a very puzzling scenario arose for the Sicilian coastline in the validation period. In fact, the WaTEM model highlighted some cases where the coast is retreating, but the sediment supply is significant. This can be explained in two ways: (a) the sediment supply is lost because the coastal dynamics transport it away beyond the closure depth; (b) the assessed sediment does not reach the river mouth because natural and/or anthropic features (dams, lakes, etc.) trap the sediment transport. This second hypothesis is linked to the WaTEM's characteristics, in that it computes the

sediment transport in hillslopes and rivers without considering erosion/deposition phenomena, which can trap the sediment eroded in the catchment in its routing to the river mouth, such as dams, lakes or transversal river structures. The comparison between No-WaTEM and WaTEM models poses limits in those areas characterized by natural and/or anthropogenic sediment interruptions to the hydrographic connectivity.

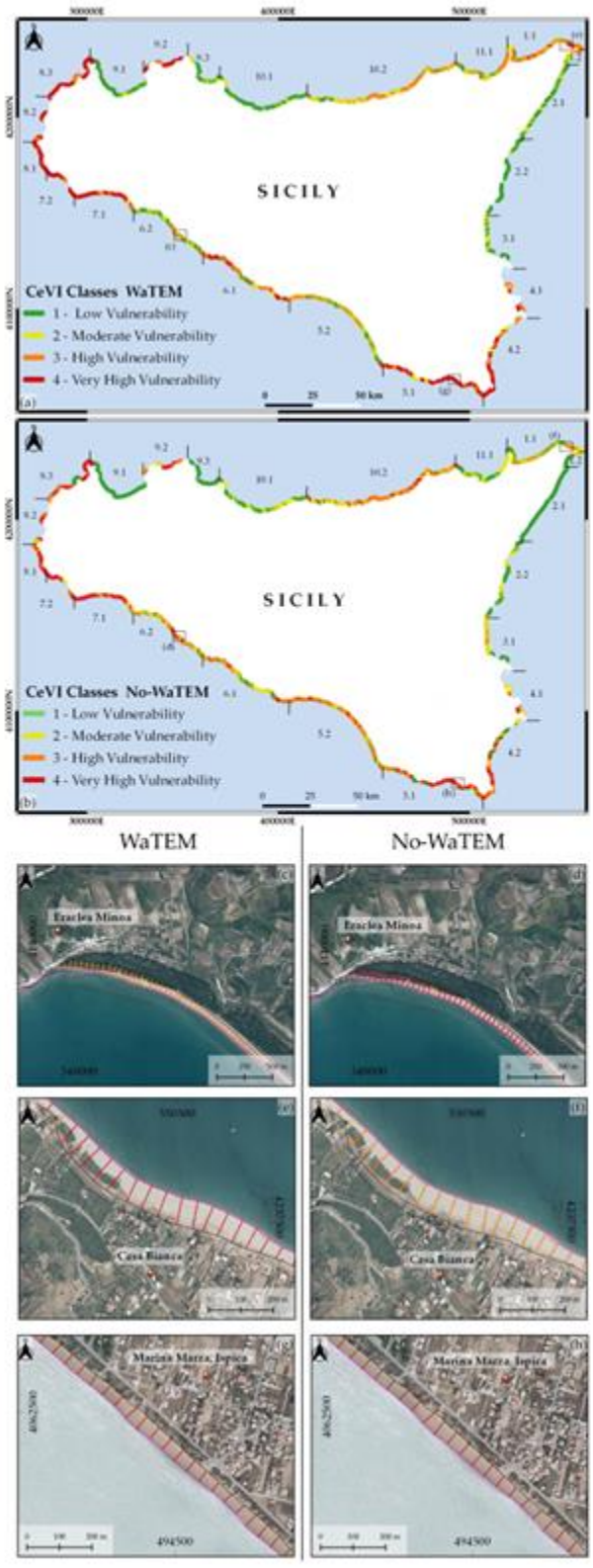

Figure 3.3.8 - The Sicilian coastal erosion vulnerability maps obtained by using, respectively, the WaTEM(subplot a) and the No-WaTEM (subplot b) models. (Subplots c,d) show the Eraclea Minoa beach(Trapani) vulnerability classes computed, respectively, with the WaTEM and No-WaTEM models.(Subplots e,f) show the Casa Bianca beach (Messina) vulnerability classes computed, respectively, with theWaTEM and No-WaTEM models. (Subplots g,h) show the Ispica beach (Ragusa) vulnerability classes computed, respectively, with the WaTEM and No-WaTEM models. The four vulnerability classes, from 1 (low vulnerability) to 4 (very high vulnerability), are depicted, respectively, in four colors: green, yellow, orange, and red.

3.3.5 CONCLUSIONS

In conclusion, this research shows a new approach to the regional assessment of coastal erosion vulnerability. In particular, a new approach named CeVI was used which considers different physical variables including morphological and hydraulic effects. The result of this approach is a new map of the coastal erosion vulnerability of Sicily. Differing from the approaches adopted in the literature which include coastal changes among the vulnerability factors, in the proposed method, coastal changes are conceptually moved to the validation of a vulnerability model which is totally dependent on factors related either to the forcing and the resilience of the coastal areas. According to the regional scale which was assumed in this research, the insights into the general picture of the coastal vulnerability conditions raise some basic research issues, including: the role of the morpho-dynamic connectivity both from the catchment to the river mouth (for sediment supply) and from adjacent littoral cells; the need for a higher-resolution database for characterizing the sea weather conditions; and the need for an accurate database of natural/anthropic sediment traps. To this end, the regional map which was obtained seems to be reliable and suitable for indicating those specific areas where more detailed modelling is required.

4.0 REFERENCES

Allan, J.D., Castillo, M.M., Capps, K.A., 2021. Stream Ecology: Structure and Function of Running Waters. Springer International Publishing, Cham. https://doi.org/10.1007/978-3-030-61286-3

Allen, R.G., Jensen, M.E., Wright, J.L., Burman, R.D., 1989. Operational Estimates of Reference Evapotranspiration. Agronomy Journal 81, 650–662. https://doi.org/10.2134/agronj1989.00021962008100040019x

Ampt, G.A., Heber Green, W., 1911. Studies on Soil Phyics. The Journal of Agricultural Science 4, 1–24. https://doi.org/10.1017/S0021859600001441

Armaroli, C., Duo, E., 2018. Validation of the coastal storm risk assessment framework along the Emilia-Romagna coast. Coastal Engineering 134, 159–167. https://doi.org/10.1016/j.coastaleng.2017.08.014

Arnold, J.G., Moriasi, D.N., Gassman, P.W., Abbaspour, K.C., White, M.J., Srinivasan, R., Santhi, C., Harmel, R.D., Van Griensven, A., Van Liew, M.W., 2012. SWAT: Model use, calibration, and validation. Transactions of the ASABE 55, 1491–1508.

Ballabio, C., Panagos, P., Monatanarella, L., 2016. Mapping topsoil physical properties at European scale using the LUCAS database. Geoderma 261, 110–123. https://doi.org/10.1016/j.geoderma.2015.07.006

Billi, P., Fazzini, M., 2017. Global change and river flow in Italy. Global and Planetary Change 155, 234–246. https://doi.org/10.1016/j.gloplacha.2017.07.008

Bird, E.C.F., 2008. Coastal geomorphology: an introduction, 2nd ed. ed. Wiley, Chichester, England ; Hoboken, NJ.

Boak, E.H., Turner, I.L., 2005. Shoreline Definition and Detection: A Review. Journal of Coastal Research 214, 688–703. https://doi.org/10.2112/03-0071.1

Boardman, J., Poesen, J. (Eds.), 2006. Soil erosion in Europe. Wiley, Chichester, England ; Hoboken, NJ.

Boccotti, P., 2000. Wave mechanics for ocean engineering, 1st ed. ed, Elsevier oceanography series. Elsevier, Amsterdam ; New York.

Borrelli, P., Van Oost, K., Meusburger, K., Alewell, C., Lugato, E., Panagos, P., 2018. A step towards a holistic assessment of soil degradation in Europe: Coupling on-site erosion with sediment transfer and carbon fluxes. Environmental Research 161, 291–298. https://doi.org/10.1016/j.envres.2017.11.009

Brown, L.C., Foster, G.R., 1987. STORM EROSIVITY USING IDEALIZED INTENSITY DISTRIBUTIONS. Transactions of the American Society of Agricultural Engineers.

Browning, G.M., Parish, C.L., Glass, J., 1947. Method for determining the use of limitations of rotation and conservation practices in the control of soil erosion in Iowa. Journal of the American Society of agronomy 39.

Bussettini, M., Braca, G., Lastoria, B., Mariani, S., 2013. Linee guida per l'analisi e l'elaborazione statistica di base delle serie storiche di dati idrologici.

Church, M., 2002. Geomorphic thresholds in riverine landscapes. Freshwater Biology 47, 541–557. https://doi.org/10.1046/j.1365-2427.2002.00919.x

Davie, T., 2010. Fundamentals of hydrology, 2. ed., repr. (twice). ed, Routledge fundamentals of physical geography series. Routledge, London.

De Vente, J., Poesen, J., Verstraeten, G., Van Rompaey, A., Govers, G., 2008. Spatially distributed modelling of soil erosion and sediment yield at regional scales in Spain. Global and Planetary Change 60, 393–415. https://doi.org/10.1016/j.gloplacha.2007.05.002

Dedkov, A.P., Moszherin, V.I., 1992. Erosion and sediment yield in mountain regions of the world. Erosion, debris flows and environment in mountain regions 209, 29–36.

Desmet, P.J.J., Govers, G., 1996. A GIS procedure for automatically calculating the USLE LS factor on topographically complex landscape units. Journal of Soil and Water Conservation 51, 427–433.

Foster, G.R., 1986. Understanding Ephemeral Gully Erosion. National Academy Press, Washington DC, 90-125 Committee on Conservation Needs and Opportunities, Ed., Assessing the Natural Resource Inventory, Soil Conservation Service, Board of Agriculture, National Research Council.

Furlan, E., Pozza, P.D., Michetti, M., Torresan, S., Critto, A., Marcomini, A., 2021. Development of a Multi-Dimensional Coastal Vulnerability Index: Assessing vulnerability to inundation scenarios in the Italian coast. Science of The Total Environment 772, 144650. https://doi.org/10.1016/j.scitotenv.2020.144650

G. Arnold, J., N. Moriasi, D., W. Gassman, P., C. Abbaspour, K., J. White, M., Srinivasan, R., Santhi, C., D. Harmel, R., van Griensven, A., W. Van Liew, M., Kannan, N., K. Jha, M., 2012. SWAT: Model Use, Calibration, and Validation. Transactions of the ASABE 55, 1491–1508. https://doi.org/10.13031/2013.42256

Gornitz, V., 1991. Global coastal hazards from future sea level rise. Palaeogeography, Palaeoclimatology, Palaeoecology 89, 379–398. https://doi.org/10.1016/0031-0182(91)90173-O

Gornitz, V.M., Kanciruk, P., 1989. Assessment of global coastal hazards from sea level rise.

Hargreaves, G.H., Samani, Z.A., 1985. Reference Crop Evapotranspiration from Temperature. Applied Engineering in Agriculture 1, 96–99. https://doi.org/10.13031/2013.26773

Intergovernmental Panel On Climate Change, 2023. Climate Change 2021 – The Physical Science Basis: Working Group I Contribution to the Sixth Assessment Report of the Intergovernmental Panel on Climate Change, 1st ed. Cambridge University Press. https://doi.org/10.1017/9781009157896

Julien, P.Y., 2010. Erosion and Sedimentation, 2nd ed. Cambridge University Press, Cambridge. https://doi.org/10.1017/CBO9780511806049

Koroglu, A., Ranasinghe, R., Jiménez, J.A., Dastgheib, A., 2019. Comparison of Coastal Vulnerability Index applications for Barcelona Province. Ocean & Coastal Management 178, 104799. https://doi.org/10.1016/j.ocecoaman.2019.05.001

Kron, W., 2005. Flood Risk = Hazard • Values • Vulnerability. Water International 30, 58–68. https://doi.org/10.1080/02508060508691837

Laws, J.O., Parsons, D.A., 1943. The relation of raindrop-size to intensity. Eos, Transactions American Geophysical Union 24, 452–460.

López Royo, M., Ranasinghe, R., Jiménez, J.A., 2016. A Rapid, Low-Cost Approach to Coastal Vulnerability Assessment at a National Level. Journal of Coastal Research 320, 932–945. https://doi.org/10.2112/JCOASTRES-D-14-00217.1

MCLAUGHLIN, S., COOPER, J.A.G., 2010. A multi-scale coastal vulnerability index: A tool for coastal managers? Environmental Hazards 9, 233–248. https://doi.org/10.3763/ehaz.2010.0052

Merritt, E., 1984. The identification of four stages during micro-rill development. Earth Surf Processes Landf 9, 493–496. https://doi.org/10.1002/esp.3290090510

Morgan, R.P.C., 2006. Soil erosion and conservation, 3. ed., [Nachdr.]. ed. Blackwell, Malden, Mass.

Moriasi, D.N., 2015. Hydrologic and Water Quality Models: Performance Measures and Evaluation Criteria. Trans. ASABE 58, 1763–1785. https://doi.org/10.13031/trans.58.10715

Moss, A.J., Green, P., Hutka, J., 1982. Small channels: Their experimental formation, nature, and significance. Earth Surf Processes Landf 7, 401–415. https://doi.org/10.1002/esp.3290070502

N. Moriasi, D., G. Arnold, J., W. Van Liew, M., L. Bingner, R., D. Harmel, R., L. Veith, T., 2007.

Model Evaluation Guidelines for Systematic Quantification of Accuracy in Watershed Simulations. Transactions of the ASABE 50, 885–900. https://doi.org/10.13031/2013.23153

Neithsch, S.L., Arnorld, J.G., Kiniry, J.R., Williams, J.R., 2009. Soil & Water Assessment Tool - Theoretical Documentation version 2009, Version 2009. ed. Texas A&M University System College Station, Texas 77843-2118, Texas Water Resources Institute Technical Report No. 406.

Orgiazzi, A., Ballabio, C., Panagos, P., Jones, A., Fernández-Ugalde, O., 2018. LUCAS Soil, the largest expandable soil dataset for Europe: a review. European J Soil Science 69, 140–153. https://doi.org/10.1111/ejss.12499

Panagos, P., Meusburger, K., Ballabio, C., Borrelli, P., Alewell, C., 2014. Soil erodibility in Europe: A high-resolution dataset based on LUCAS. Science of The Total Environment 479–480, 189–200. https://doi.org/10.1016/j.scitotenv.2014.02.010

Paola, G.D., Iglesias, J., Rodríguez, G., Benassai, G., Aucelli, P., Pappone, G., 2011. Estimating Coastal Vulnerability in a Meso-Tidal Beach by Means of Quantitative and Semi-Quantitative Methodologies. Journal of Coastal Research 61, 303–308. https://doi.org/10.2112/SI61-001.30

Poggio, L., de Sousa, L.M., Batjes, N.H., Heuvelink, G.B.M., Kempen, B., Ribeiro, E., Rossiter, D., 2021. SoilGrids 2.0: producing soil information for the globe with quantified spatial uncertainty. SOIL 7, 217–240. https://doi.org/10.5194/soil-7-217-2021

Priestley, C.H.B., Taylor, R.J., 1972. On the Assessment of Surface Heat Flux and Evaporation Using Large-Scale Parameters. Monthly Weather Review 100, 81–92. https://doi.org/10.1175/1520-0493(1972)100<0081:OTAOSH>2.3.CO;2

Renard, K.G., 1997. Predicting soil erosion by water: a guide to conservation planning with the Revised Universal Soil Loss Equation (RUSLE). US Department of Agriculture, Agricultural Research Service.

Ross, C.W., Prihodko, L., Anchang, J., Kumar, S., Ji, W., Hanan, N.P., 2018. HYSOGs250m, global gridded hydrologic soil groups for curve-number-based runoff modeling. Scientific Data 5, 180091. https://doi.org/10.1038/sdata.2018.91

Servizio Idrografico, 1916. Annali Idrologici, Parte II.

Shaw, J., Taylor, R.B., Forbes, D.L., Solomon, S. [Bedford Inst. of O., Dartmouth, NS (Canada)]", "Ruz, M.H. [Laval Univ., Quebec, PQ (Canada). Centre d`etudes nordiques]", 1999. Sensitivity of the coasts of Canada to sea-level rise, []. Geological Survey of Canada, Ottawa, ON (Canada), Canada.

Singh, A., Jha, S.K., 2021. Identification of sensitive parameters in daily and monthly hydrological simulations in small to large catchments in Central India. Journal of Hydrology 601, 126632. https://doi.org/10.1016/j.jhydrol.2021.126632

Slaymaker, O., Souch, C., Menounos, B., Filippelli, G., 2003. Advances in Holocene mountain geomorphology inspired by sediment budget methodology. Geomorphology 55, 305–316. https://doi.org/10.1016/S0169-555X(03)00146-6

Smith, D.D., 1941. Interpretation of soil conservation data for field use. Agric. Engg. 22, 173–175.

Smith, M.J., Cromley, R.G., 2012. Measuring Historical Coastal Change using GIS and the Change Polygon Approach: Measuring Historical Coastal Change. Transactions in GIS 16, 3–15. https://doi.org/10.1111/j.1467-9671.2011.01292.x

Soil Conservation Service, S., 1972. National engineering handbook, section 4, Hydrology. US Department of Agriculture Washington, DC.

Tapsell, S.M., Penning-Rowsell, E.C., Tunstall, S.M., Wilson, T.L., 2002. Vulnerability to flooding: health and social dimensions. Philosophical Transactions of the Royal Society of London. Series A: Mathematical, Physical and Engineering Sciences 360, 1511–1525. https://doi.org/10.1098/rsta.2002.1013

Thieler, R., 2000. Open-File Report (Open-File Report).

Tóth, B., Weynants, M., Pásztor, L., Hengl, T., 2017. 3D soil hydraulic database of Europe at 250 m resolution. Hydrological Processes 31, 2662–2666. https://doi.org/10.1002/hyp.11203

Van Oost, K., Govers, G., Desmet, P., 2000a. Evaluating the effects of changes in landscape structure on soil erosion by water and tillage. Landscape Ecology 15, 577–589. https://doi.org/10.1023/A:1008198215674

Van Oost, K., Govers, G., Desmet, P., 2000b. Evaluating the effects of changes in landscape structure on soil erosion by water and tillage. Landscape Ecology 15, 577–589. https://doi.org/10.1023/A:1008198215674

Van Rompaey, A.J.J., Verstraeten, G., Van Oost, K., Govers, G., Poesen, J., 2001. Modelling mean annual sediment yield using a distributed approach. Earth Surf Processes Landf 26, 1221–1236. https://doi.org/10.1002/esp.275

Vanoni, V.A., 1975. Sedimentation Engineering: Classic Edition. American Society of Civil Engineers.

Verstraeten, G., 2006. Regional scale modelling of hillslope sediment delivery with SRTM elevation data. Geomorphology 81, 128–140. https://doi.org/10.1016/j.geomorph.2006.04.005

Walling, D.E., 1983. The sediment delivery problem. Journal of Hydrology 65, 209–237. https://doi.org/10.1016/0022-1694(83)90217-2

Williams, A.T., Micallef, A., 2009. Beach management: principles and practice. Earthscan, London ; Sterling, VA.

Williams, J.R., 1975a. Sediment routing for agricultural watersheds. JAWRA Journal of the American Water Resources Association 11, 965–974.

Williams, J.R., 1975b. HYMO flood routing. Journal of Hydrology 26, 17–27. https://doi.org/10.1016/0022-1694(75)90122-5

Wischmeier, W.H., Johnson, C.B., Cross, B.V., 1971. Soil erodibility nomograph for farmland and construction sites.

Wischmeier, W.H., Smith, D.D., 1978a. Predicting rainfall erosion losses: a guide to conservation planning. Department of Agriculture, Science and Education Administration.

Wischmeier, W.H., Smith, D.D., 1978b. Predicting rainfall erosion losses: a guide to conservation planning. Department of Agriculture, Science and Education Administration.

Wischmeier, W.H., Smith, D.D., 1958. Rainfall energy and its relationship to soil loss. Eos, Transactions American Geophysical Union 39, 285–291.

Zingg, A.W., 1940. Degree and length of land slope as it affects soil loss in run-off.